

General Disclaimer

One or more of the Following Statements may affect this Document

- This document has been reproduced from the best copy furnished by the organizational source. It is being released in the interest of making available as much information as possible.
- This document may contain data, which exceeds the sheet parameters. It was furnished in this condition by the organizational source and is the best copy available.
- This document may contain tone-on-tone or color graphs, charts and/or pictures, which have been reproduced in black and white.
- This document is paginated as submitted by the original source.
- Portions of this document are not fully legible due to the historical nature of some of the material. However, it is the best reproduction available from the original submission.

JPL HIGHLIGHTS
1981

(NASA-CR-174535) JPL HIGHLIGHTS, 1981 (Jet
Propulsion Lab.) 131 P HC A07/MF A01
CSCL 05A

N84-11046

Unclass
G3/81 44292

JET PROPULSION LABORATORY
CALIFORNIA INSTITUTE OF TECHNOLOGY
PASADENA, CALIFORNIA

JPL HIGHLIGHTS

1981



JET PROPULSION LABORATORY
CALIFORNIA INSTITUTE OF TECHNOLOGY
PASADENA, CALIFORNIA

CONTENTS
ORIGINAL EDITIONS
COLOR

CONTENTS

INTRODUCTION	1
I. DEEP SPACE EXPLORATION	
A. Planets and Their Satellites	
Saturn	
Voyager Saturn Encounter and Uranus Mission	5
Saturn After Voyager 2	6
The Kings of Saturn	9
Titan	10
Other Saturnian Satellites	12
Magnetospheres of Jupiter and Saturn	15
Venus	
Temperature and Cloud Structure of Venus' North Pole	16
Jupiter	
Io Heat Flow	19
B. Astrophysics	
Studies in High-Energy Astrophysics via HEAO-3	20
Shuttle Infrared Telescope Facility Fine Guidance Sensor	22
Radio Interferometer Observations of Astronomical Object SS433	24
JPL Radar Astronomy: Asteroid Apollo and Saturn	26
C. Deep Space Navigation and Communication	
Voyager-Saturn Data Rate Enhancement	27
II. ENERGY AND ENERGY CONVERSION TECHNOLOGY	
Large Area Silicon Development	30

PRECEDING PAGE BLANK NOT FILMED

High-Performance Thermal Storage Materials Testing	32
Sunfuels: Integrated Fuels Production and Use	33
Acoustic Diagnostics of Turbulent Combustion	34
Quasi-Bipolar Lead-Acid Battery	36
Automotive Diesel Engine Particulates Destruction by Electrical Discharge	38

III. EARTH ORBITAL APPLICATIONS

Global Maps of Water Vapor, Wind Speed and Wave Height	42
Advances in Digital SAR Processing Techniques	45
Tectonic Studies in the Caribbean With Seasat Radar Imagery	46
Seasat Altimeter Studies in the Gulf of Mexico	48
Seasat Scatterometer Detection of a Tropical Depression in the Gulf of Mexico	50
Joint JPL/Caltech/People's Republic of China Earthquake Fault Study	52
Portable Radio Geodesy for Geodynamics Measurements	54
Balloon-Borne Microwave Limb Sounder	56
Maritime Remote Sensing (MARSEN) Experiment in the North Sea	58
Regular Solar Irradiance Variations Related to Solar Active Regions	60
Zero Gravity Fluid Dynamics	62

IV. INFORMATION SYSTEMS AND SPACE TECHNOLOGY DEVELOPMENT

Image Processing Using Very Large Scale Integrated Systems	64
Automated Spacecraft Power Systems Management	66
Remote Manipulator System	68
Target Body Tracker	70
Model Insensitive Control for Elastic Spacecraft Study and Experiment	72

Optical Fibers for Frequency Distribution	74
Radio Frequency Interference Surveillance	76
Delta Differenced One-Way Range for Navigation	78
An Efficient Atom Source for Hydrogen Maser Frequency Standard	80
Spacecraft Contamination Flight Data (NOAA-7)	82
Rocket Propellant High-Pressure Combustion Study	84
Heat Sterilizable Solid Rocket Motor	86
Electrostatic Levitator for Containerless Science in Space	87
Detector Arrays for Infrared Imaging	88
An Electron-Photon Coincidence Technique as a Radiometric Calibration Standard in the Vacuum Ultraviolet	90
Tunable Lasers for Remote Sensing Applications	91
Extraction of Oxygen From Carbon Dioxide	92
V. TECHNOLOGY APPLICATIONS	
Computer Animation of Space Mission Planetary Encounters	96
A Technology for the Production of Fusion Targets	98
Automated Cervical Cancer Screening	100
Clear-Air Turbulence Avoidance Using Microwave Radiometry	102
Population Exposure to Air Pollution Study	104
Computer Enhancement of Coronary Arteries From Intravenous Angiograms	107
Anticancer Drug Microspheres for Leukemia Treatment	108
Advanced Ocean Technology Development Platform System	110
VI. BASIC RESEARCH	
Closed Ecosystems Research	114
Deep Space Optical Communication	116

The Dynamics of Free Liquid Drops	318
Electron Spin Resonance	120
AUTHORS, ADDRESSES, PHONE NUMBERS	122

INTRODUCTION

The impressive discoveries about Saturn's atmosphere, rings and satellites by Voyager 2 head this report on significant accomplishments of the Jet Propulsion Laboratory in research and development for the fiscal year ending September 30, 1981.

The entries were selected as the most important work completed during the fiscal year. Many achievements are in continuing programs; some are advances in work included in "JPL Highlights 1980."

Representing a broad spectrum of activities, the selections emphasize the three major programmatic goals of JPL: (1) implementation of deep space missions for NASA; (2) a leadership role in the Department of Energy's solar-electric development program for the nation; and (3) participation in Earth-orbital flight projects and experiments.

JPL often collaborates with other research centers, universities and private industry. Where feasible, subcontracting is done. The Voyager mission, as an example, is a multi-year collaborative effort involving thousands of scientists, engineers and technicians from many institutions and agencies in this country and abroad.

The first of this report's six sections summarizes achievements in exploring the solar system and analyzing discoveries produced by planetary missions. They were highlighted by photography of Saturn and its rings and large satellites by Voyager 2 during its encounter in late summer. Now Voyager 2 is en route to a January 1986 encounter with Uranus, and Voyager 1 is en route out of the solar system toward interstellar space.

Voyager 2 passed closer to Saturn than Voyager 1 had passed nine months earlier. The Voyager 2 trajectory provided a unique opportunity to examine the rings in greater detail, and several satellites at much closer range than Voyager 1.

Wind-velocity profiles for Saturn's atmosphere have been worked up. Enceladus' surface appears to have a history that is both extremely old and extremely young. Explanations of the ringlets and spokelike features in the rings must be revised, based on data from Voyager 2.

Phoebe, Saturn's outermost satellite, was photographed by Voyager 2 on September 24, 1981. Phoebe is dark, round and has a radius of about 200 kilometers, almost twice the size computed from Earth-based observations.

Viking Lander 1, renamed the Thomas A. Mutch Memorial Station, continues to operate on the surface of Mars, with an automatic program to collect meteorological and imaging data through 1994.

The Pioneer Venus orbiter continues to return data. Venus' north polar region has been found to contain unusual cloud and temperature structures that suggest a clearing or depression in the polar cloud deck.

Analysis of heat-flow data from Jupiter's satellite Io shows that Io is more geophysically active than the Earth.

Studies of x-ray and gamma-ray emissions from data returned by HEAO-3 show a variety of new phenomena: For example, more than half the stars in the central region of the Hyades cluster are x-ray

emitters; an x-ray flare in one of the Hyades stars was 1000 times brighter than a solar flare.

JPL delivered a prototype version of the fine-guidance sensor for the space shuttle infrared telescope facility. The sensor exhibits a high degree of autonomy through use of a high-performance microcomputer.

In energy and energy-conversion research, reported in the second section of this document, the Large Area Silicon Sheet Task advanced the growth of single-crystal ingots of silicon by the Czochralski technology. The task group demonstrated growth of five monocrystalline ingots of 15-centimeter diameter, each weighing about 30 kilograms, from a single crucible.

JPL has demonstrated production of a valuable chemical and fuels from agricultural wastes using concentrated solar thermal radiation as the only energy source.

A new lead-acid battery structure under development at the Laboratory offers advantages in terms of energy density, power density, and energy efficiency.

An electrical discharge technique developed by JPL as an extension of NASA technology for measuring carbon-fiber particulates holds promise for reducing emissions from diesel-powered automobiles.

The Earth-orbital applications section reports on data returned by Seasat that has provided the first

global pictures of water vapor, wave height and wind speed over the oceans.

A high-speed digital synthetic aperture radar processor has been developed. It is capable of processing a 100- by 100-kilometer Seasat SAR image in 2.5 hours.

Data from the Seasat altimeter during the satellite's 1978 passages over the Gulf of Mexico confirmed sea-based models of a large anticyclonic eddy of the gulf's current loop. That variable current is the primary source of the Gulf Stream.

A group of geologists from Caltech and JPL joined counterparts from the People's Republic of China in a joint study of the San Andreas Fault in California and the Red River Fault in China's Yunnan Province. The Red River Fault is less active than the San Andreas.

The section on information systems and space technology development contains a report on a voice-control system developed and tested by JPL. The system controls the space shuttle's cameras and monitors. It is a 50-foot-long mechanical arm mounted in the cargo bay of the shuttle.

Technology applications research at JPL includes a description of a computer-animation system for demonstrating spacecraft planetary encounters. The system demonstrated the two Voyager encounters with Jupiter and the two encounters with Saturn.

I. Deep Space Exploration

VOYAGER SATURN ENCOUNTER AND URANUS MISSION

Both Voyagers 1 and 2 carried out extraordinary encounters with Saturn during the period of this report. After Voyager 1's encounter, in November 1980, the Voyager Project team focused on preparing for Voyager 2's August 1981 encounter. Voyager 2's planned observations were significantly changed, as a result of Voyager 1's findings at Saturn, to improve science returns from the second encounter. The Voyagers succeeded at Saturn far beyond expectations, including detailed atmospheric and magnetospheric studies; images of all 17 satellites, three of which were discovered by Voyager; and exciting definition of Saturn's complex ring system. The Voyager 2 Saturn encounter marks the end of the

Voyager Project's primary Jupiter-Saturn encounter mission that began with project approval in June 1972.

The Voyager Project now phases into the Uranus-Interstellar Mission that includes continued investigation of the interplanetary-interstellar media by both Voyager 1 and Voyager 2, and Voyager 2's Uranus encounter in January 1986, and a possible continuation to Neptune in August 1989. It is noteworthy that the primary mission was completed within the targeted total run-out cost covering FY 72 through FY 81. The following reports summarize highlights of the Saturn encounters.

PRECEDING PAGE BLANK NOT FILMED

SATURN AFTER VOYAGER 2

The rotation period of Saturn's magnetic field was determined from Voyager 1's planetary radio astronomy experiment to be 10 hours, 39 minutes, 24 ± 3 seconds. That is presumed to be the rate at which the bulk of Saturn's interior rotates. Cloud motions relative to the basic rate have been deduced on the basis of time-lapse imagery from Voyagers 1 and 2, and are summarized in the latitudinal wind profile on the opposite page. Winds are consistently eastward between $+35^\circ$ and -35° latitude, cloud vortices and eddies are apparent between opposing wind jets, and such features are observed to exist up to very high latitudes in Saturn's north polar region.

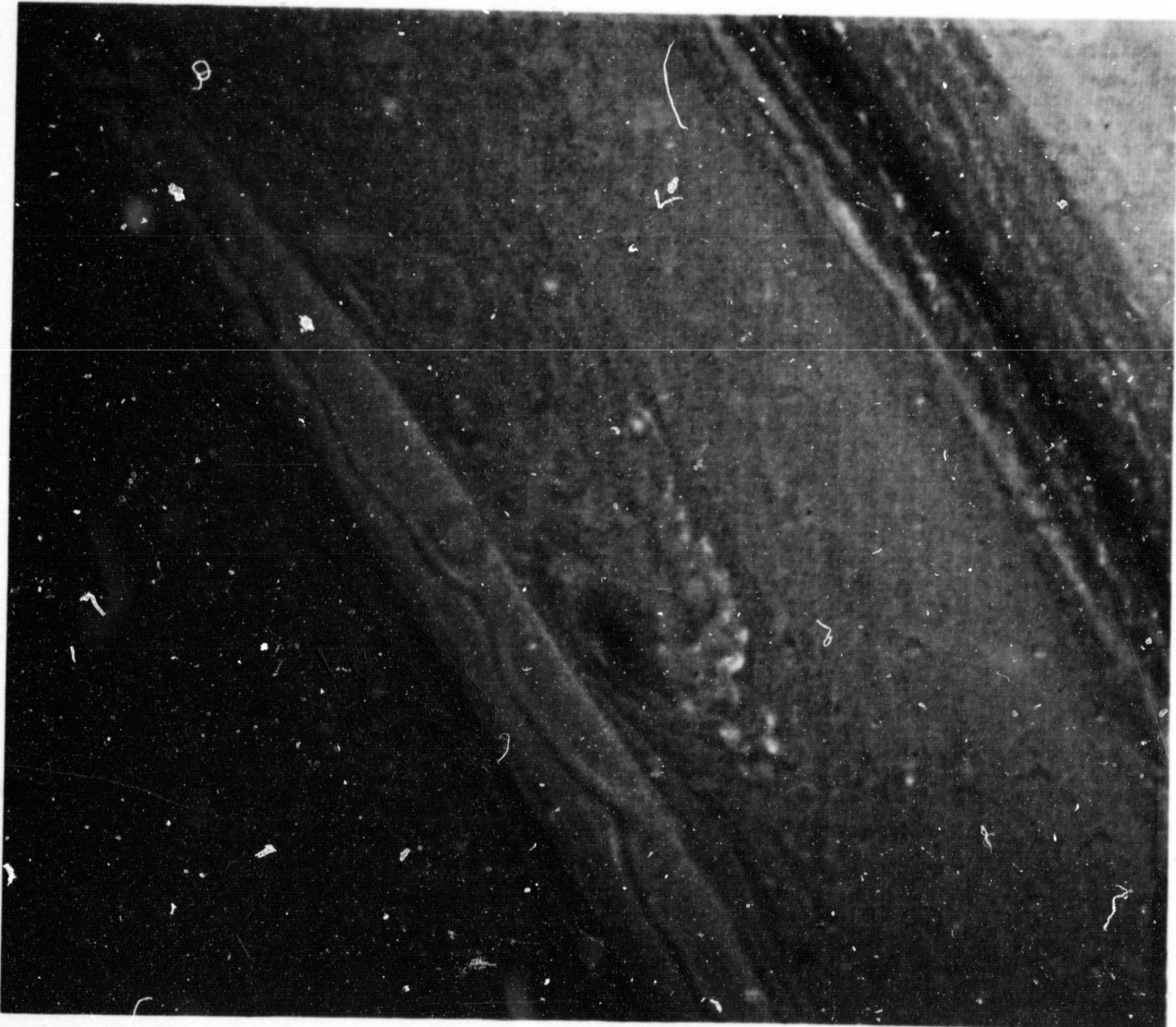
Voyagers 1 and 2 provided a total of four atmospheric radio occultation profiles: two near local sunset at latitudes of -73° and $+36^\circ$, and two near local sunrise at latitudes of 0° and -31° . All show minimum temperatures of about 80 kelvins near the 0.1-bar level and higher temperatures above and

below that level. The Voyager 2 profiles are shown on the opposite page. At the -73° latitude point, the radio science experiment determined a peak ionospheric electron density of 23,000 electrons per cubic centimeter at a height of about 2500 kilometers above the 1-bar pressure level.

The infrared experiment on Voyager 1 deduced that hydrogen (H_2) makes up 94 percent by number of the atmosphere of Saturn. Almost all the remaining 6 percent is helium (He), implying that helium is overabundant in Saturn's atmosphere. Gravitational sinking of helium, consistent with the observed overabundances, has been proposed as a source of thermal energy for Saturn, which radiates almost 2.5 times as much energy as it receives from the sun. Ammonia (NH_3), phosphine (PH_3), methane (CH_4), ethane (C_2H_6), acetylene (C_2H_2), methylacetylene (C_3H_4), and propane (C_3H_8) have all been identified as trace constituents of Saturn's atmosphere.

Figure (opposite page): False-color image of Saturn was made from two Voyager 2 frames — one violet and one green. Images were taken on August 19, 1981, from a distance of 7.1 million kilometers. Smallest observable features are 130 kilometers. Wavelike structures in ribbon are moving eastward (to right) at 150 meters per second.

ORIGINAL PAGE
COLOR PHOTOGRAPH



ORIGINAL PAGE IS
OF POOR QUALITY

PRECEDING PAGE BLANK NOT FILMED

Prior to the Voyager encounters, the rings of Saturn were seen as relatively uniform A-, B-, and C-rings, with occasional gaps at radial distances corresponding to orbital resonances with Saturn's inner satellites, notably Mimas. Additionally, two narrow rings, F and G, were imaged or proposed by Pioneer 11 investigators on the basis of depletions in the plasma environment. The broad but tenuous E-ring had been viewed only from Earth.

Voyagers 1 and 2 imaged the faint E-ring and verified the existence of the G- and D-rings, the latter an extremely faint inward extension of the C-ring. They furthermore revealed that the A-, B-, C-, D-, and F-rings appear to be composed of a startlingly complex system of ringlets of varying optical thickness. Radial structure is apparent down to the limit of resolution (100 meters for some of the photopolarimeter measurements) for nearly all ring observations. Many of the ringlets or ring boundaries are non-circular, implying that much of the observed structure may be rapidly changing under the influence of as-yet-unexplained dynamical forces. Two narrow ringlets appear at times to be composed of intertwined components.

Spoke-like aggregates of fine particles are seen against the B-ring, both on the illuminated and non-illuminated faces of the ring. These unexplained markings form over very short time periods (minutes), primarily near the point where the rings emerge from Saturn's shadow. Most dissipate before they complete a single orbit of Saturn.

Color differences are apparent between as well as within the major rings. Those color differences imply either composition or particle size distribution differences or a combination of the two. Analyses

of Voyager 1 radio signals transmitted through the rings lead to the conclusion that average particle diameters in the A-ring, outer Cassini Division, and C-ring are 10, 8, and 2 meters, respectively.

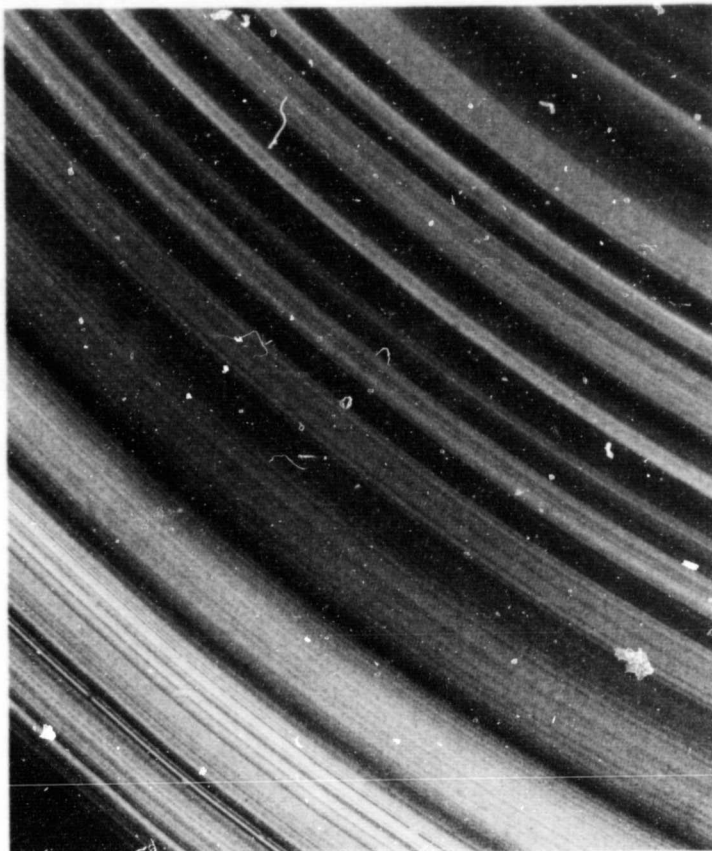


Photo of Saturn's B-ring taken by Voyager 2 on August 25, 1981, shows structure of the B-ring broken into about 10 times the number of ringlets previously known from Voyager 1 data. Narrowest features are about 15 kilometers wide. Variations in thickness are due to differences in particle density and light-scattering properties.

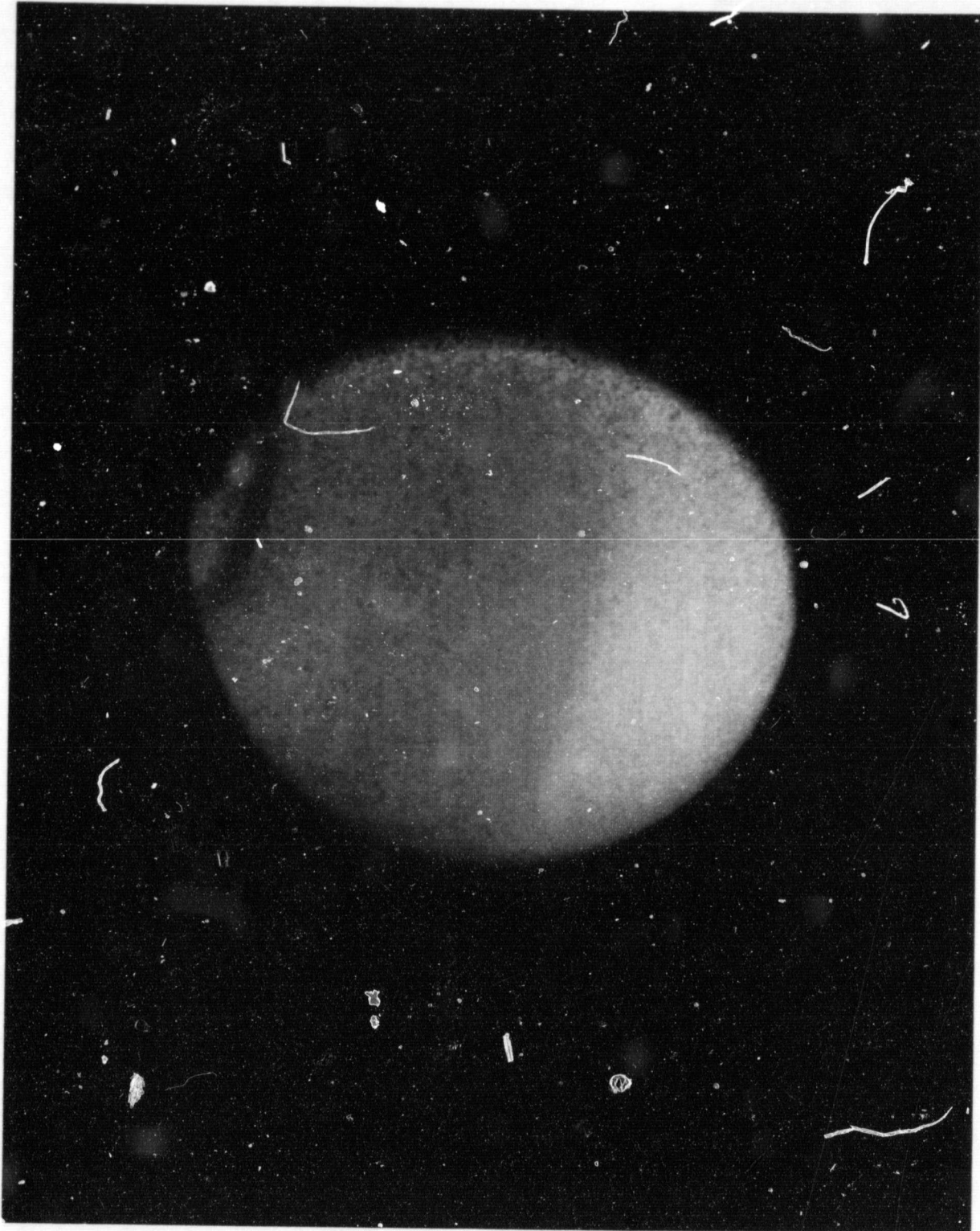
Long before Voyager 1 flew within 4000 kilometers of Titan's surface, this largest of Saturn's moons was known to possess a substantial atmosphere containing methane (CH_4), ethane (C_2H_6), ethylene (C_2H_4), and acetylene (C_2H_2). The thickness, composition, transparency, temperature, and pressure were largely unknown, and the diameter of Titan's solid body was uncertain by several hundred kilometers.

Voyager 1 radio-science measurements indicated the presence of a solid surface of radius 2570 km. Titan thus ranks second in size to Jupiter's Ganymede (radius = 2638 km) among solar system satellites. Both are larger than the planets Mercury and Pluto. Together with imaging results, the measurements of Titan's surface radius imply that surface-obscuring hazes extend to altitudes more than 200 km. Discrete haze layers detected by the imaging and ultraviolet experiments extend to still higher levels. Radio-science and infrared measurements are combined to pro-

vide an atmospheric temperature profile for Titan. At the bottom of the atmosphere, the temperature is 95 kelvins and the pressure is 1.6 bars. A minimum atmospheric temperature of about 70 K occurs at 0.1 bar, about 40 km above the surface. Ultraviolet, infrared and radio-science observations from Voyager all lead to the conclusion that, like the Earth, Titan's main atmospheric constituent is nitrogen (N_2), comprising about 82 percent of the total atmosphere. Spectroscopically undetectable argon is postulated to occupy most of the remaining 12 percent of the atmosphere. Trace amounts of a large number of other compounds of carbon, hydrogen and/or nitrogen have been detected in the Voyager spectra.

Analyses of photopolarimetric observations of Titan from Voyager 2 in late August 1981 are expected to yield information on the size and vertical distribution of the photochemical haze particles in the atmosphere.

ORIGINAL PAGE IS
OF POOR QUALITY



Voyager 2 image of Titan shows contrast differences and a well-defined equatorial boundary between the northern and southern hemispheres of Saturn's largest satellite. A dark polar collar also appears at about 60°N latitude. A distinct layer of submicron-size particles stands above the main cloud layer on the limb.

In addition to Titan, Saturn possesses 16 satellites, ranging in diameter from 30 to 1530 kilometers. Closest approach images of those satellites, all of which were imaged by Voyager, were taken at distances ranging from 74,000 km (1.4-km resolution) for Rhea to 2,080,000 km (36-km resolution) for Phoebe.

A composite photograph of the eight recently discovered and consequently unnamed satellites is shown below. All appear to have irregular shapes and to be in synchronous rotation, i.e., they keep the same face toward Saturn. Three of the "rocks" were discovered in Voyager 1 imagery, the remainder from telescopic observations here on Earth.

Phoebe, the outermost of the Saturn satellites, is probably a captured asteroid. Its orbit is retrograde and is near the ecliptic plane. All other satellites of Saturn have prograde orbits and are near Saturn's equatorial plane. Furthermore, Phoebe alone appears to be in non-synchronous rotation; it rotates once every 9 to 10 hours but

completes an orbit of Saturn only once every 550 days. Phoebe is also the least reflective of all the Saturnian satellites, reflecting only 5 percent of the sunlight striking its surface. Most of the others reflect from 40 to 90 percent of the light, consistent with their compositions, which are primarily water ice with differing percentages of rocky material.

Enceladus appears to be the most active satellite of Saturn, based on the variety of geologic forms on its surface. Mimas and Tethys each have impact crater scars that span one-third the diameter of the respective moons. Dione and Rhea have slightly darkened trailing faces that are crisscrossed with bright, wispy material. Hyperion has a highly irregular shape and orientation in space. Iapetus' surface is covered with materials that vary by a factor of 10 in reflectivity. One entire hemisphere reflects only 20 percent as much light as the other.

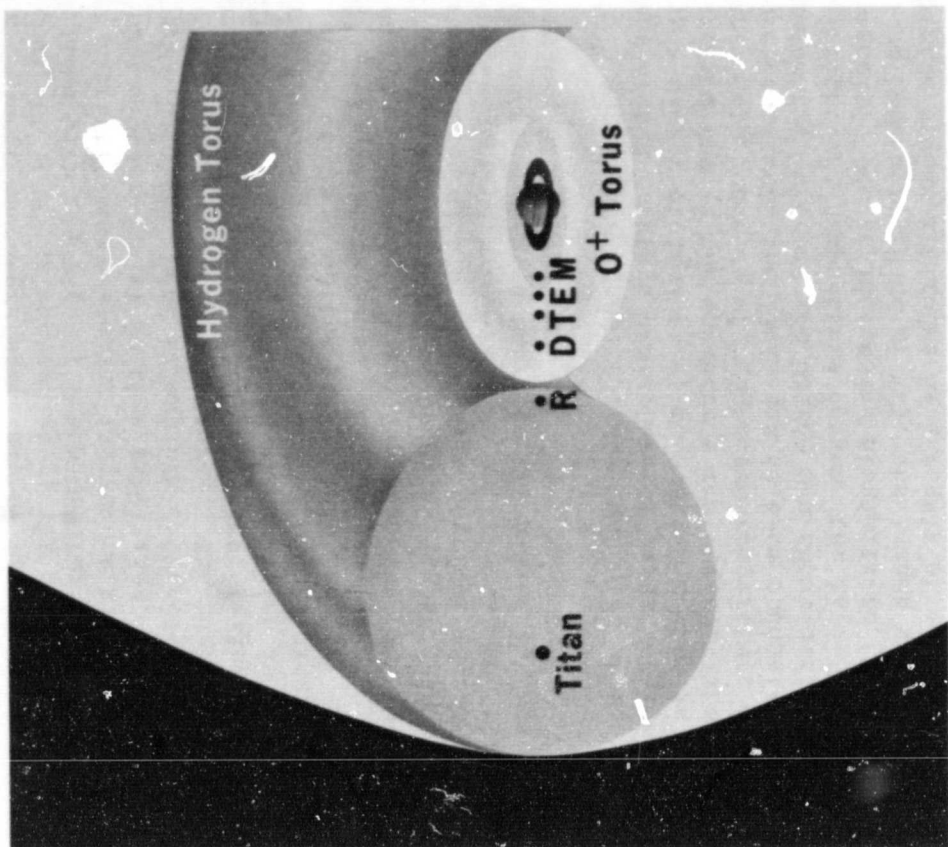
Accurate radio tracking of the Voyager spacecraft has provided accurate mass measurement; for Titan, Rhea, Iapetus, and Tethys.



Composite photo of newly discovered Saturnian satellites shows (clockwise from left) 1980S28, 1980S26, 1980S1, 1980S25, 1980S6, 1980S13, 1980S3, and 1980S27, all to the same relative scale. Enceladus (opposite page) has terrains of different ages - most recent appears less than 190 million years old.

ORIGINAL PAGE
COLOR PHOTOGRAPH





The approximately radial alignment of the sun, Jupiter, and Saturn early in 1981 provided Saturn-bound Voyager 2 a rare opportunity to observe the extended magnetic tail of Jupiter at a distance of almost half a billion kilometers behind Jupiter. At that distance, Jupiter's magnetotail may resemble a tattered wind sock waving in the solar wind that flows outward from the sun. It is likely that Saturn passed through that Jovian magnetotail several times in April 1981, but by Voyager 2's closest approach to Saturn in late August, no remnant effects of that passage were apparent.

Voyagers 1 and 2 extended the measurements of Pioneer 11 and gave a much better measure of the variability of the Saturnian fields, plasmas, and radio emissions. On the basis of bow shock and magnetopause crossing distances, Voyager data indicate that the average position of the bow shock is 31 Saturn radii (1 Saturn radius = 60,330 kilometers) in a sunward direction. The corresponding average position of the magnetopause is 22 Saturn radii in a sunward direction. It is further estimated that Titan's orbit (orbital radius = 20 Saturn radii) is entirely within the magnetosphere about 80 percent of the time.

Titan was discovered to have no intrinsic magnetic field and therefore does not have a liquid, electrically conducting core. Its atmosphere may be a source of neutral hydrogen atoms forming a torus of particles encompassing the orbits of Titan and Rhea.

Diagram shows relative sizes and positions of hydrogen and ionized-oxygen toruses discovered by Voyager 2. RDTEM are Saturn's satellites Rhea, Dione, Tethys, Enceladus, and Mimas. Hydrogen torus appears to extend from Saturn's magnetopause to inside orbit of Rhea.

The temperature structure of the stratosphere of Venus (65 to 95 kilometers above the surface) is being studied with the Pioneer Venus Orbiter using data from an infrared remote sensing instrument similar to those flown on terrestrial weather satellites. The polar region has been found to exhibit extremely interesting temperature and cloud structures. The highest temperatures at 11.5 micrometers, a carbon dioxide "microwave" window within which most of the emission is radiated from the cloud tops, are found within an elongated feature centered on the pole. This feature, seen only obliquely in Earth-based data, generally consists of two connected bright areas separated by 180° of longitude at latitudes of about 80°N. Brightness temperatures within the hottest portions of this polar "dipole" approach 260 kelvins at 11.5 μm , the highest temperatures seen anywhere on the planet at this wavelength.

The figure opposite shows two polar stereographic maps of the northern hemisphere of Venus obtained during a single orbital pass; the entire region is not observed due to the spacecraft trajectory. The top map represents contours of brightness temperature difference between the 13.1- and 13.8- μm channels of the radiometer, whereas the bottom map shows differences in brightness temperature between the 11.5- and 13.1- μm channels. Due to increasing proximity to the strong 15- μm absorption band of CO₂, the longer wavelengths observe higher altitudes as a result of enhanced gas opacity. The 11.5-, 13.1- and 13.8- μm channels are most sensitive to emission at altitudes of approximately 65, 70, and 80 km, respectively.

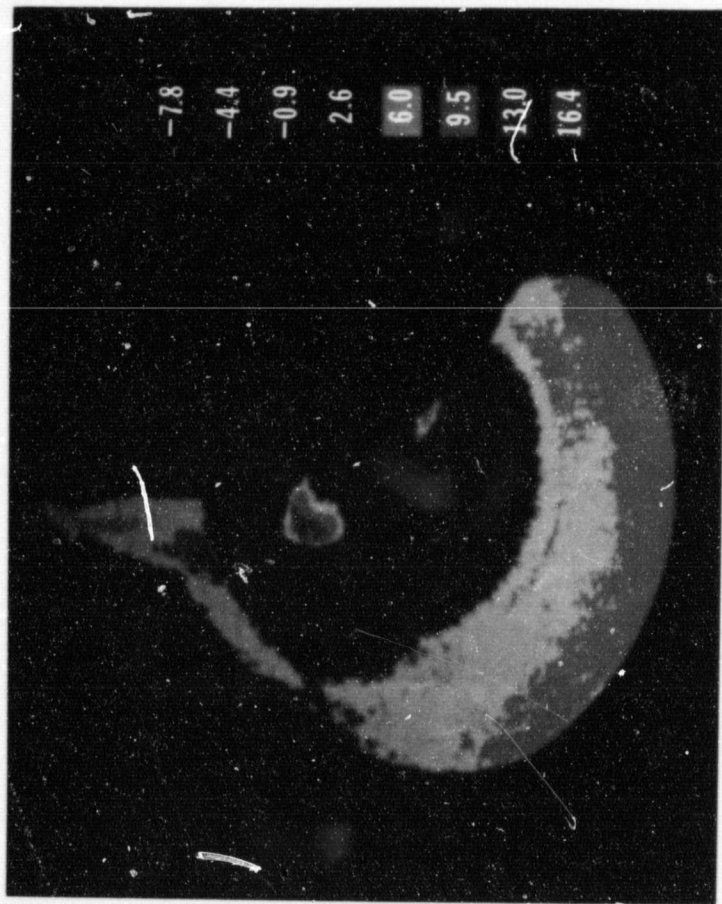
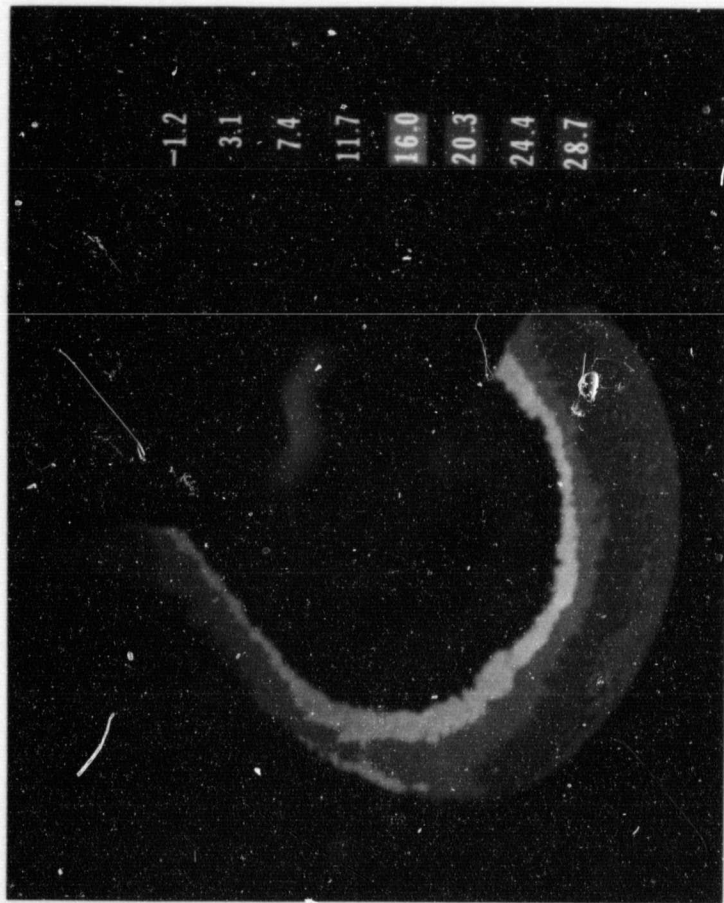
brightness temperatures at 11.5 μm compared to 13.1 μm , a trend which continues as wavelength increases (see top map). These results suggest that the dipole is a depression or clearing in the polar cloud deck. Data from other orbital passes show that the feature rotates about the pole with a period of roughly 3 Earth days.

The broad dark-blue region surrounding the pole at about 60-80°N is known as the polar collar, and is characterized by 11.5- μm brightness temperatures between 205 and 225 K. Such low temperatures were thought to be due to elevation in cloud height by about 15 km in the presence of a negative "vertical" temperature gradient. However, temperature retrievals using the radiometer data and comparisons with temperature profiles obtained from the Pioneer radio occultation experiment indicate that the clouds are not significantly elevated within the collar and appear colder due to a strong horizontal temperature gradient. In fact, the temperature profiles within the collar are inverted; that is, temperature is increasing with height. This result, which has led us to revise our picture of Venus' cloud structure, is demonstrated in the figure, which shows negative temperature differences within the collar between 11.5 and 13.1 μm , in contrast with the behavior shown elsewhere on the planet. Similar studies using data from other orbital passes are currently in progress and suggest that the strength of the collar temperature inversion is time-dependent.

Figure (opposite page): Contour map of the difference in brightness temperatures between the 13.1- and 13.8- μm channels (top) and the 11.5- and 13.1- μm channels (bottom). Numbers indicate the average value in kelvins for the corresponding contour level. Negative numbers indicate that the brightness temperature is higher at 13.8 μm than at 13.1 μm (top), suggesting an increase in temperature with height, and higher at 13.1 μm than at 11.5 μm (bottom). Note that the presence of strong temperature inversions at these altitudes (65-80 km) is confined to the collar region.

The dipole is seen in these maps as an elongated feature straddling the pole. Only one of the hot spots is completely visible and it appears in the lower map in orange-red, indicating significantly higher bright-

ORIGINAL PAGE
COLOR PHOTOGRAPH



10 HEAT FLOW

The JPL analysis of the thermal emission from Io yields 2 ± 1 watt per square meter as the heat flow from the interior. This is very large by any planetary criterion. Comparison with data for the Earth and the moon, in the table, shows that Io is the more geophysically active body. The heat flow is so large that it tells us that the interior of Io is partially molten on a global scale.

The heat flow determination for Io is possible because about one percent of Io's surface is covered by 'hot' spots, where heat leaves the interior and radiates into space. The hot spots have temperatures of 200-250 kelvins, occasionally hotter. By way of comparison, the surrounding country-side reaches a peak temperature of ~130 K at noon on the equator. At higher latitudes the peak temperatures are lower since the insulation of the surface there is less.

Because of this large temperature difference, between the hot spots and the remaining 99 percent of Io's surface, it is possible at infrared wavelengths to recognize two distinct temperature components in Io's thermal emission spectrum. The hot spots radiate most of their power at wavelengths

shorter than 15 micrometers; the remainder of the surface radiates power at wavelengths longer than 20 μm . The JPL team found that this spectral separation is clearly evident in the published observations of Io made 10 years ago by astronomers using telescopes on the Earth. However, the significance was not realized then because prior to Voyager Io was regarded as a quiescent satellite, known to have peculiar spectral reflectance, with sporadic outbursts of dekametric radio waves. The satellite also is situated within a large, diffuse cloud of neutral sodium atoms which accompanies it in its orbital trip about Jupiter. Therefore, Io's true thermal state was not fully appreciated until the eruptive plumes and surface hot spots were observed by Voyager 1.

Io probably has many other forms of intense geological activity in addition to the observed plumes, calderas, and lava flows. By analogy with the Earth, we would expect Io to also have large-scale convection and silicate volcanism. When the mid-1980s Galileo spacecraft goes into orbit about Jupiter, it will be possible to look for evidence of these other Ionic processes.

Heat Flow Data

Planet	Heat Flow	Comments
Earth		
Average	0.06	1.5
Geothermal area	1.7	40
Moon	0.02	0.5
Io	2 ± 1	48 ± 24
		Global heat flow through crust
		Wairakei, New Zealand
		Average of Apollo 15 and 17
		1 landing sites
		Global average

The x-ray and gamma-ray emission from cosmic sources is the subject of a continuing JPL research effort. These types of radiation give unique information on atomic and nuclear reactions. These reactions occur in the sun, stars, and the interstellar medium when energetic particles and photons undergo a large variety of physical processes.

The studies in x-ray and gamma-ray astronomy are primarily based on measurements obtained with the series of three High-Energy Astronomy Observatories (HEAO-1, -2, and -3) which operated between 1977 and 1981. The x-ray observations were obtained on HEAO-1 and HEAO-2 as collaborative investigations, while the gamma-ray observations were made with the JPL-built High-Resolution Gamma-Ray Spectrometer on HEAO-3.

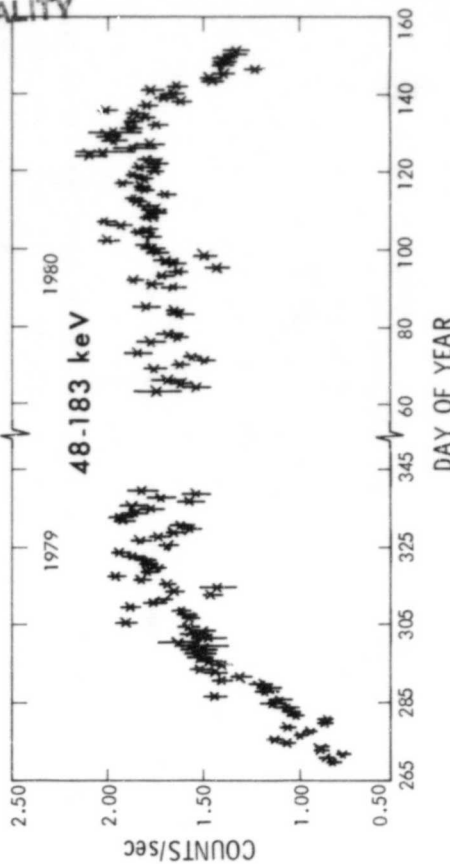
A survey of stars in the Hyades cluster showed that more than half of the stars in the central region are x-ray emitters. More than 80 percent of the stars which are similar to the sun (spectral types F V and G V) were observed to emit x-rays, 30 to 300 times as intense as those at the sun. An x-ray flare in one of the Hyades stars, 1000 times brighter than a solar flare, was detected. The interpretation of these measurements in terms of stellar-corona models adds to our understanding of the properties and evolution of stars.

The HEAO-3 Gamma-Ray Spectrometer performed the first survey of the full sky with high spectral resolution. Among the phenomena observed were: continuum and gamma-ray line emission from the sun; gamma-ray bursts; variations in the intensity of the black-hole candidate Cygnus X-1; and variations in the intensity of the positron-electron annihilation radiation from the vicinity of our galactic center.

Eight-month observations of Cygnus X-1, one of the brightest known x-ray emitters in the galaxy, disclosed an upward and a downward transition of the low-energy gamma-ray flux. Comparison of these gamma-ray observations with low-energy x-ray data from other experiments showed that Cygnus X-1 was in a hitherto-unknown type of low-emission state.

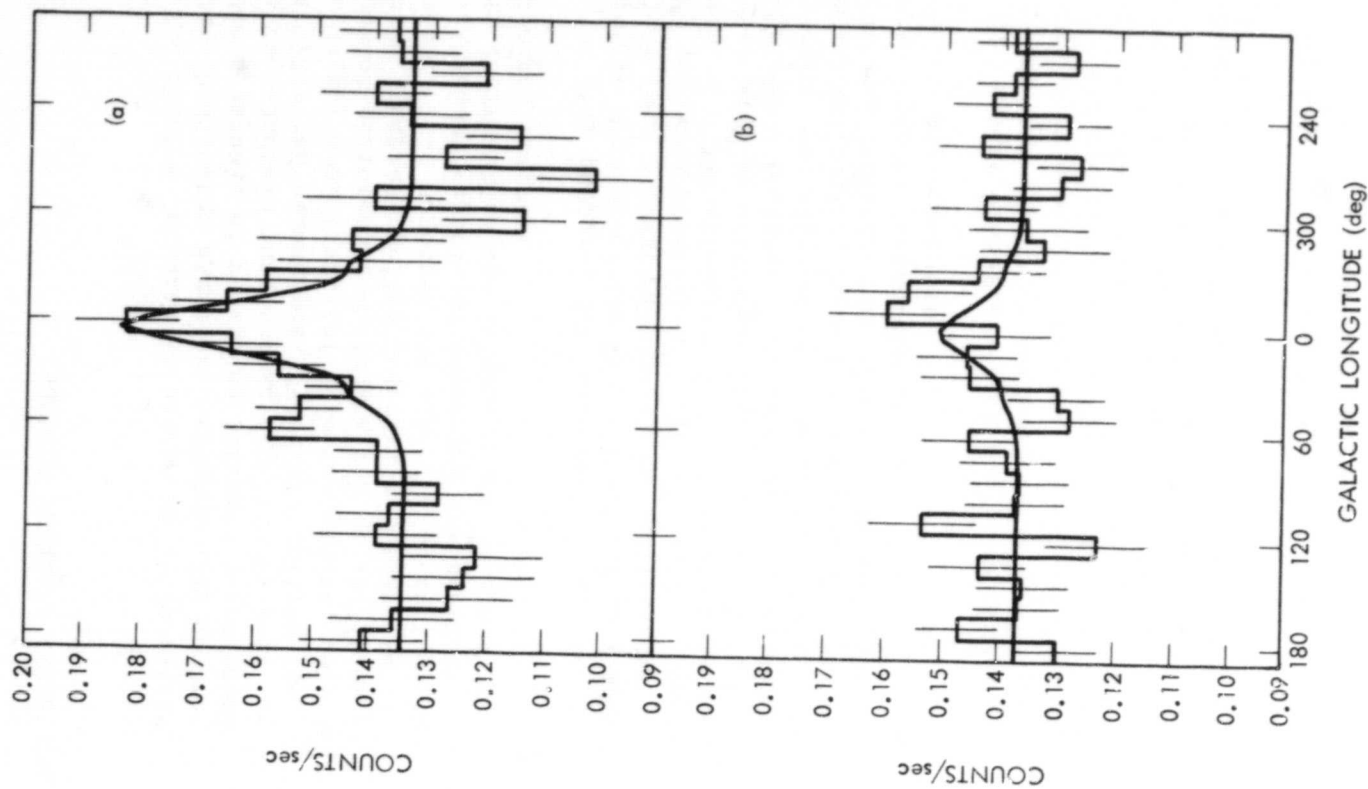
Positron-annihilation radiation at 511 kiloelectronvolts from the galactic center region had been detected previously, but the HEAO-3 spectrometer data produced statistical evidence of temporal variation of this radiation. The existence of a massive black hole at the galactic center, which had been suggested from infrared observations, provides a plausible explanation for the gamma-ray observation, although it cannot yet be proven with the available data.

ORIGINAL PAGE IS
OF POOR QUALITY



1979-1980 hard x-ray light curve of Cygnus X-1, a black hole candidate.

ORIGINAL PAGE IS
OF POOR QUALITY



Plot of the 511-keV positron annihilation line intensity as a function of galactic longitude (the galactic center is at longitude = 0). In (a), the smooth curve shows the best fit to a constant background level plus the response to a single source near the direction to the galactic center. The data shown in (b) were recorded approximately 6 months after the data shown in (a). Between the two observations, the signal from the galactic center region had decreased by a factor of approximately 3".

The Shuttle Infrared Telescope Facility (SIRTF) will be a 0.85-meter diameter, cryogenically cooled instrument capable of providing infrared astronomers with a thousandfold increase in sensitivity over present infrared telescopes. To fully utilize the extraordinary sensitivity of this instrument, pointing and control performance exceeding the capabilities of the basic Shuttle-supplied pointing mount system will be needed. This required the use of a precision star-tracking sensor capable of enhancing the accuracy and stability with which the telescope can be aimed at astronomical targets.

For this purpose, JPL developed and delivered a prototype version of the Fine Guidance Sensor (FGS) to NASA's Ames Research Center to be incorporated in a newly designed pointing and control system. The FGS consists of a 348-millimeter F/1.8 Schmidt-Cassegrain telescope with an active secondary mirror, Charge-Coupled Device (CCD) detector housing, CCD support electronics, and environmental control hardware. The FGS main electronics, housed in a separate chassis, employ a bus structured architecture in which the principal control element is an ATAC 16M high-performance microcomputer.

The sensor exhibits a high degree of autonomy through the use of a high-performance microcomputer operating from a stored program. The microcomputer controls the operation of the FGS and performs complex payload attitude determination computations based upon the multi-star position inputs. It also provides real-time corrections to CCD image response based upon known off-axis optical aberrations existing within the system.

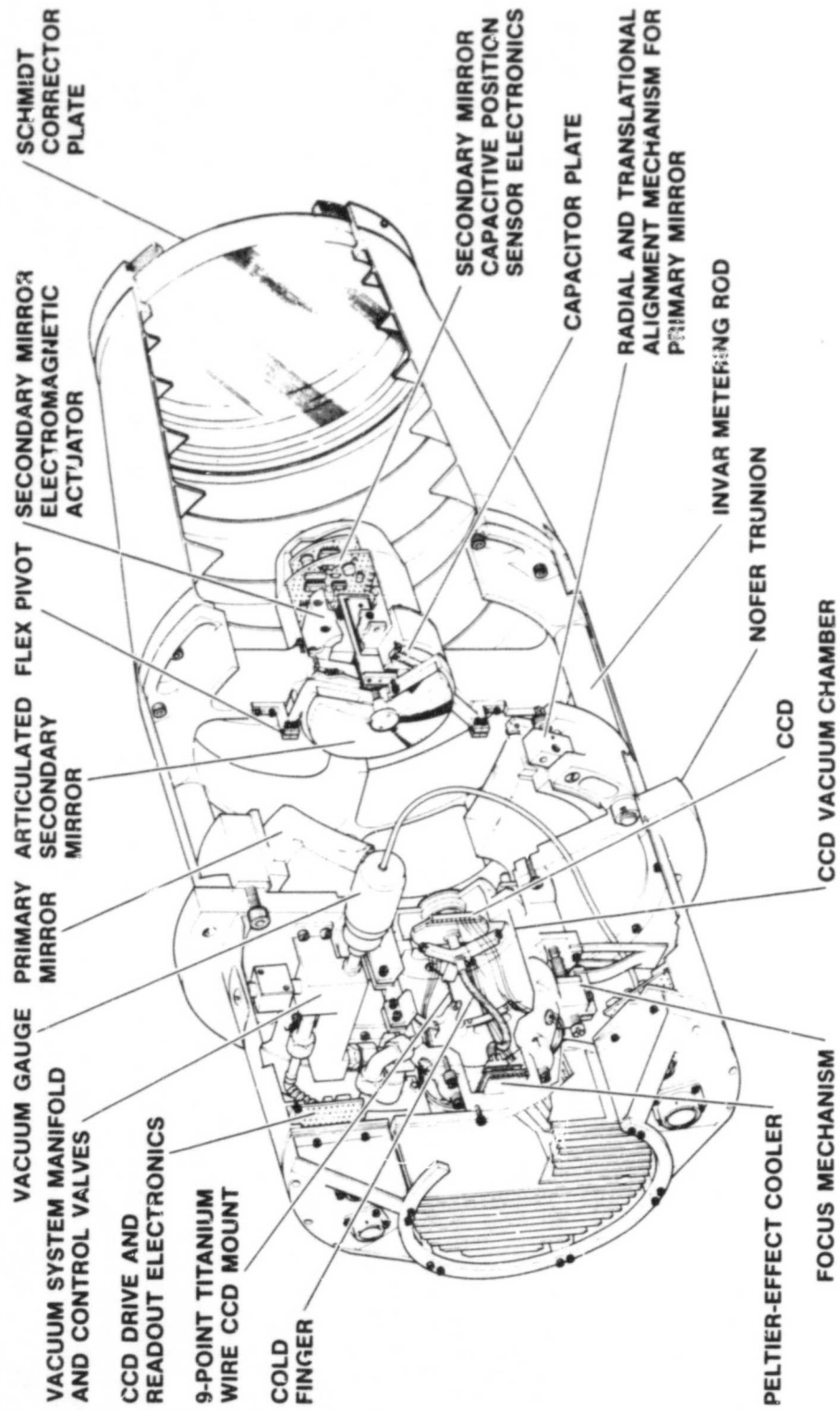
The FGS can acquire and track up to 20 stars within its field of view and supply coordinate and

intensity information on all tracked stars once during each scan frame. The measured position of each tracked star is refined through the use of digital centroid interpolation techniques to a precision which exceeds the CCD detector element resolution by more than 50 times. Within the four square degree field of view, the 320 x 512 element CCD provides star position resolution better than 0.5 arc second for stars as dim as ninth magnitude. Pointing and control dynamics are further improved by utilizing the movable secondary mirror within the FGS to achieve fine motion correction, rather than moving the entire telescope assembly.



SIRTF Fine Guidance Sensor prototype.

ORIGINAL PAGE IS
OF POOR QUALITY



Cutaway of SIRTF Fine Guidance Sensor.

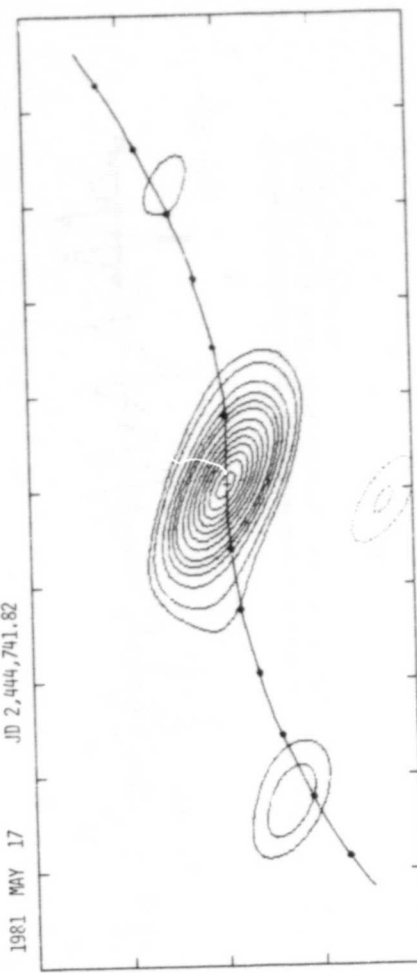
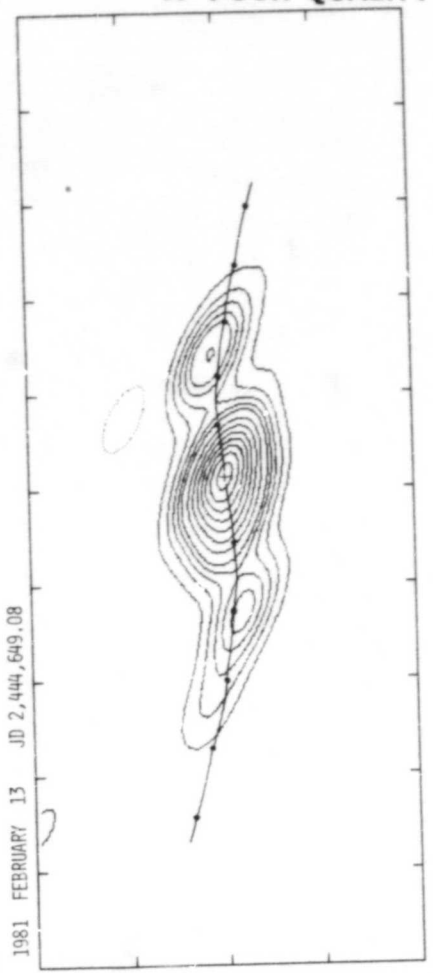
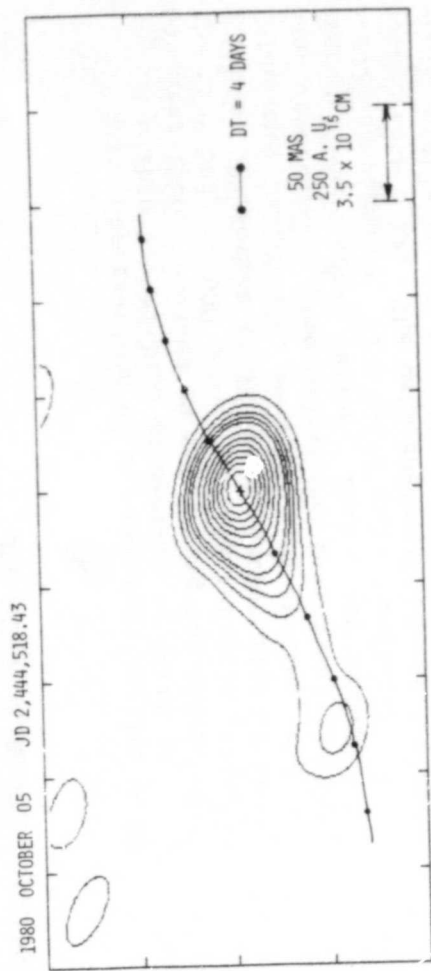
One of the most bizarre phenomena discovered in our universe is astronomical object SS433, an unusual star system which may be the remnant of a supernova explosion. Although located only about 15,000 light years from us within our own galaxy, it possesses several characteristics of very distant quasars and radio galaxies billions of times more massive and powerful. One characteristic is the very strong radio emission, which permits us to study their structure in much greater detail than is possible at optical wavelengths.

Our knowledge of the compact structure (the core and close-in jets) of these objects is obtained from simultaneous observations of their radio emissions by widely separated large antennas. This technique is called Very Long Baseline Interferometry (VLBI), and JPL and the stations of the Deep Space Network have had a significant role in its application to extragalactic and galactic astronomy. In the case of SS433 the sensitivity of the DSN stations has been of prime importance because of the weakness of its radio signal.

The unique features of SS433 are the extremely large velocity of the relatively cool ionized gas in the system, over one-quarter the speed of light, and the changes in these velocities that occur within a period of 164 days. Although it was proposed on the basis of the optical data that these were oppositely directed jets, only observations of the radio emission demonstrated that the model was correct and resolved ambiguities in the parameters of the model. In addition the distance of SS433 was determined by the radio observations.

Results of VLBI observations using a DSN antenna at Goldstone along with two other radio telescopes in California are shown in the accompanying figure. The radio contour maps, made at three different times, illustrate the changing jets by comparing the actual radio emission with the path expected from the model. They indicate that the radio emission is ejected in blobs rather than as smooth jets, suggesting that SS433 acts more like a machine gun firing discrete bullets than like a garden hose.

ORIGINAL PAGE IS
OF POOR QUALITY

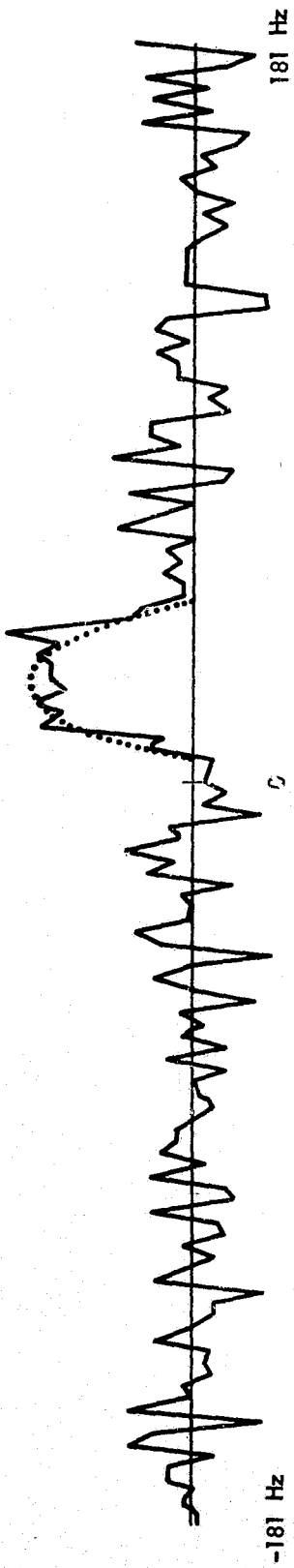


Contour maps of the radio brightness of SS433 at a wavelength of 13 centimeters are shown at three different times. The cross at the point of brightest emission is probably the place of origin of the blobs being shot out. The dots represent the location expected for previous ejections, even four days older. The curvature of the path traced by the dots is due to the changing direction along which the jets are emanating. The elliptical shapes of the contours represent the instrumental response of the interferometer.

Radar observations of the asteroid Apollo, which passed within 8.4 million kilometers of Earth in November 1980, resulted in estimating the radius of the tiny body at 600 meters and its rotation period at 3 hours. Performed by JPL radar astronomers at the Goldstone, California, 64-m tracking station, the X-band observations produced 48,000 individual spectra over a 14-hour total period. Each spectrum had a bandwidth of almost 1500 hertz and a resolution of better than 3 Hz. The data analyzed this year added significantly to our knowledge of the size of asteroids.

Radar observations of Saturn's rings were made during the past year with the ring plane only 6 degrees from being edge-on. The normalized radar cross section did not drop appreciably with angle. This result, coupled with earlier data and computer scattering simulations, shows that the ring particles must be much larger than the wavelength -- on the order of a meter or larger. Either ice or metal fits the data, but, in any case, the particles must be of irregular, jagged shape. This was a major supplement to the Voyager 1 imaging and radio science data.

ORIGINAL PAGE IS
OF POOR QUALITY



Average spectrogram of all of the November 1980 asteroid Apollo observations. Power density is plotted against frequency. The dotted curve is the theoretical response from an ideal rotating diffusing sphere having a radius of 600 m. The rotation rate was determined from the radar albedo variation with time, and a value of 3.06 h was observed.

After Voyagers 1 and 2 were launched, the detailed mission planning for Saturn encounter indicated that the video science value would be greatly enhanced if the planned X-band data rate of 27 kilobits per second (kbps) could be increased significantly. Several possibilities for increasing the Earth-station-gain over system-temperature ratio were investigated in an attempt to increase the data rate to 44 kbps at 30-degree elevation. This required about 2-decibel (58 percent) increased performance.

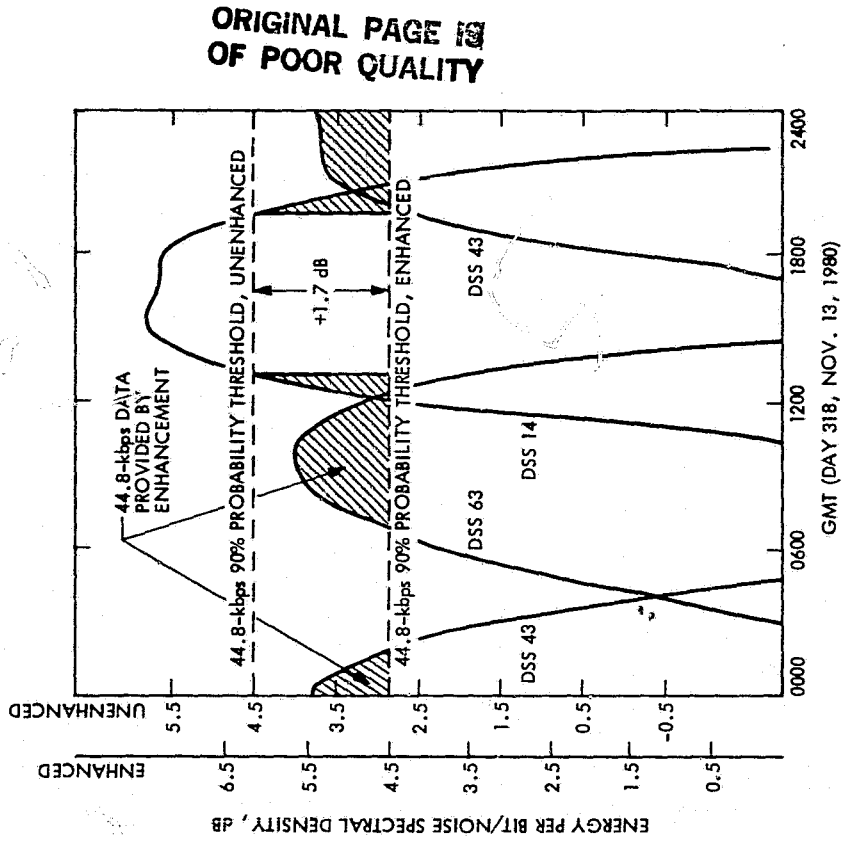
The options considered for these improvements included: array baseband telemetry signals from both 34- and 64-meter apertures (0.8 dB); increase 64-m gain by increasing feed illumination efficiency (0.3 dB); decrease system temperature from 27 to 22 kelvins by reducing maser contribution (0.6 dB); or decrease system temperature by removing the dichroic plate from the X-band horn (0.3 dB).

All four improvements were considered initially, but it was decided that an S-band uplink and downlink were a high priority requirement. Therefore, the dichroic plate had to remain, and 1.7 dB was the expected potential improvement.

The technology was fairly well in hand for these improvements. An array configuration had been demonstrated by the DSN Advanced Systems Program on Mariner Venus Mercury (MVM73). Hybrid mode feed beam-shaping, while not specifically demonstrated in the DSN, was fairly low risk. A low noise wideband X-band maser also was under development, and an S-band maser, incorporating low-noise transmission line principles, had been demonstrated.

These capabilities were developed and installed at each DSN complex (Goldstone, Australia, and Spain)

by mid-summer 1980. The desired performance improvements were achieved, or bettered, so that during much of the Voyager 1 Saturn flyby, a 44-kbps link was in operation.



44.8-kbps telemetry performance. Depicted are the link design margins actually obtained for the three DSN complexes as a function of time during the Saturn flyby sequence. The hatched areas are the times when the data rate threshold was raised by the 1.7-dB enhancement.

III. Energy and Energy Conversion Technology

PRECEDING PAGE BLANK NOT FILMED

LARGE AREA SILICON DEVELOPMENT

The Large Area Silicon Sheet Task of the Low-Cost Solar Array Project made notable progress in advancing the growth of single crystal ingots of silicon by the Czochralski (high-temperature melt) technology. The task force demonstrated the growth of 5 monocrystalline ingots of 15-centimeter diameter, each weighing about 30 kilograms, from a single crucible. (The current manufacturing technology is limited to the growth of a single 20-kg ingot of 10-cm diameter per crucible.)

The fact that the growth of 150-kg monocrystalline ingots of large diameter from a crucible of 20-kg capacity has been accomplished is noteworthy. This advancement, while achieving very high throughput,

also results in substantial reduction of costly consumables such as the crucibles and cycle time. This process was achieved through the development of the continuous melt replenishment technology.

The task force is currently focusing its effort on the development of automation needed for consistent control of ingot size and quality. With that feature demonstrated, the advanced Czochralski process will be a viable technology to meet the project cost objective of 70 cents per peak watt of photovoltaic module.

The Low-Cost Solar Array Project is managed by JPL for the Department of Energy.

ORIGINAL PAGE IS
OF POOR QUALITY



Five monocrystalline ingots of silicon, each 1.5 centimeters in diameter and weighing about 30 kilograms, were grown in an advanced Czochralski process to achieve low-cost solar arrays for U. S. energy needs.

HIGH-PERFORMANCE THERMAL STORAGE MATERIALS TESTING

The thermal power systems (TPS) utilizing solar energy require a method of thermal energy storage to compensate for cloud cover and afternoon load peaking. This energy can be stored as heat of fusion of salts which have melting points near the energy conversion system operating temperature (about 1500°F).

Several problems inherent in such a system are the high cost and corrosive nature of some salts, and the transfer of heat through the solidified layer of salt that forms. Corrosion testing of the sodium/sodium chloride (Na/NaCl) system at JPL indicates that all of the above problem areas can be avoided. Cost is not a problem with NaCl.

Corrosion is a problem with pure NaCl but the addition of sodium (Na) reduces the activity of the chlorine (Cl), producing a system similar to pure sodium in corrosion characteristics. This behavior has been confirmed by the JPL testing program in containment vessels of type 321 stainless steel and 9Cr-1 molybdenum alloy steel.

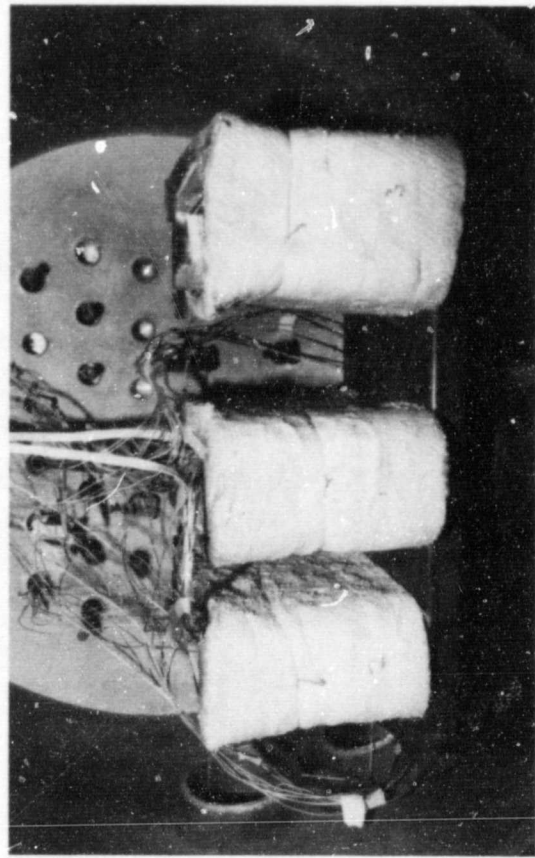
The vessels containing the thermal storage salt with sodium were cycled across the salt melting point once per hour for 4000 hours. Post-test analyses indicated moderate corrosion of the 9Cr-1 Mo alloy container with negligible corrosion effects of the 321 stainless steel.

The concept appears applicable to other salt systems of the alkali metal/alkali salt type. Improvements in heat transfer are under evaluation. When fully molten, the system produces two liquids, one salt rich and one alkali metal rich. The alkali metal liquid is lower in density and higher in thermal conductivity. It is available to transfer heat from the solidifying salt to a heat exchange system to

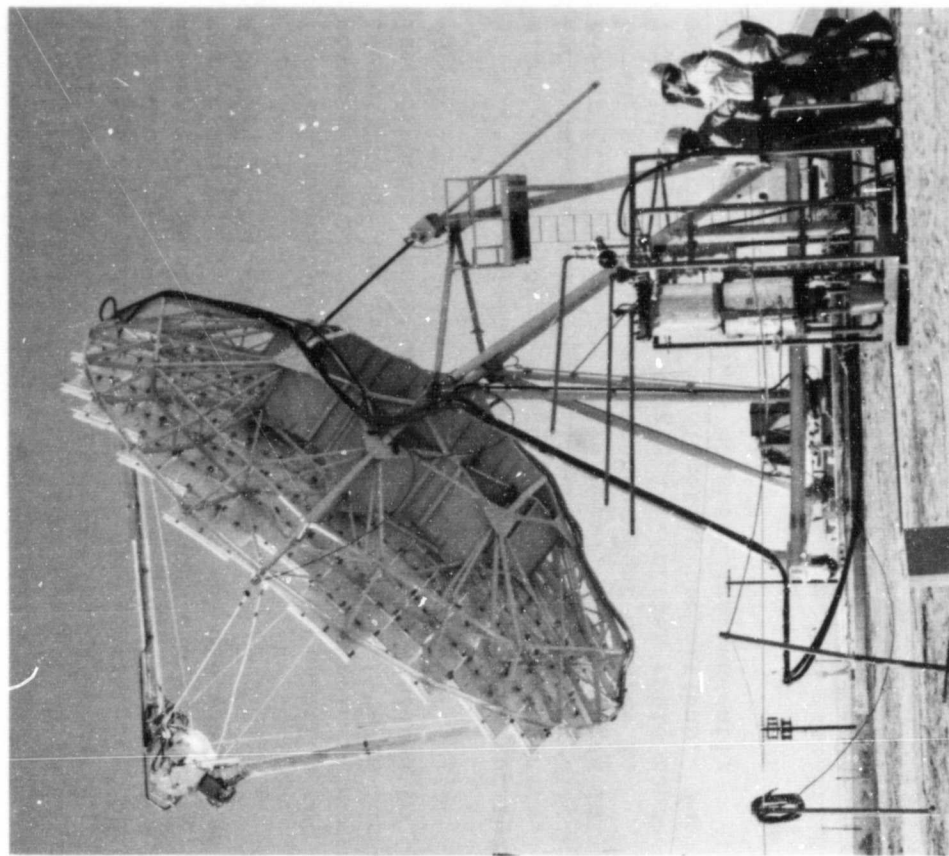
increase the rate of heat removal from the storage system.

The overall concept appears to meet the needs of thermal power systems using solar energy coupled with common methods of energy conversion.

ORIGINAL PAGE
BLACK AND WHITE PHOTOGRAPH



Vacuum chamber containing thermally cycled corrosion test capsules.

ORIGINAL PAGE
BLACK AND WHITE PHOTOGRAPH

JPL has successfully demonstrated the production of a valuable chemical and fuels from agricultural wastes utilizing concentrated solar thermal radiation as the only energy source.

Corncobs were the feedstock and, after hydrolysis with 5 percent sulfuric acid, were processed with solar-generated steam to convert their hemicellulose content (nearly 17 percent by weight) to a pseudo-aromatic aldehyde (furfural) with a high market value (\$6.20/gallon). Chemical extraction with dichloromethane saved the use of thermal energy normally wasted in distillation for water separation.

The furfural so produced (with a 500-ppm special additive) was tested as a fuel in a four-cylinder diesel engine. The energy content of furfural being lower than that of regular diesel fuel, the power level was lower for the same fuel flow rate. Also, the exhaust was smokier. Nevertheless, the engine ran successfully. This demonstrated the feasibility of producing a substitute diesel fuel with agricultural wastes and solar thermal energy.

Other feedstock are being characterized in a simulated solar reactor. Peanut shells, rice hulls, sugarcane bagasse, and napier grass are being studied to aid specific communities that have approached JPL for technical advice. The large "spent mass," usually in excess of 80 percent of feedstock by weight, is being biologically processed to yield other valuable chemicals, including butanol which can be used directly (or blended with regular diesel fuel up to 50 percent by volume) in a diesel engine.

A solar thermal energy collector at Edwards Test Station was used to process corncobs with solar-generated steam to produce furfural for fuel. The corncobs are in the boiler unit under the concentrator dish.

ACOUSTIC DIAGNOSTICS OF TURBULENT COMBUSTION

The search for rapid, non-intrusive means of monitoring the efficiency of turbulent combustion in industrial furnaces led to an investigation of acoustic emission from turbulent flames. It was discovered that the superficially random noise field contained valuable information about the combustion zone and that any change in the operating conditions was discernible as a change in the acoustic spectrum.

The responsiveness of the acoustic spectrum to changes such as Reynolds number and air/fuel ratio was identified as the key to acoustic diagnostics in turbulent flames. Acoustic imaging has been employed to obtain localized data with non-interference.

Acoustic emission spectra were obtained from small diameter laboratory burners, two commercial burners, and a large burner in the firebox of a Babcock-Wilcox Boiler (150,000 pounds steam/hour). The changes in burner size and firing rate represent changes in Reynolds number, and changes in air/fuel ratio represent departure from stoichiometric proportions. The combustion efficiency was measured independently through gas analyses.

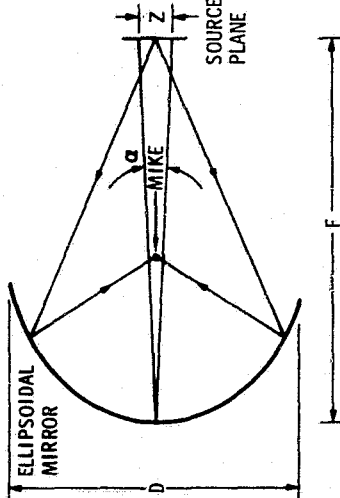
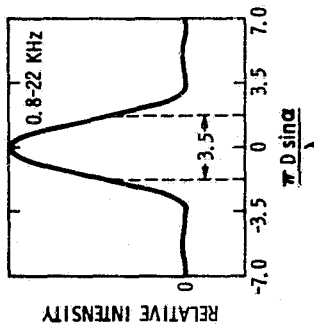
The content of acoustic emission when classified in terms of the scales of turbulence provides direct insight into the degree of turbulent mixing and thus into the rate of mixing-controlled combustion. If acoustic emission measurements are localized to receive acoustic emission from selected regions of the turbulent flame, it is possible to obtain a reaction profile along the length of the flame. Such localization of measurements is made possible by an ellipsoidal acoustic mirror/microphone (EAMM) assembly.

Since chemical combustion rate is governed by turbulent mixing in many cases, the variation in

acoustic output at frequencies corresponding to scales of turbulence should correlate with variation in combustion rate along the flame length.

Further studies using the EAMM should help unravel the mysteries of turbulent combustion and supply a viable mathematical model for characterizing turbulent combustion by acoustic emission data.

ORIGINAL PAGE IS
OF POOR QUALITY

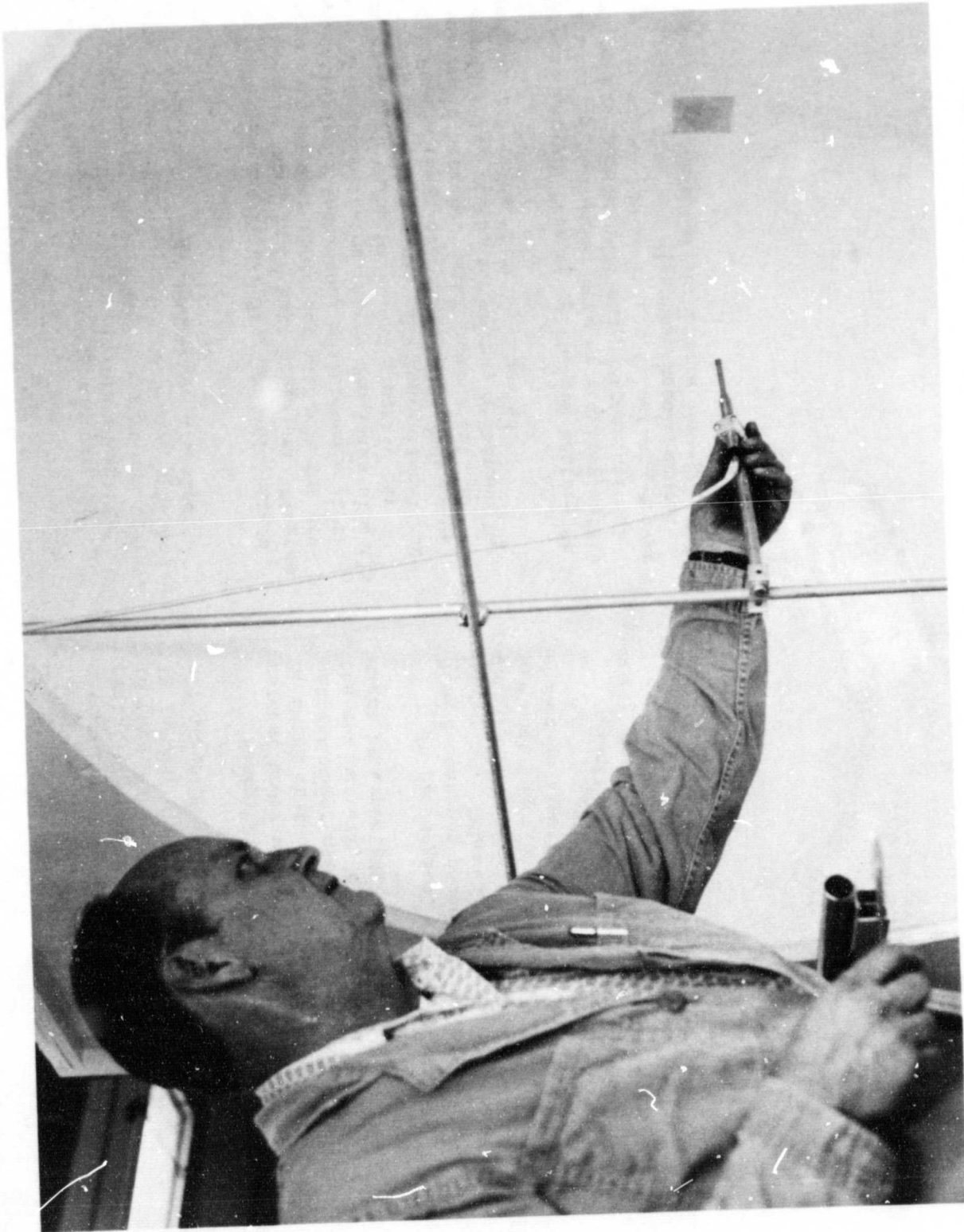


$$\text{RESOLUTION: } Z \cdot \lambda \left(\frac{3.5F}{\pi D} \right)$$

SIZE OF TURBULENT ZONE: $\eta/L \approx R^{-0.25}$

Schematic shows how acoustic imaging works in the EAMM assembly. Graph gives a profile of relative intensity results.

ORIGINAL PAGE
BLACK AND WHITE PHOTOGRAPH



A JPL investigator is shown using the small microphone to locate the focus of the acoustic mirror for the turbulent flame combustion study.

QUASI-BIPOLAR LEAD-ACID BATTERY

The Quasi-Bipolar, a new lead-acid battery structure under JPL development, offers advantages in terms of energy density, power density, and energy efficiency. Under high-power and deep-discharge applications, significant life advantages are also expected.

The predicted energy density, when discharged at the three-hour rate, is 50 watt-hours per kilogram — compared with 30 watt-hours per kilogram for conventional batteries. Laboratory measurements at the cell level have demonstrated energy densities slightly in excess of the 50 Wh/kg mark. An electric car which achieves a 60-mile range with conventional batteries will have a range of roughly 100 miles using the new lead-acid battery. With improvements in motors, controllers, gears, and tires, a further increase to some 150 miles might be expected.

The most notable feature of the new battery is an extraordinarily high power density — approximately 400 watts per kilogram at full charge (conventional lead-acids run around 120 watts per kilogram). Power levels of greater than 400 W/kg have been measured in the laboratory. An electric vehicle incorporating

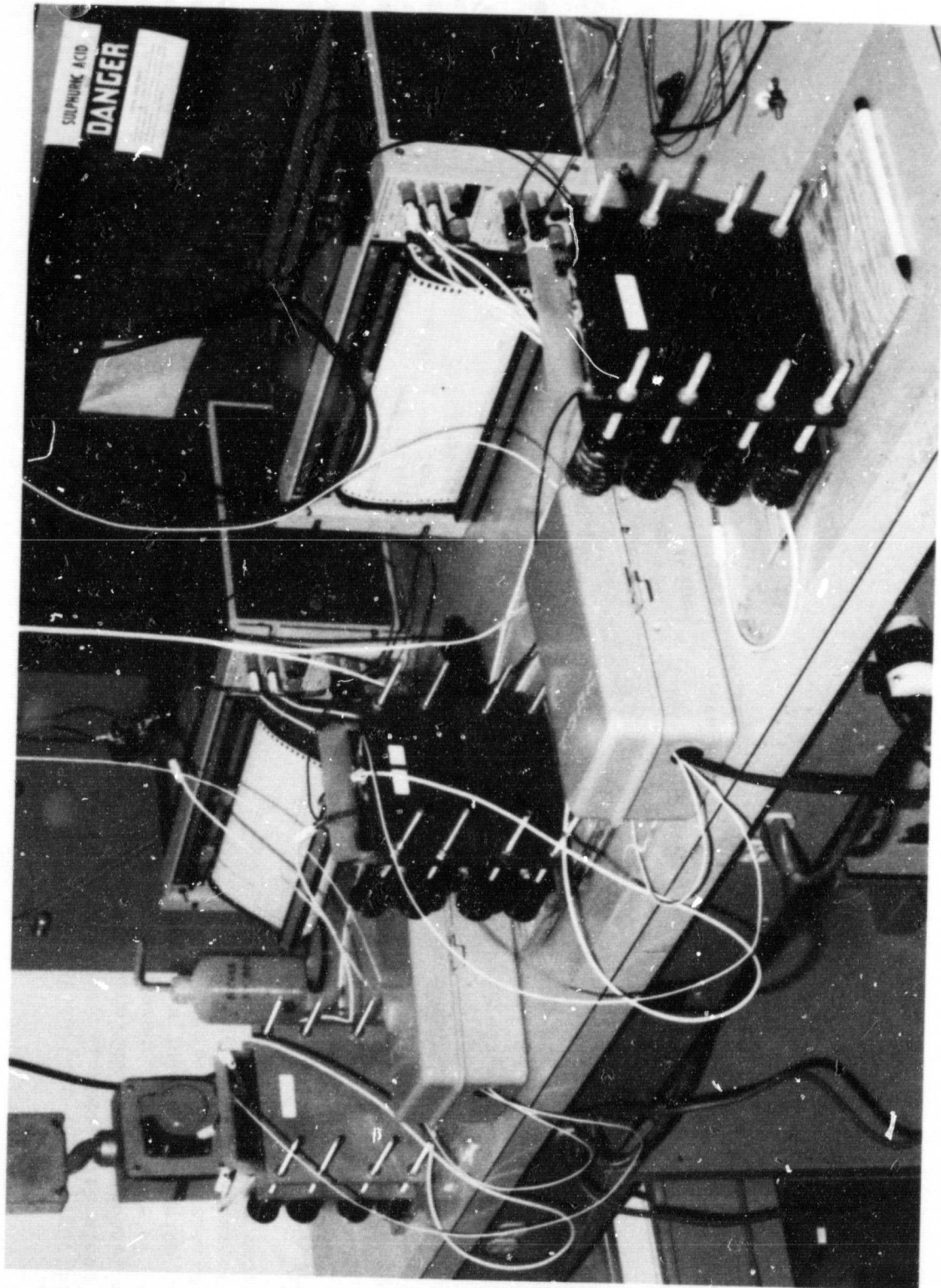
a combination of the Quasi-Bipolar Battery and a suitably powerful motor-control system is predicted to have a 0 to 60 mph acceleration time of less than 12 seconds (conventional electric cars are virtually all above 30 seconds).

Energy efficiency is expected to be around 90 percent under electric vehicle conditions. It should be noted that conventional batteries run around 85 percent under similar conditions. Accordingly, with the new battery, a five percent savings in electricity might be expected.

In production, the new battery is expected to have a cost per pound equivalent to conventional batteries. However, due to an increased energy density and a predicted increase in life, the cost per unit function (cost per unit energy throughput) should be significantly lower.

Sealed, maintenance-free techniques are currently being developed for conventional lead-acid batteries. The Quasi-Bipolar Battery is amenable to these techniques and should lower costs and improve safety and adaptability.

ORIGINAL PAGE
BLACK AND WHITE PHOTOGRAPH



Laboratory setup for Quasi-Bipolar Battery development and testing.

An electrical discharge technique developed by JPL has shown marked efficiency in destroying aggregated diesel fuel particulates. The method -- an extension of NASA technology for measuring carbon fiber particulates -- holds promise for reducing emissions from diesel-powered automobiles.

The destruction takes place between close-spaced, comb-shaped electrodes which are charged alternately at opposite polarity of 500 to 1000 volts. When the engine exhaust -- carrying particulates generated by the incomplete combustion of diesel oil -- flows through the electrodes, the particulates trigger sparks which generate a plasma leading to the ignition and combustion of the carbonaceous particulates to gaseous products.

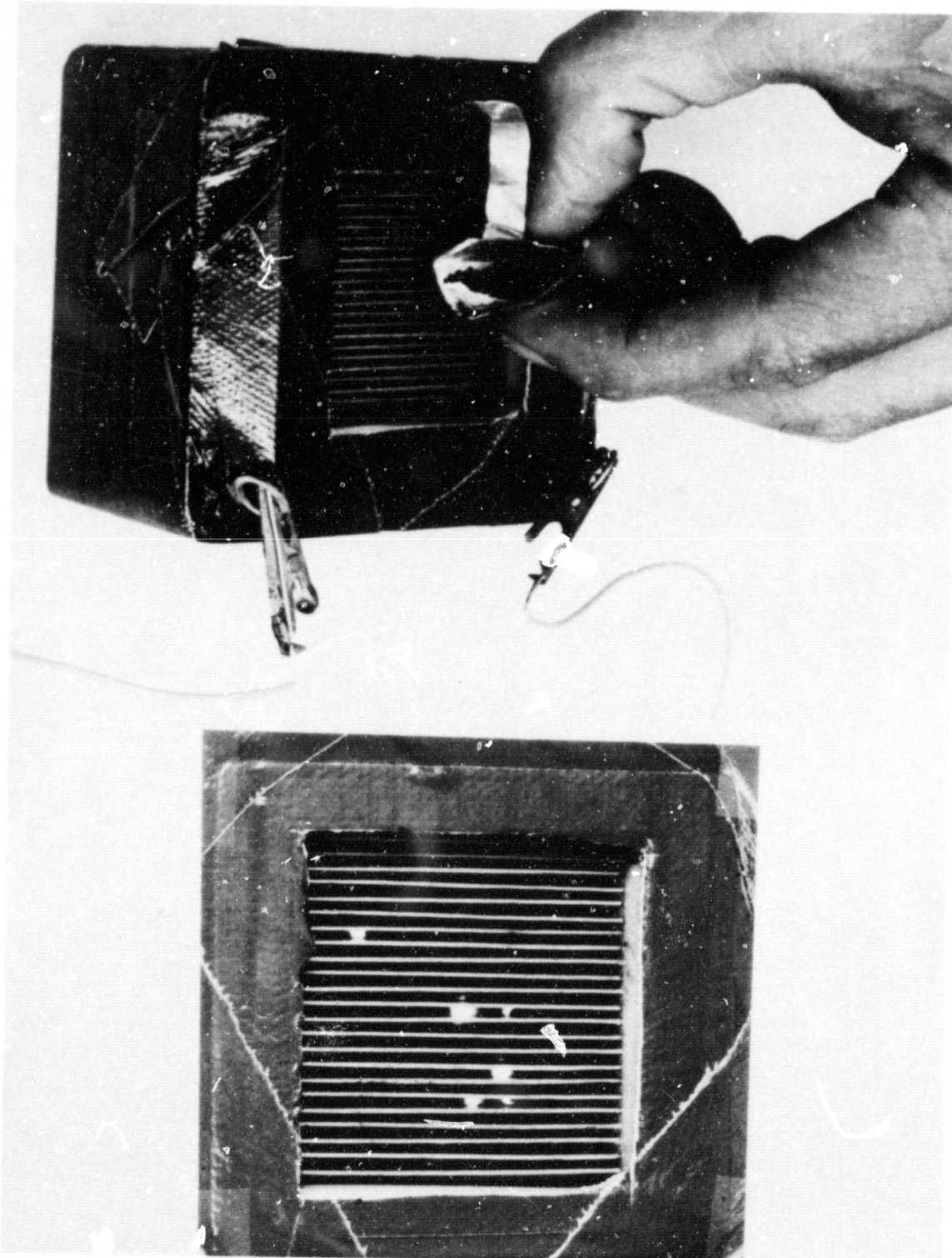
Test results to date:

- (1) The technique effectively destroyed particulates when they were aggregated from submicron size into particles several micrometers in diameter. Destruction efficiency as high as 70 percent was attained and could reach 80 to 95 percent with improved hardware design.

- (2) The major product of the destruction process is carbon dioxide, with minor amounts of carbon monoxide, hydrocarbons, nitrogen oxides, and ozone. The rates of these emissions by a full-scale device are estimated to be 20 to 100 times smaller than those specified by the Environmental Protection Agency for light duty vehicles.
- (3) The electric power required for such a destruction device is 50 watts or less, affordable by light duty vehicles. This efficiency is attributed to the release of energy by the particulates through their own fast combustion.
- (4) One problem remaining is how to dynamically agglomerate exhaust particulates. Concepts such as self-release filters and a fluidized-bed particulates agglomerator are being explored.

Funding for the emission work came from the Federal Department of Energy and the California Air Resources Board.

ORIGINAL PAGE
BLACK AND WHITE PHOTOGRAPH



Static particulates destruction test using agglomerated particles in powder form. (Left) Powder being introduced to the comb grid. (Right) Particulates being ignited by the arc plasma and destroyed by combustion.

III. Earth Orbital Applications

PRECEDING PAGE BLANK NOT FILMED

GLOBAL MAPS OF WATER VAPOR, WIND SPEED, AND WAVE HEIGHT

The NASA-JPL Seasat has provided the first global pictures from space of water vapor, wave height, and wind speed over the oceans. The satellite, launched in 1978, also measured atmospheric liquid water, sea-surface temperature, and sea-surface topography with improved accuracy over results from previous satellites.

The instrumentation included three active microwave radars, a passive microwave radiometer, and a passive visible and infrared radiometer. Because of relative insensitivity to cloud cover, microwave sensors provide useful measurements of the sea surface in all weather conditions.

The water vapor was measured by the Scanning Multichannel Microwave Radiometer (SMMR), and the wind speed and wave height were measured by the altimeter. The SMMR and scatterometer are also capable of measuring wind speed at the sea surface, but their measurements are not expected to differ qualitatively from the altimeter readings presented here.

The latitudinal banding of water vapor values reflects the higher water vapor saturation level of

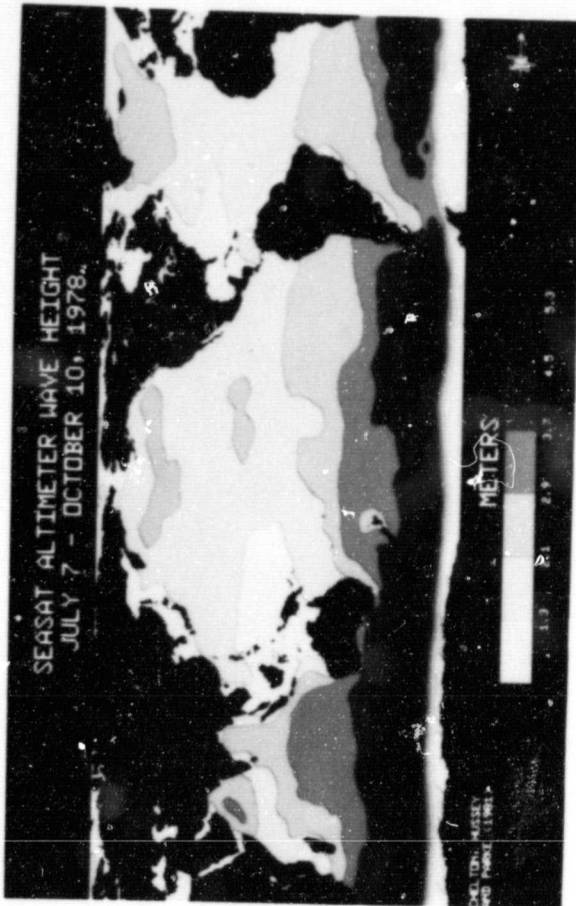
warm, tropical air compared to cooler air at high latitudes.

All of the classical features of the wind field are evident in the wind speed picture. The most prominent feature in the wind field is the band of extremely high wind speed in the southern hemisphere winter storm region between 50°S and Antarctica (especially southwest of Australia).

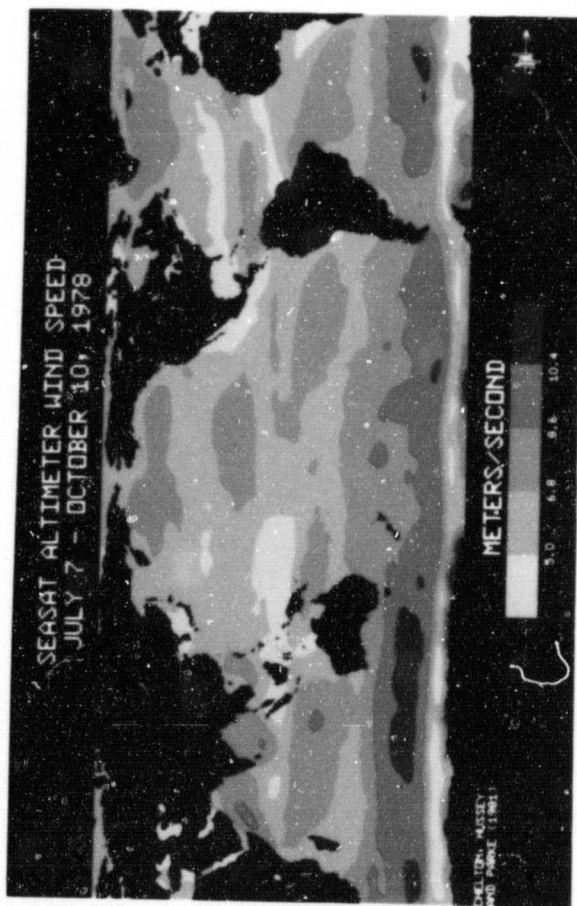
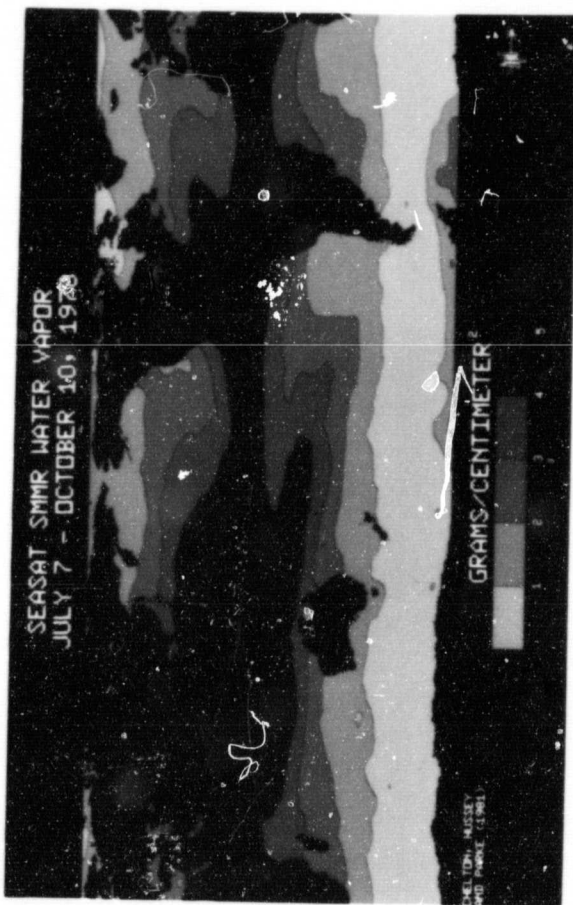
The wave height picture is believed to be the first accurate global wave map ever produced. Wave heights in the northern hemisphere are generally small (2-3 meters). Largest wave heights are found in the southern ocean high wind speed region, especially southwest of Australia where mean wave height is greater than 5.5 m. Smallest waves are found in the western Atlantic and Pacific Oceans.

These geophysical maps demonstrate the unique ability of satellites to provide global measurements of sea-surface conditions. This will prove especially useful in data-sparse regions such as the southern hemisphere. It is anticipated that further analysis of the data will ultimately lead to a better understanding of the process of wind wave generation and improve forecasts of world-wide sea state.

Figure (opposite page): Average global Earth distribution of surface wind speed, wave height, and atmospheric water vapor for period 7 July through 10 October 1978 as determined from analysis of Seasat data.



ORIGINAL PAGE
COLOR PHOTOGRAPH



ORIGINAL PAGE
COLOR PHOTOGRAPH

PRECEDING PAGE BLANK NOT FILMED

A high-speed digital Synthetic Aperture Radar (SAR) processor has been developed which is capable of processing a 100- x 100-kilometer Seasat SAR image in 2.5 hours. The processor utilizes a programmable host computer (a System Engineering Laboratory 32/55) along with three parallel array processors (by Floating Point System, Inc.) attaining an overall arithmetic processing speed of 36 million operations per second.

The system employs advanced SAR algorithms along with state-of-the-art parallel processing techniques to achieve this extremely high throughput rate in an economical fashion.

Output products, such as the image of the Los Angeles basin, contain 64 million picture elements (pixels) and are recorded onto film to form a map-compatible, rectified image at a scale of 500,000 to 1. The imagery is being produced on a routine basis in support of a variety of radar remote sensing investigations.



Digitally processed Seasat SAR image of the Los Angeles basin. The image was produced by a high-speed processing algorithm developed at JPL.

TECTONIC STUDIES IN THE CARIBBEAN WITH SEASAT RADAR IMAGERY

Studies of crustal deformation in the northern Caribbean Sea using images made by the Seasat Synthetic Aperture Radar (SAR) developed a better understanding of the complex geology of the area including Jamaica, Puerto Rico, and Hispaniola, the island shared by the Dominican Republic and Haiti.

Such detailed studies could lead to improved techniques for identifying mineral and metal deposits and increase the ability to predict seismic risk. Observed topographic anomalies in the SAR images indicate recent tectonic activity. The imagery for Jamaica has enabled a synthesis of the orientation and relative vertical displacements of major earthquake faults.

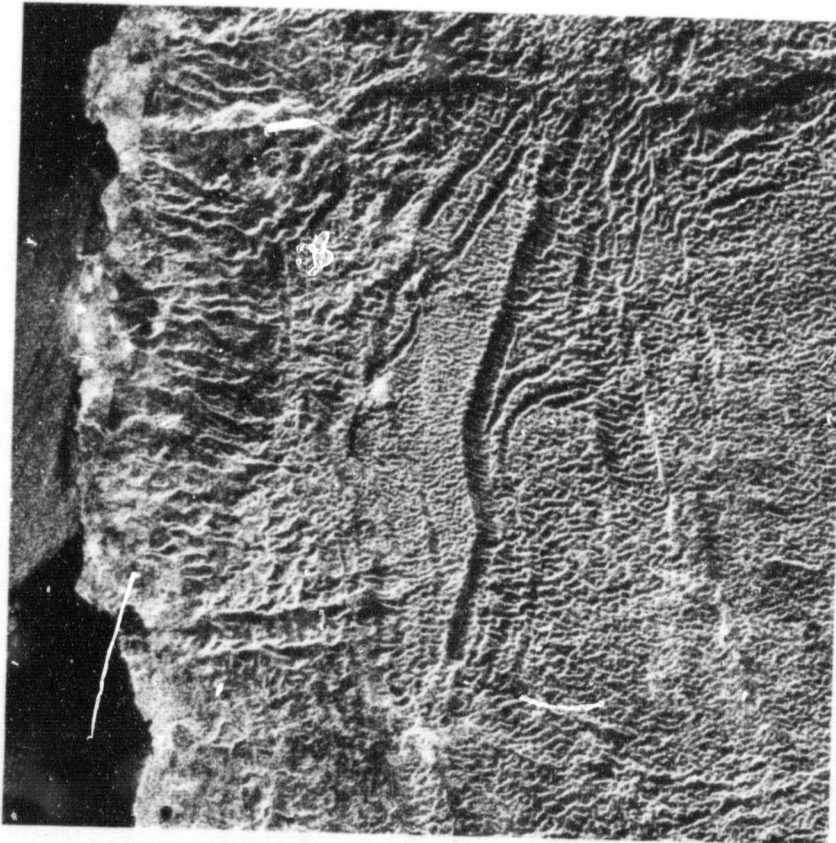
Studies of crustal deformation in the northern Caribbean Sea using images made by the Seasat Synthetic Aperture Radar (SAR) developed a better understanding of the complex geology of the area including Jamaica, Puerto Rico, and Hispaniola, the island shared by the Dominican Republic and Haiti.

The seismically active northern Caribbean plate boundary is an excellent geological analogue to the San Andreas Fault in California.

One of the most prominent faults in the Caribbean islands is the Duanvale system running through Jamaica's north coast. Detailed studies were undertaken of this fault, one of which is depicted in the accompanying figure.

The fault interpretation map of the area shows two major zones of east-west lineaments with a set of west-northwest lineaments running between them. This latter set is characterized by strongly lineated Karst ridges, suggesting rapid, continuing deformation.

ORIGINAL PAGE IS
OF POOR QUALITY



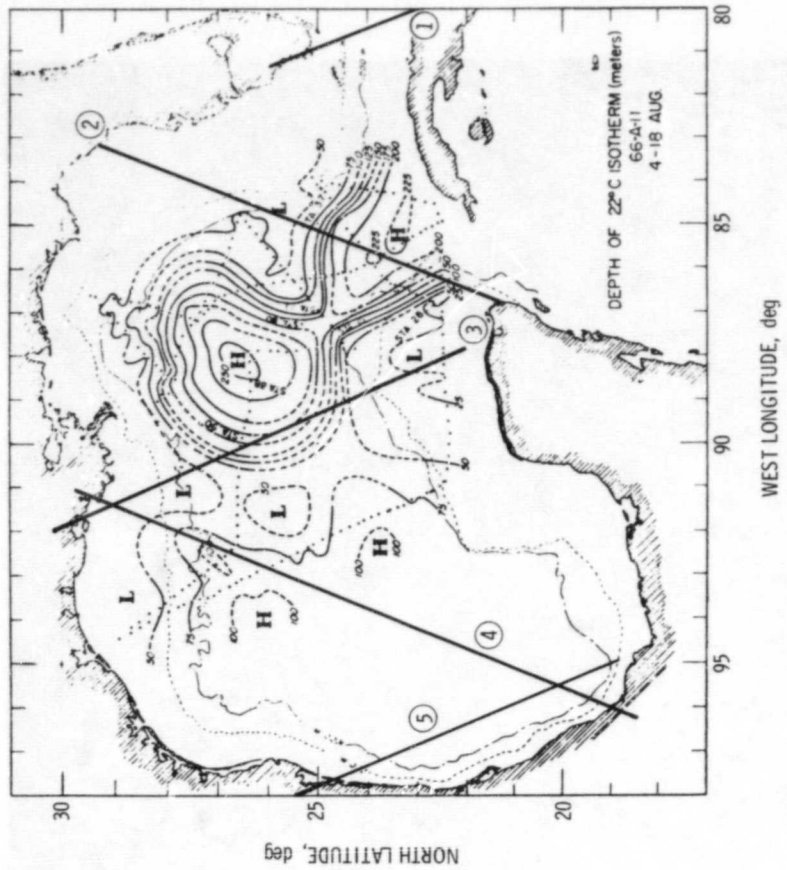
Study of the eastern segment of the Duanvale fault located on the north coast of Jamaica.

Data from the Seasat altimeter during the satellite's 1978 passage over the Gulf of Mexico confirmed sea-based numerical models of a large anticyclonic eddy of the gulf's loop current. This variable current is the primary source for the Gulf Stream.

The altimetric observations were recorded at a time when the eddy had broken off the loop current and begun drifting southwestward. The sea-surface height differences from the altimetric readings are shown in the left figure (opposite page), those from the numerical model in the right. The agreement indicates that the combination of methods can provide a better understanding of the mesoscale processes in the Gulf of Mexico.

The anticyclonic eddies, which occur every 8 to 15 months, are from 300 to 400 kilometers in diameter and have a dynamic height signature of 50 to 60 centimeters. They are the largest known ocean eddies. They drift westward, dominating circulation in the gulf until they dissipate.

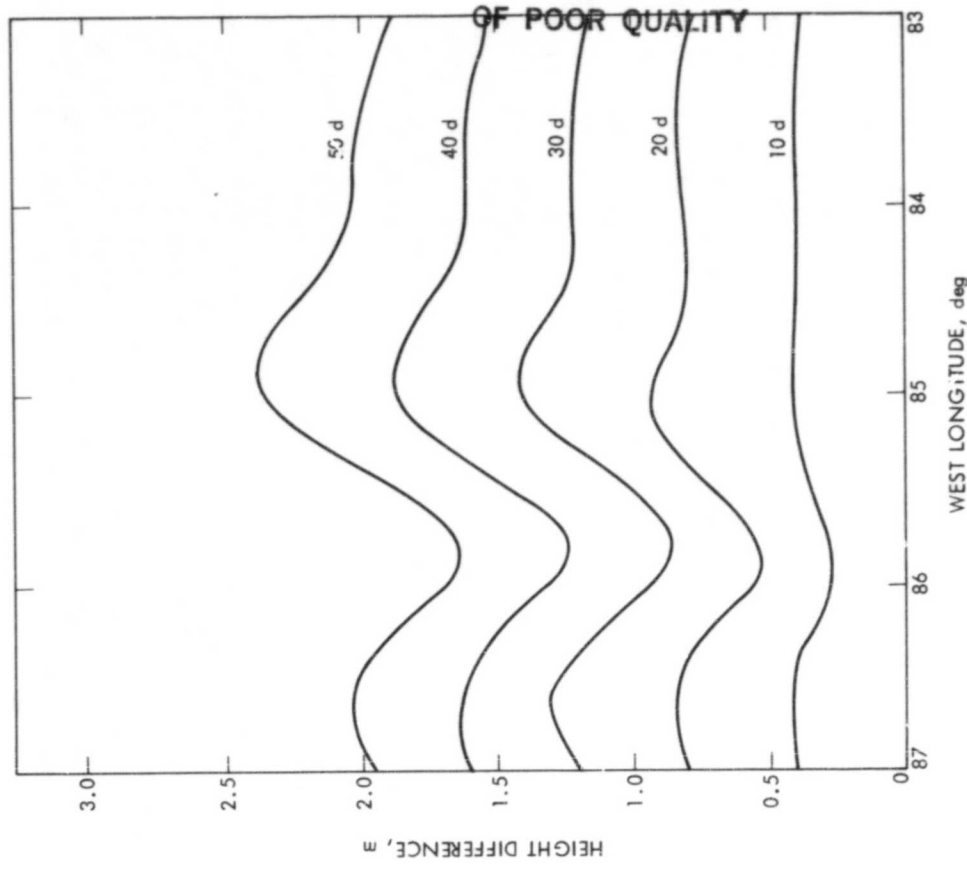
An expendable bathythermograph transect from Galveston to Yucatan confirmed the location of the eddy at essentially the position determined by the Seasat altimeter. The Naval Oceanographic Research and Development Activity provided the sea truth data for the numerical model results in this study. The gulf loop current normally flows from Yucatan to Florida but at other times extends northward, nearly to the Mississippi Delta.



Topography of the 22°C isothermal surface in the Gulf of Mexico for August 1966. An anticyclonic eddy is about to separate from the loop current. This is similar to the configuration that the Seasat altimeter found in 1978. Also shown are Seasat ground tracks.

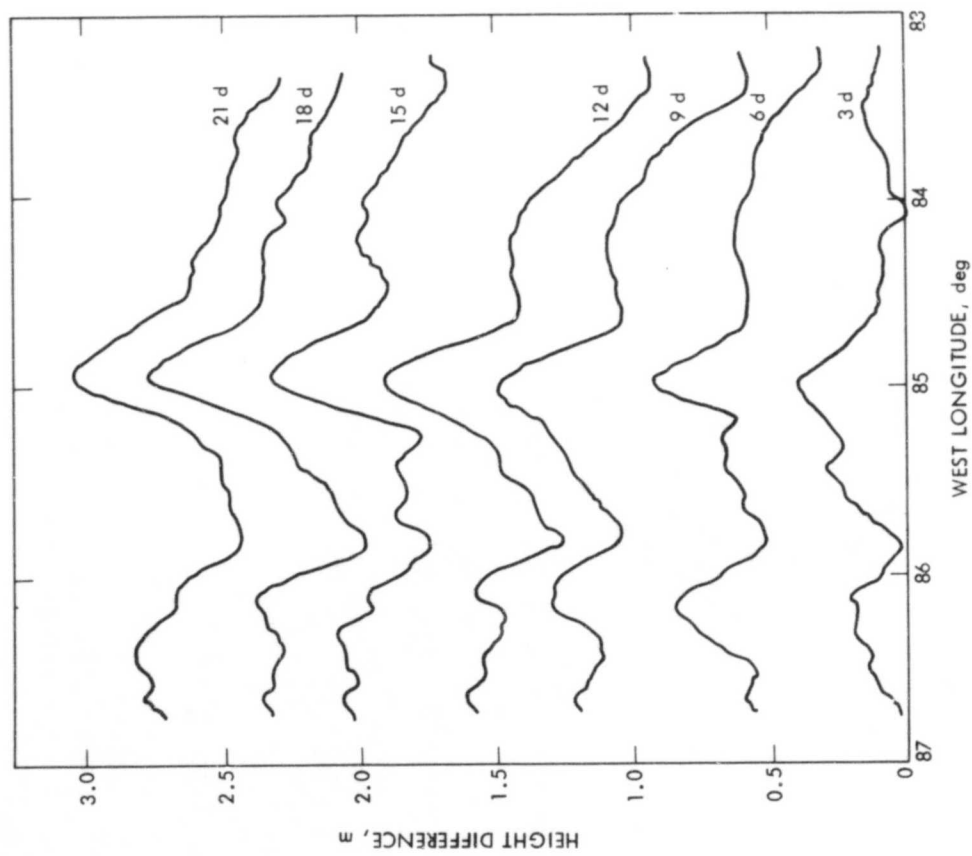
ORIGINAL PAGE IS
OF POOR QUALITY

ORIGINAL PAGE IS
OF POOR QUALITY



Gulf of Mexico sea-surface height changes over a 21-day period (September 17-October 8, 1978) at 3-day intervals as determined by the Seasat altimeter along ground track 2.

Sea-surface height changes from a numerical circulation model of the gulf at 10-day intervals along a line corresponding to ground track 2. Note similarity to the altimeter results. Surface elevation profiles of this nature occur only when the loop current is shedding an eddy.



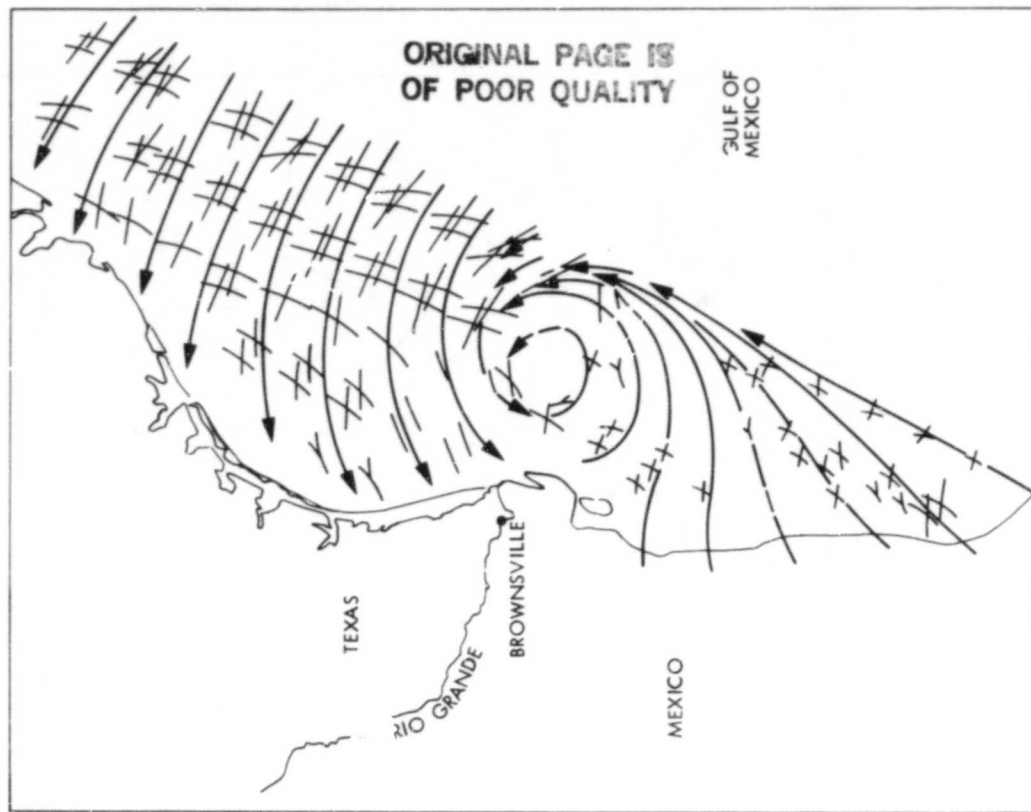
SEASAT SCATTEROMETER DETECTION OF A TROPICAL DEPRESSION IN
THE GULF OF MEXICO

In recent analysis of data from the September 9, 1978, Seasat pass over the Gulf of Mexico, researchers from JPL, UCLA and the Canadian Atmospheric Environment Service found that the scatterometer aboard the satellite had clearly defined a tropical storm which weather services in New Orleans and Texas had been unable to identify with conventional data and weather satellite imagery. The scatterometer is a radar instrument which measures surface wind speed and direction over the ocean.

The storm was discovered in the Seasat data in a research effort for the National Marine Fisheries Division (of the National Oceanic and Atmospheric Administration), in Mississippi, where prediction of rich fishing areas depends on accurate models of wind-driven currents.

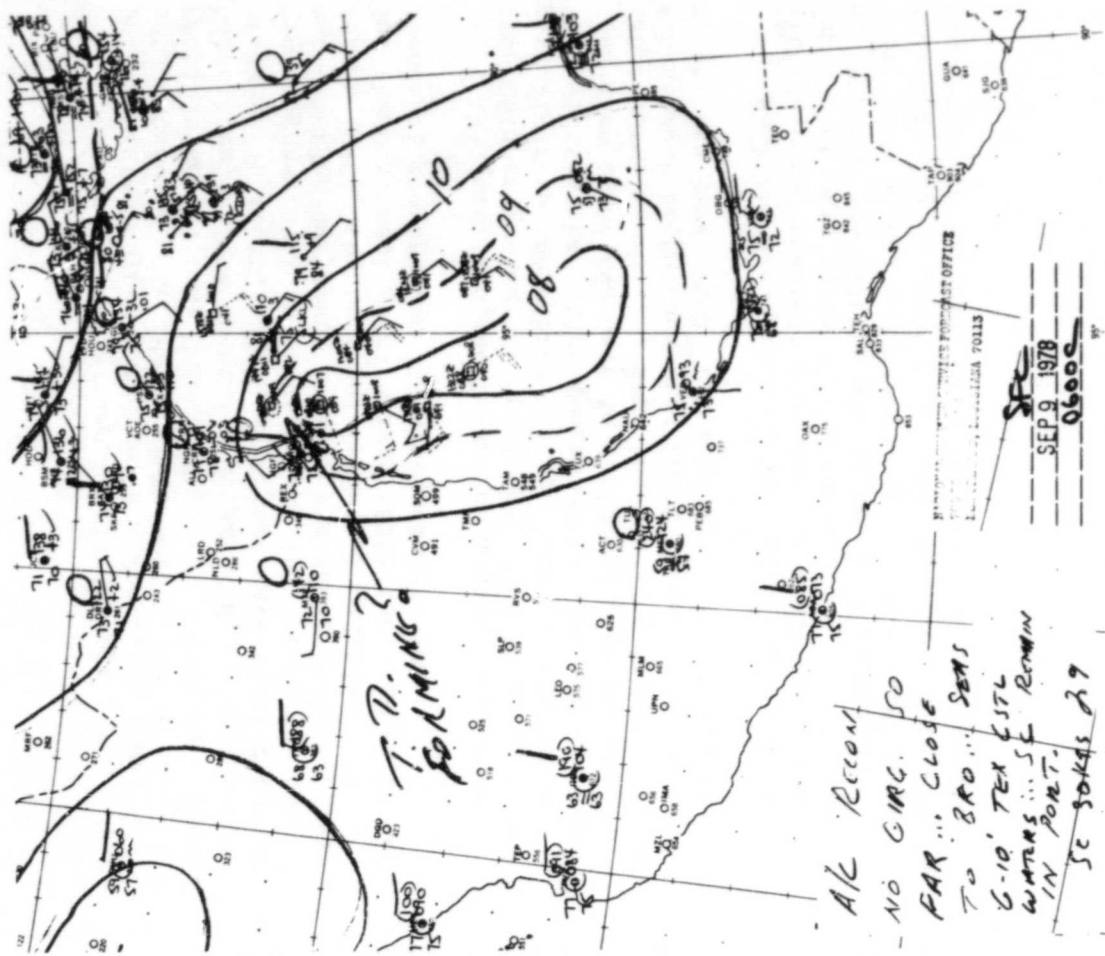
While forecasters were aware of a possible tropical depression on the date, neither GOES satellite imagery nor reconnaissance aircraft could locate it. The scatterometer data recorded that morning disclosed a marine circulation system with winds up to 28 knots swirling over the gulf. If the data had been available in real time, the National Weather Service could have forecast the fairly intense tropical storm at least 13 hours before the subsequent verification about 125 miles off the coast of Brownsville, Texas.

The observations have been acknowledged by the National Weather Service in New Orleans which furnished material for the composite map and notations (right figure, opposite page).

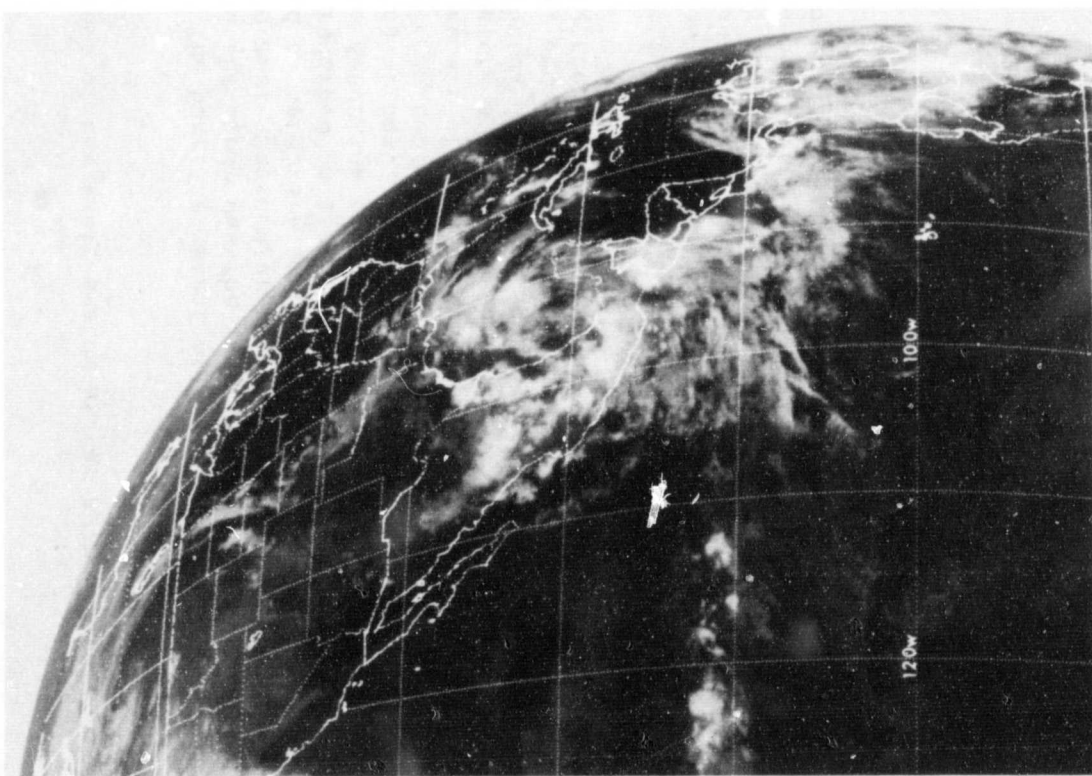


Analyzed raw scatterometer data showing streamlines (arrows) for Rev 1061 taken at 0500Z, 9 September 1978, in the Gulf of Mexico, indicating tropical depression near Brownsville, Texas. Multiple solutions result from physical relationship between probing radar signal and ocean surface characteristics measured. There are up to four vectors pointing inward toward location of each measurement site; length of vectors proportional to wind speed: 28 knots maximum, 4 knots minimum.

ORIGINAL PAGE IS
OF POOR QUALITY



Infrared imagery from GOES west geostationary satellite taken at 0445Z, 9 September 1978; no clear evidence of tropical depression in Gulf of Mexico.



NWS New Orleans Forecast Office analysis of chart for 1200Z (0600 CST), 9 September 1978 (7 hours after Seasat pass), indicating difficulty of forecast office to determine presence of the tropical depression by aircraft reconnaissance, ship reports, and analysis. Cloud imagery for this analysis time similar to figure at left.

Spurred by Landsat images, field work for a joint United States-Chinese study of the Red River Fault in Yunnan Province, in the southwestern corner of the People's Republic of China (PRC), was completed. Three Caltech geologists spent six weeks studying this large strike-slip fault, which is in some ways similar to the San Andreas Fault in California. This study was carried out under an agreement between the State Seismological Bureau (PRC), the National Science Foundation (USA), and the U.S. Geological Survey (USA) for scientific and technical cooperation in earthquake studies.

The joint program began in January 1981, when five Chinese geologists spent one month in a counter-part visit to the United States. During this month they visited the entire length of the San Andreas Fault. They also spent two days in JPL's Image Processing Laboratory, where they were introduced to digital image enhancement techniques used to clarify Landsat images of the Red River Fault for subsequent interpretation.

NASA arranged for Landsat-3 to take new images with 30-meter resolution of certain areas along the fault that were especially interesting. In February one JPL and two Caltech geologists went to China to begin work on the Red River Fault. Their field work took them from a point 50 kilometers north of the Viet Nam border to Xiaguan, with limited reconnaissance on

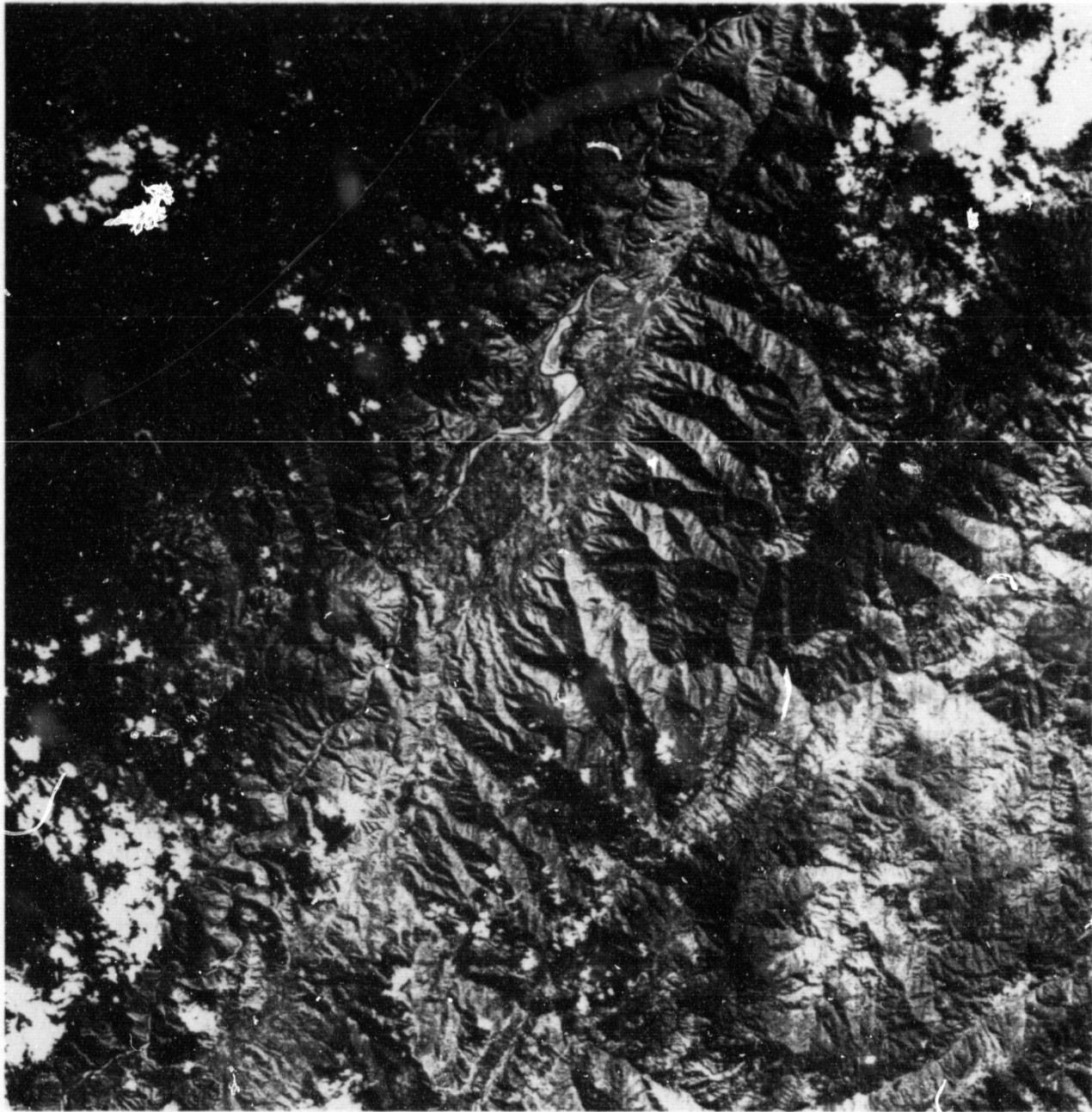
branches of the fault system as far as the Yangtze River.

The puzzling aspect of the Red River Fault that led to the study was the fact that, although it is one of the most spectacular regional faults of China as viewed on satellite images, no large earthquakes have been recorded on its principal segment. The objective was to determine its degree of activity and seismic hazard, if any. There had also been considerable debate concerning horizontal versus vertical displacements.

As a result of the joint study, all American and Chinese geologists agreed that there is abundant evidence of horizontal displacement during the last few million years, and several argued that movement has occurred during the last 10,000 years as well.

It also turned out that the fault, which is so obvious on satellite images (bounding the mountainous Ailaoshan metamorphic block), is not the principal active fault in the region. Another previously unmapped parallel fault lies in a sedimentary basin to the northeast of the Ailaoshan block. This fault was first recognized on the satellite images before the field work began. All geologists concurred that the Red River Fault has a significantly lesser degree of activity than the San Andreas Fault.

ORIGINAL PAGE IS
OF POOR QUALITY



The Landsat image that discovered the major fault lines in the People's Republic of China, later studied by Caltech-IP1 geologists.

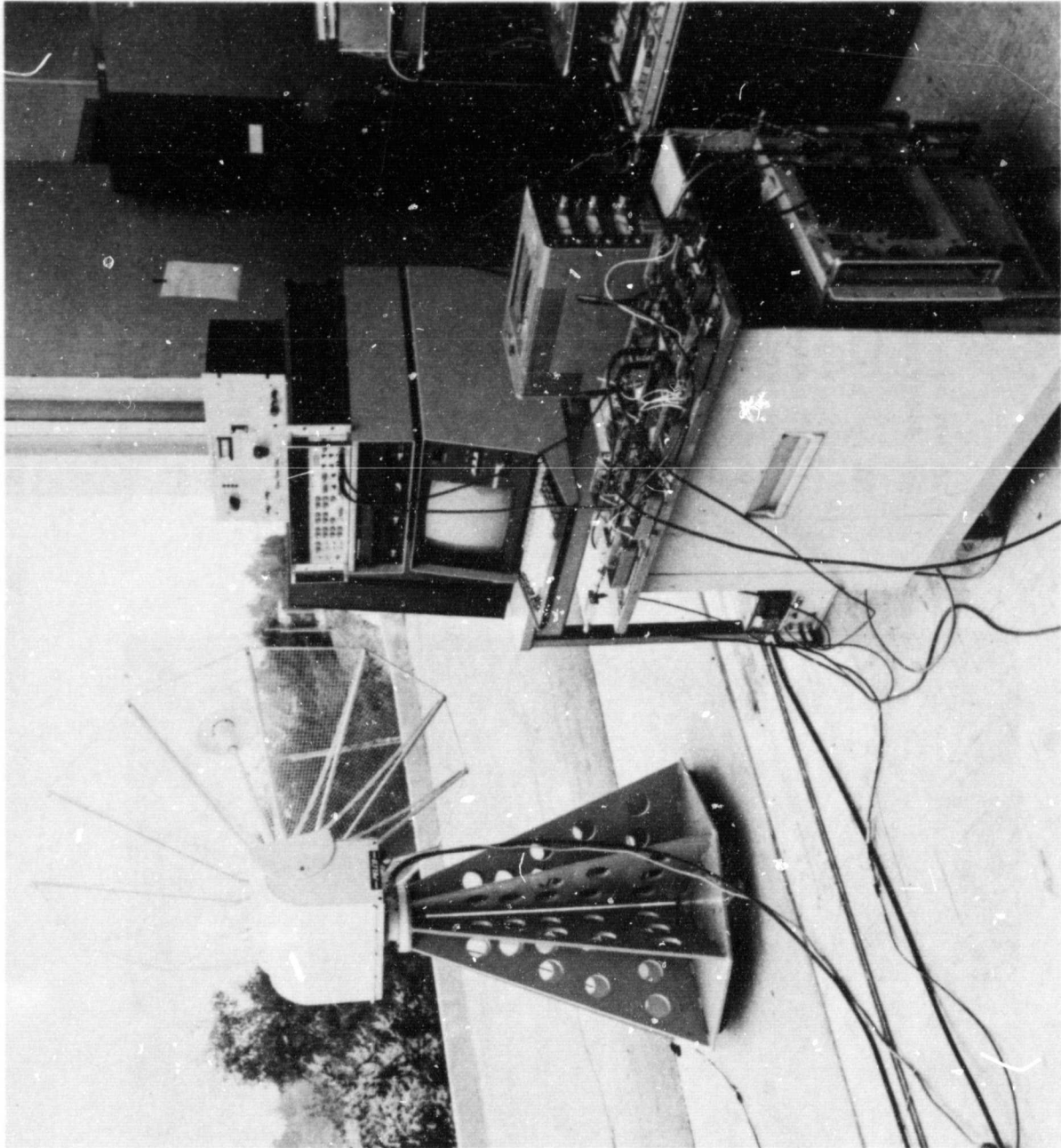
An approach to high-accuracy geodesy at low cost at distances of 20 to 200 kilometers is to use satellites as radio signal sources instead of quasars, because satellites can have signal strengths a million times stronger. A JPL concept called SERIES (Satellite Emission Range Inferred Earth Surveying) exploits the structure of the Global Positioning System (GPS) radio transmissions to construct a single-station range measurement to the satellites without having to know details of the signal design. With this technique, 0.5- to 3-centimeter three-dimensional baseline accuracy can potentially be achieved over distances of 20 to 200 km, respectively, from only a few minutes of on-site data acquisition. This potential capability has been partially demonstrated this year in a single-station experiment.

Feasibility demonstrations exhibit precisions of 30 picoseconds (1 cm) with one-second averaging for single station range. In addition, simultaneous re-

ception at the two GPS channels, 1575 and 1227 megahertz, has allowed direct calibration of ionospheric electron content equivalent to a few centimeters. By differencing one-way range measurements to two independently operated stations, a delay data type will be created that is conceptually identical to the delay observable of VLBI (Very Long Baseline Interferometry), and from which Earth crustal motion can be directly inferred.

The figure shows a breadboard of the equipment used in the initial feasibility demonstrations. The electronics and control functions were housed in a modified camper shell suitable for transport by pickup truck. In both the demonstration and actual operations, a microcomputer is used in each SERIES station for antenna pointing, which is accurate within one degree. The microcomputer also records on computer tape or floppy disc the digital data from the one-way ranging SERIES receiver.

ORIGINAL PAGE IS
OF POOR QUALITY

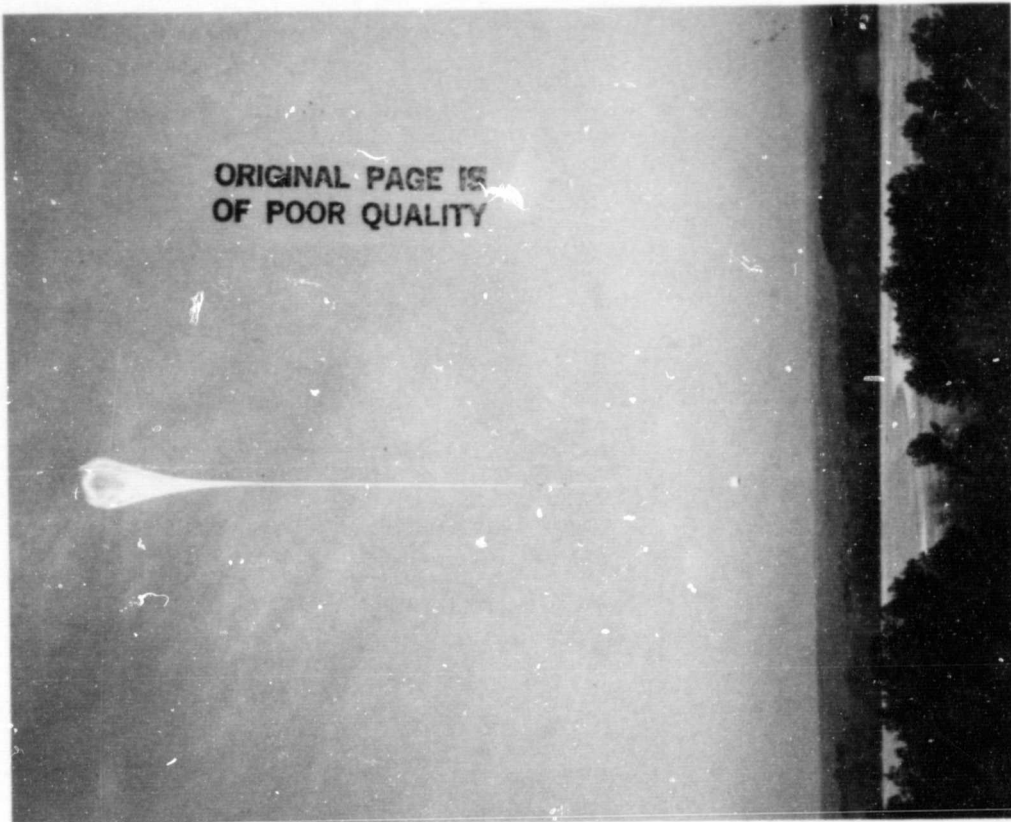


SERIES proof-of-concept station with L-band (1.2 and 1.6 GHz) reception capability for signals from the NAVSTAR Global Positioning System (GPS) satellites. Especially designed for operation with one or more similar stations to achieve few centimeter, 3-dimensional baseline measurements in near-real time. For application of crustal dynamic measurements over baseline of 20 km to perhaps intercontinental distances.

A new atmospheric measurement technique, microwave limb sounding, has been developed at JPL and successfully used from balloons to provide important data on the chemistry of Earth's protective stratospheric ozone layer. The JPL Balloon-Borne Microwave Limb Sounder (BMLS) is the first instrument to perform microwave measurements looking down through the Earth's atmospheric limb. It measures thermal emission with 105 channels located on three spectral lines near a frequency of 205 gigahertz (1.5-millimeter wavelength). The three spectral lines for which the BMLS is initially tuned are rotational transitions of ozone (O_3), chlorine monoxide (ClO), and hydrogen peroxide (H_2O_2).

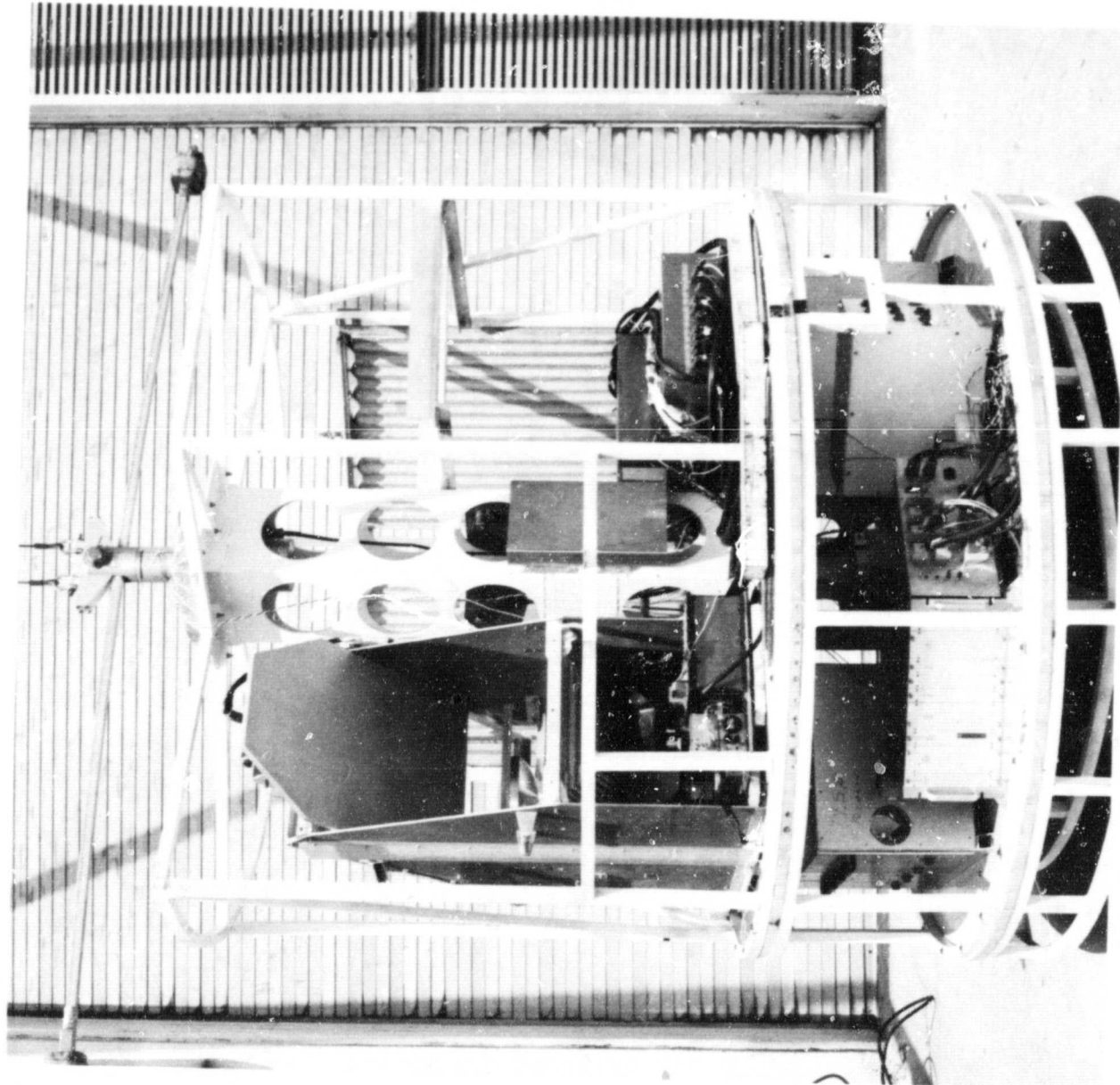
Two BMLS flights up to 40,000 kilometers were performed at the National Scientific Balloon Facility, Palestine, Texas, with the instrument performing perfectly. Results included the first measurement of the predicted diurnal variation in stratospheric ClO , the first simultaneous remote measurement of stratospheric ClO and O_3 , and the first tentative measurement of stratospheric H_2O_2 . The ClO results are important for understanding the potential depletion of stratospheric O_3 by chlorine which originates from man's technology. This is of practical importance because O_3 shields living organisms from damaging solar ultraviolet radiation. The H_2O_2 result adds to the general knowledge of stratospheric composition and chemistry as H_2O_2 may be a factor in destruction of ozone by hydrogen chemistry.

Future simultaneous flights with the BMLS and other instruments making related measurements are planned. A satellite microwave limb sounding experiment is also under study for the Upper Atmosphere Research Satellites now being considered by NASA.



The JPL Balloon-Borne Microwave Limb Sounder (BMLS) starts its first flight into the stratosphere from the National Scientific Balloon Launch Facility in Palestine, Texas, on February 20, 1981. The BMLS measures the abundances of stratospheric ClO , O_3 , and H_2O_2 . These measurements are important for improving our understanding of stratospheric chemistry and the possible depletion of stratospheric ozone by man's technological activities.

ORIGINAL PAGE IS
OF POOR QUALITY



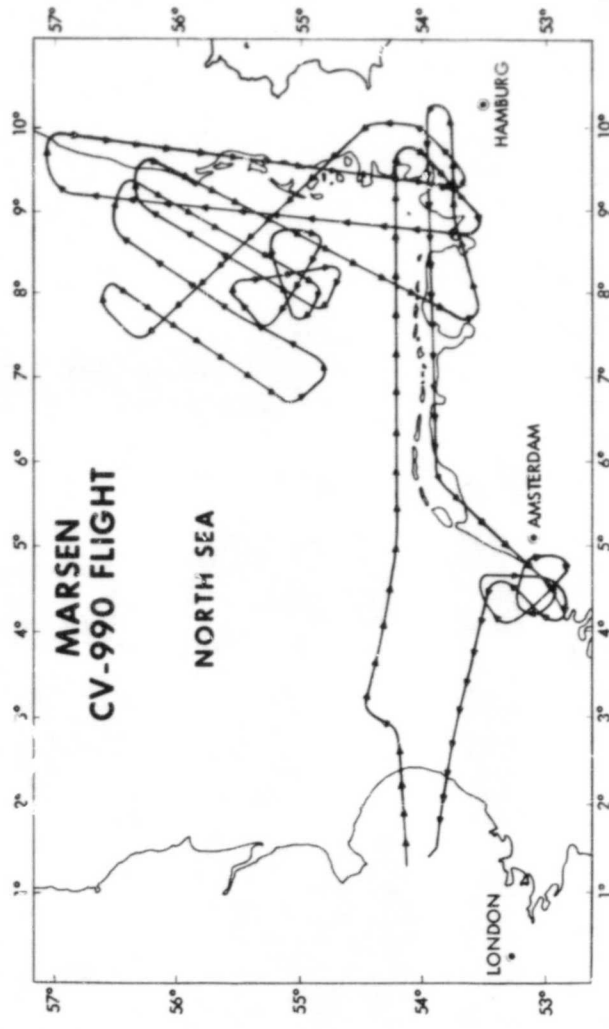
Closeup of the JPL Multisensor Gondola with the Balloon Microwave Limb Sounder mounted in the upper left. The microwave instrument measures about 2 x 4 feet in its niche in the 6-foot diameter gondola.

A multi-national large-scale experiment to investigate problems of significant importance to the oceanographic community was conducted and successfully executed under the coordination of JPL in the United States and the Max-Planck-Institut für Meteorologie in Germany. The primary objectives were to utilize the complementary capabilities provided by remote sensing (active and passive) and conventional (in situ) techniques to investigate the behavior of oceanic fronts; the generation of waves and currents by wind in finite depth waters; the dynamics of short waves, their dependence on wind speed, currents, long waves and surface containment, in relation to gaining detailed understanding of the processes by which JPL-designed imaging radars detect ocean surface phenomena.

The first phase of the experiment was conducted from August 15 to September 15, 1979, with emphasis on

detecting oceanic fronts in the German Bight area. The second phase, from September 15 to October 15, stressed the measurement of waves, currents, and wind in the German Bight and Dutch offshore areas. An extended experiment, conducted on the Dutch Noordwijk tower, obtained additional measurements under severe wind conditions.

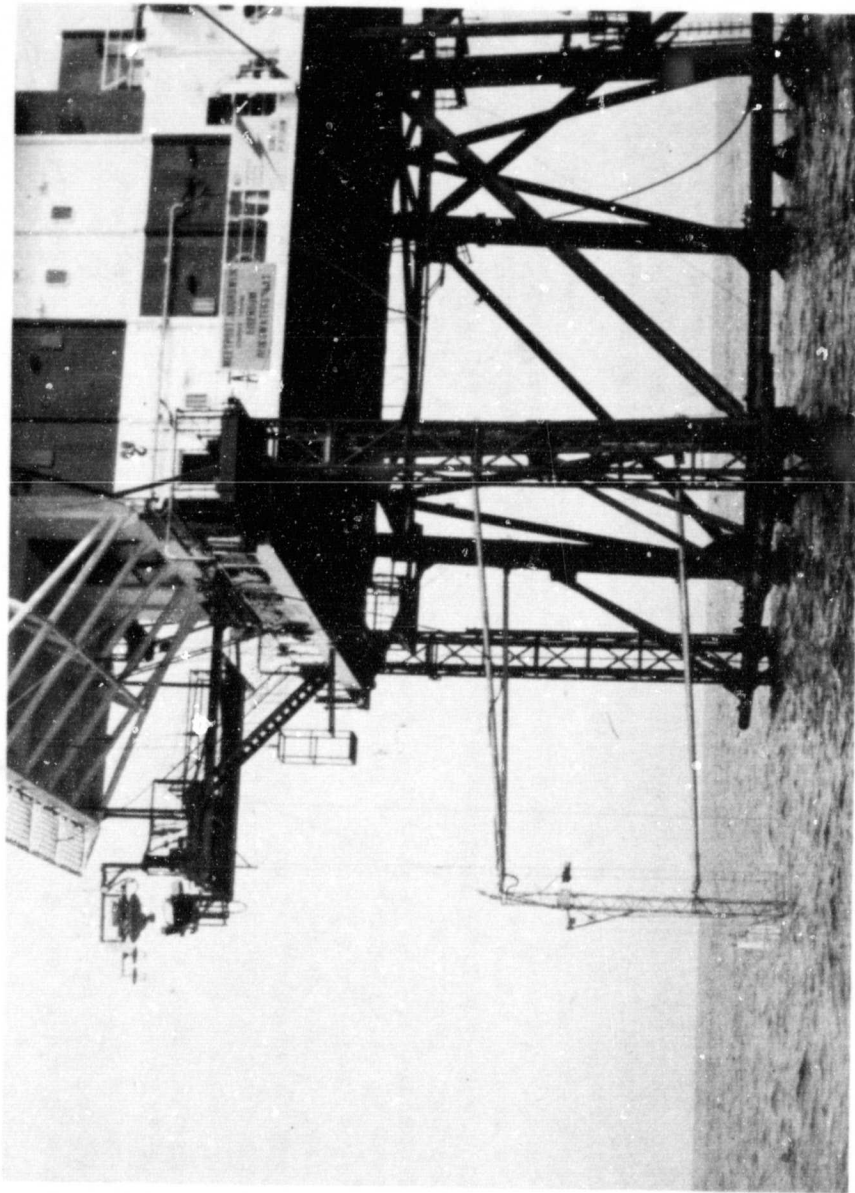
The data sets collected during MAREN were of sufficient quality to meet all scientific objectives of the experiment. A total of 29 different institutions participated in the collection of the data sets, with 19 of these institutions in Europe. Upon completion of data analysis, investigators expect to produce 35 scientific contributions to present understanding of the ocean surface processes in the North Sea area and the use of remote sensing techniques for measuring t. em.



ORIGINAL PAGE IS
OF POOR QUALITY

Flight path of NASA CV-990 aircraft during the second phase of the MAREN experiment. Remote sensing instrument carried was the JPL L-band Synthetic Aperture Radar.

ORIGINAL PAGE IS
OF POOR QUALITY



Tower at Noordwijk, Netherlands, utilized for measurements of ocean surface phenomena during the MARSEN experiment.

REGULAR SOLAR IRRADIANCE VARIATIONS RELATED TO SOLAR ACTIVE REGIONS

The Active Cavity Radiometer Irradiance Monitor (ACRIM) experiment on NASA's Solar Maximum Mission (SMM) monitored the total solar irradiance nearly continuously from launch in February 1980 through the remainder of the year. ACRIM's three Active Cavity Radiometer (ACR) sensors sustained an internal measurement precision of less than 0.005 percent during the 10 months of normal SMM operation. An independent solar irradiance experiment was conducted using a sounding rocket in May 1980, in which ACRIM's three sensors were compared with two similar ACR sensors on the rocket. All five sensors agreed to within 0.05 percent of their mean.

The results of ACRIM observations for 1980 are shown in the figure opposite. A series of regular irradiance decreases occurs with sharp dips below the mean from April through October at intervals near 24 days, followed by three more major dips through early November. Prominent maxima of total irradiance occur immediately before and after most dips.

A principal periodicity in both ACRIM irradiance and the total sunspot area was found near 24 days. The total solar irradiance measured by ACRIM has a strong inverse correlation with several indices of solar activity: The projected sunspot area, the 2800-megahertz flux, and the Zurich sunspot number.

The general character of the total solar irradiance emerging from the full set of 1980 ACRIM results is that of continuous short-term variability below the 0.2 percent level superposed on a slow long-term decrease at the rate of 0.05 percent per year. The variability results from modulation of the average solar irradiance by a combination of sunspot flux deficit and facular flux excess. The recurring pattern of solar activity maxima and the related irradiance decreases, together with the absence of

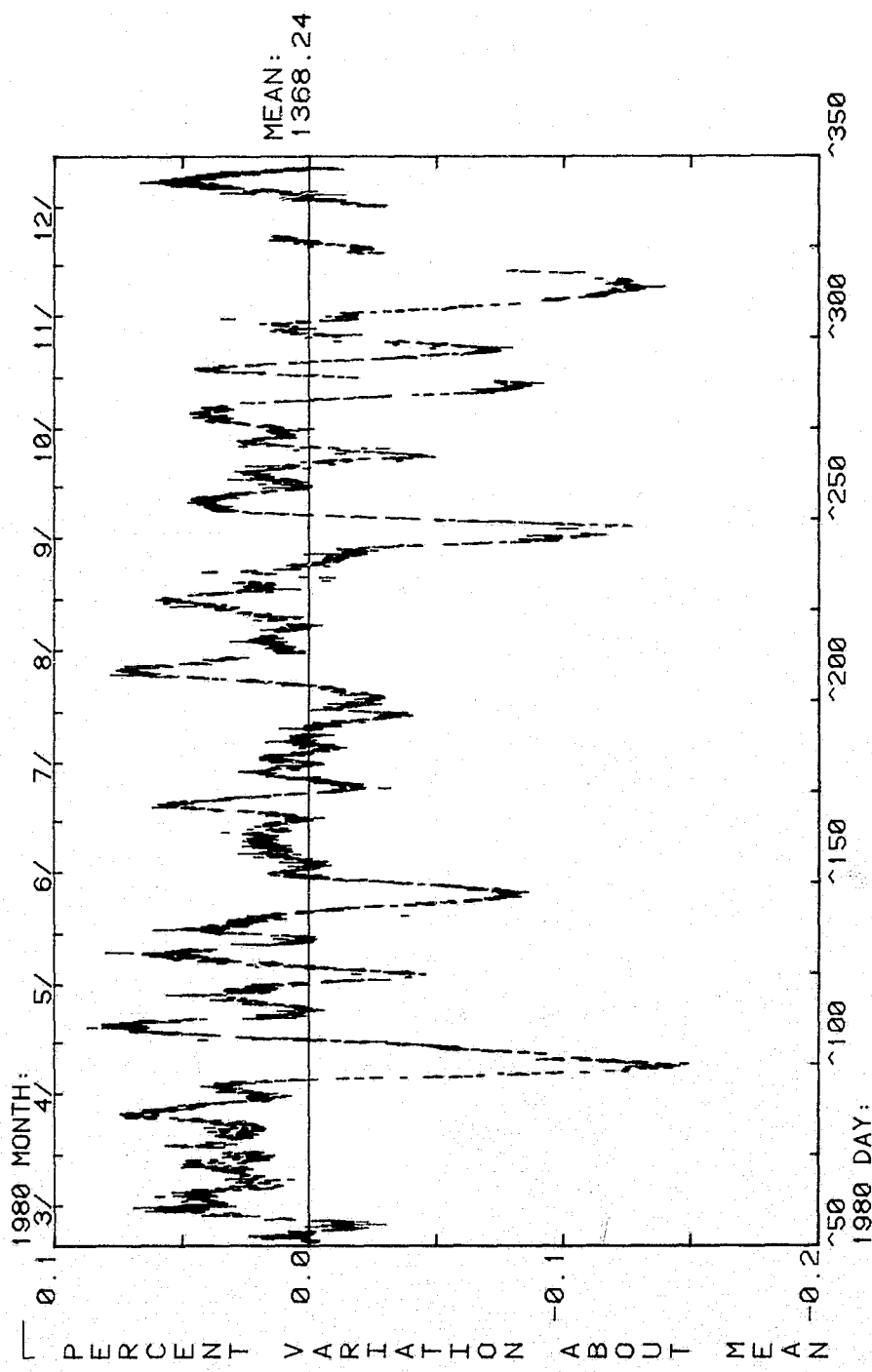
significant periodic behavior shorter than six days, supports the following scenario of solar active region evolution and irradiance modulation:

Magnetic fields in the hydrogen convection zone disrupt the outward flow of energy, resulting in the formation of sunspots. The spots decrease the total radiant flux emitted in proportion to the area of the spots and their lower temperatures.

Assuming regional energy balance over times longer than the persistence of individual active regions, the stored-up energy must eventually be transferred to space by radiation, solar wind, and other processes. What appears to be energy storage in the convection zone during the irradiance reductions is probably only an increased time required for the diverted deficit energy to reach the photosphere by longer convection paths. These paths would be expected to be the shortest possible, causing the diverted energy to be released near sunspots where faculae typically occur. Such facular areas would radiate at abnormal temperatures, having gathered both the diverted and normally convected energy.

The development and decay of sunspots and faculae during the evolution of most active regions varied in phase and duration. Evidence was the increasing ratio of plage to spot area in reappearances of active regions associated with the irradiance dips. After the spot reaches its maximum and begins to fade, the associated faculae persist, radiate away the deficit energy, then fade themselves, completing the cycle. Approximate ratios of sunspot and facular intensity to that of the quiet photosphere are 0.5 and 1.2. Most faculae were observed to have longer lifetimes and larger areas than their precursive sunspots; it is a necessary condition for the restoration of regional energy balance.

ORIGINAL PAGE IS
OF POOR QUALITY



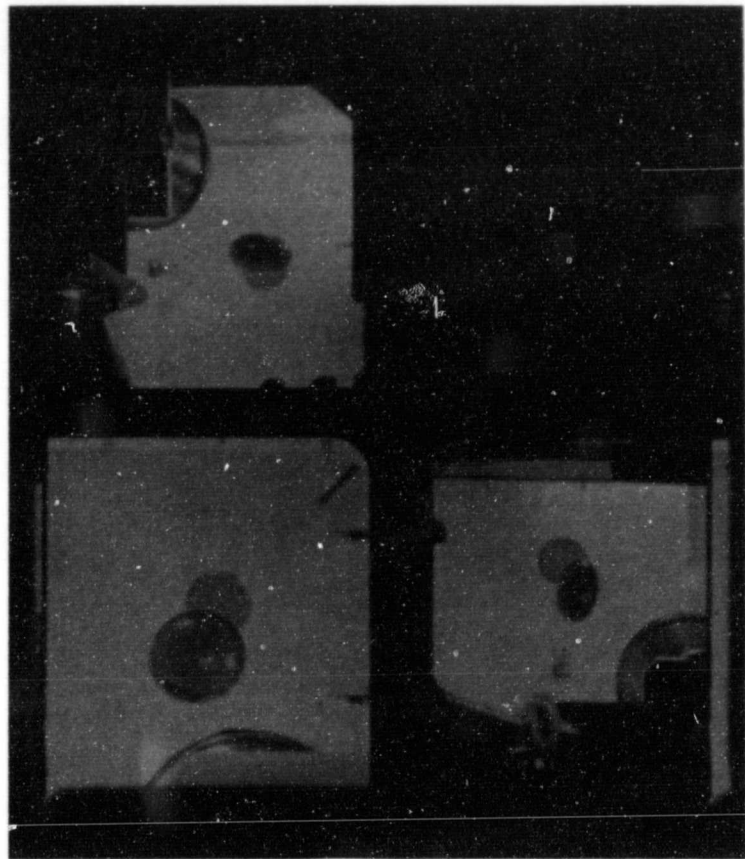
The record of 1980 ACRIM solar total irradiance observation is shown as the percentage variation about the 1368.2 W/m² mean irradiance at 1 AU over the 300-day mission period. A linear model fitted by least squares to the ACRIM results revealed a systematic downward trend in the irradiance at the rate of 0.05 percent per year.

A series of reduced gravity experiments was conducted by JPL scientists using SPAR sounding rockets and KC 135 aircraft in preparation for the flight of a Drop Dynamics Module on the Space Shuttle. These free-drop experiments in zero-gravity environment are expected to have applications in nuclear physics, chemical and material processing, and meteorology.

The reduced gravity tests also contributed to JPL's development of a high-temperature acoustic

containerless processing module being designed for NASA's Material Processing Program. The JPL experiments will be conducted in this module aboard the Space Shuttle.

Significant data on the fluid dynamic behavior of liquid shells was obtained. These experiments confirmed theoretical predictions of oscillation modes and their frequency. The results also are pertinent to the Department of Energy program for developing inertial fusion target shells.



ORIGINAL PAGE IS
OF POOR QUALITY

Results of reduced gravity drop dynamic experiments with JPL's three-axis acoustic levitation module are shown as flown and observed on a SPAR rocket.

IV. Information Systems and
Space Technology
Development

IMAGE PROCESSING USING VERY LARGE SCALE INTEGRATED SYSTEMS

Data systems of the next decade will require extensive improvements in data rates and miniaturization far beyond today's general-purpose digital computers. Vast quantities of image data will have to be calibrated, manipulated and merged at rates far exceeding the capacity of present systems.

Very Large Scale Integrated (VLSI) systems using specific image processing algorithms offer a potent solution. This year JPL built and tested a simulation of a pipeline filter which enhances or smoothes images from 50 to 1000 times faster than present computers.

After commercial multipliers were examined and found wanting, JPL computer scientists incorporated four digital multipliers and accumulators on each chip. As wire sizes continue to shrink with improved industrial fabrication technology, many more multipliers/ accumulators can be expected per chip while using similar designs.

The JPL-designed chips can be connected in tandem as many times as desired to perform a complete convolution or filtering operation during each computer

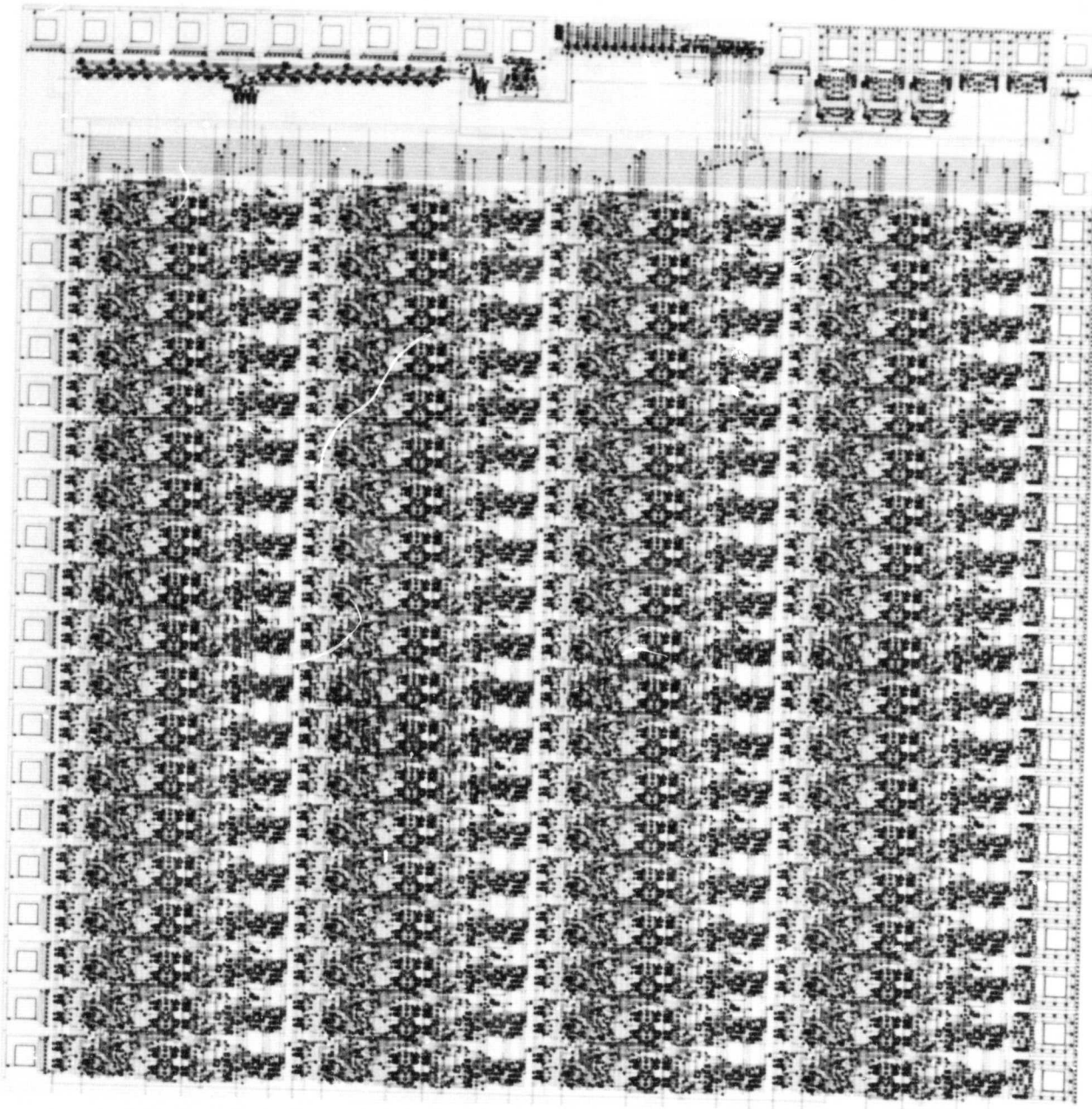
cycle. All multiplications are performed concurrently rather than serially. Additionally, the mathematics have been defined for a simulated VLSI design for a very rapid geometry machine.

The JPL Image Processing Laboratory plans to incorporate the VLSI filter and geometry algorithms into its computer systems in the near future. These two algorithms form the basis for data calibration, registration and mosaicking.

Moreover, VLSI promises to be an inexpensive ancillary to any existing computer system. For example, automated pattern extraction, both commercial and military, has been slow to reach daily applications due to expensive hardware. This device sets the stage for such applications.

Also, seismic exploration for new and better-resolved oil fields requires the greater sophistication that was made possible by faster two-dimensional filtering. For filtering, this device outperforms the Cray-I, considered to be among the world's fastest digital computers.

ORIGINAL PAGE IS
OF POOR QUALITY



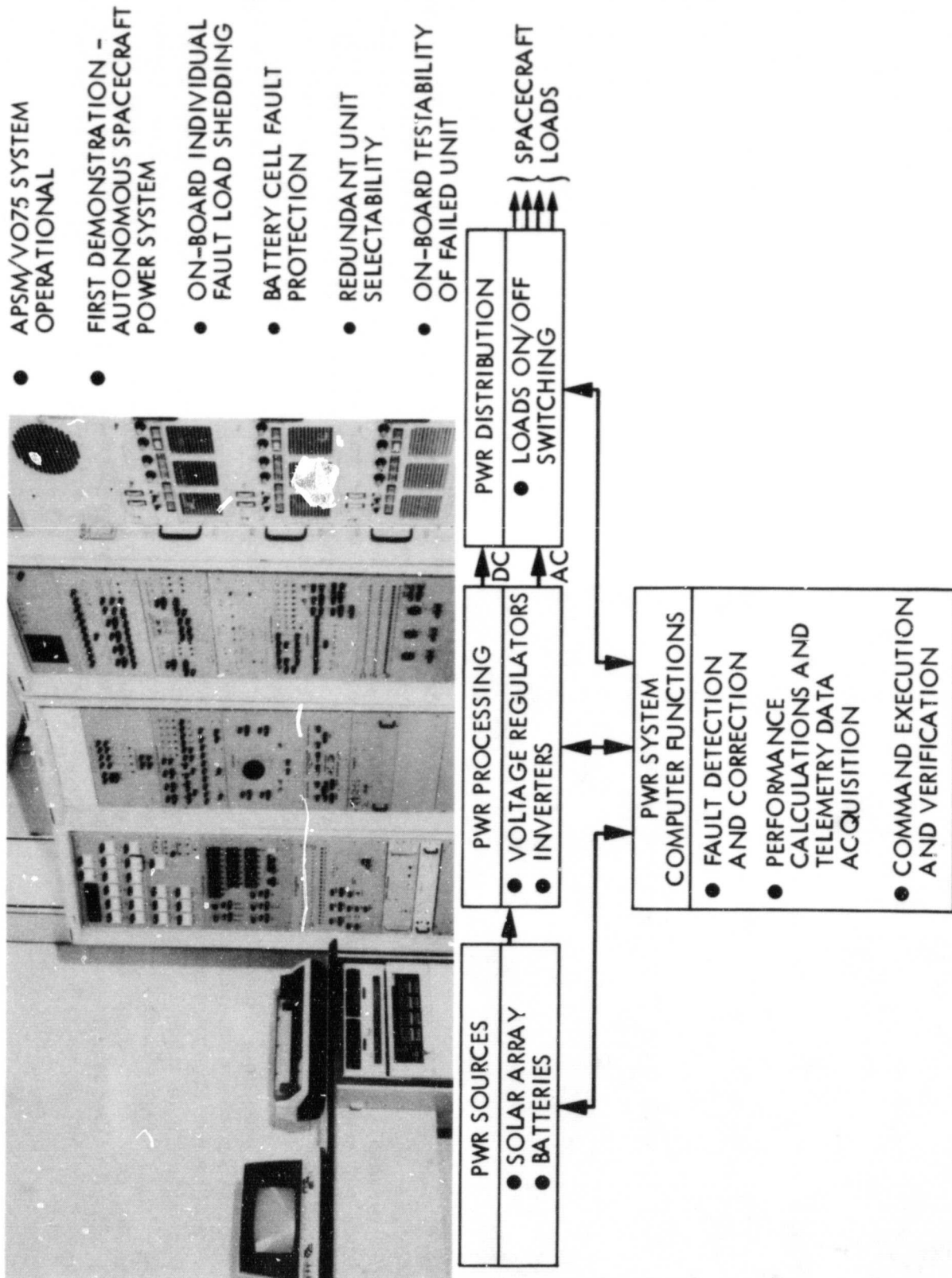
A trial VLSI fabrication of a four-multiply and add chip was made and tested at JPL. Its first major application will be in JPL's Image Processing Laboratory.

An autonomous spacecraft power system for outer planetary missions was developed and demonstrated by an advanced technology task group. The system incorporated Automated Power Systems Management (APSM) functions for monitoring, computation, and control on board the spacecraft, minimizing need for Earth-based control.

The APSM demonstration used a Viking Orbiter breadboard power system and a distributed microcomputer to implement autonomous functions. Key APSM functions include battery charge control; power processor monitoring, fault detection, and redundant element switching; data acquisition, processing, and storage; power margin management; and individual load fault detection and recovery.

The APSM capability is designed for missions in which round-trip light time (greater than one hour) is too long for effective ground-based response to spacecraft problems.

The system provides new flexibility. Design changes affecting monitoring or computing functions can be made in software rather than hardware, as at present. Such modifications, including changes in the telemetry data format, can also be made in flight.

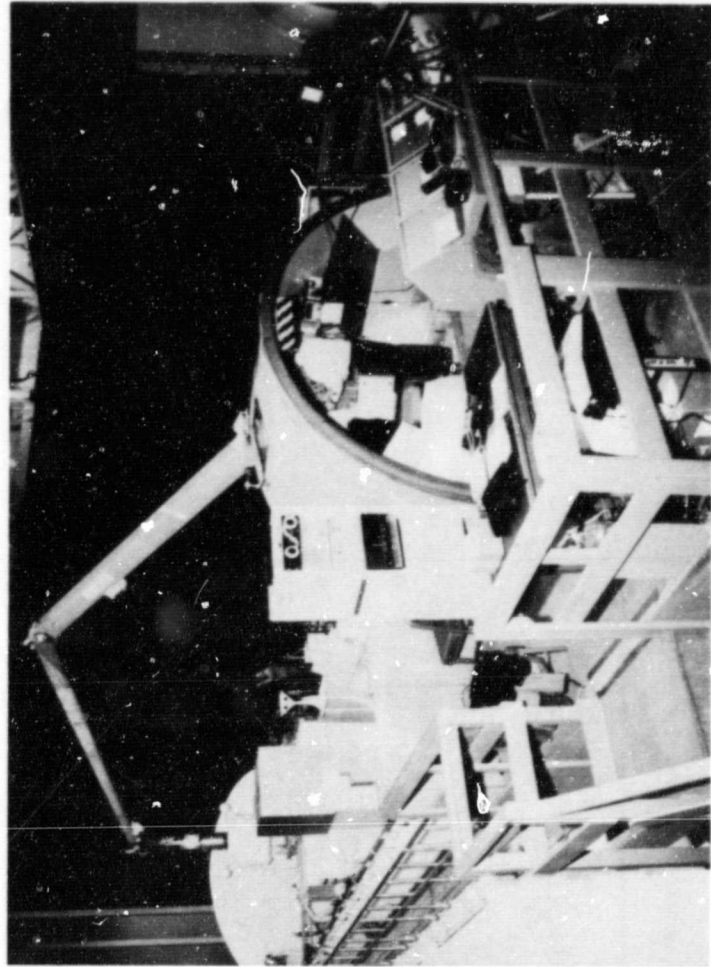


A voice control system for control of the Space Shuttle cameras and monitors has been developed and successfully tested by the JPL Teleoperator Laboratory at the Remote Manipulator Development Facility of the Johnson Space Center in Houston, Texas.

The Remote Manipulator System (RMS) is a mechanical arm fifty feet in length mounted in the cargo bay of the Space Shuttle. It will be used to deploy and retrieve satellites and other payloads into and out of Earth orbit. Control of the RMS arm requires the use of both of the operator's hands. There are several TV cameras located in the cargo bay and two TV monitors in the control cabin that allow the

operator to get a close-up view of the payload being operated upon. Prior to implementation of the JPL voice control system, in order to control the selection and movement of the cameras (PAN, TILT, IRIS, FOCUS, ZOOM, etc.), the operator must cease control of the RMS arm, press some buttons and toggle switches on the camera control panel until the cameras are aligned properly, and then resume control of the RMS arm.

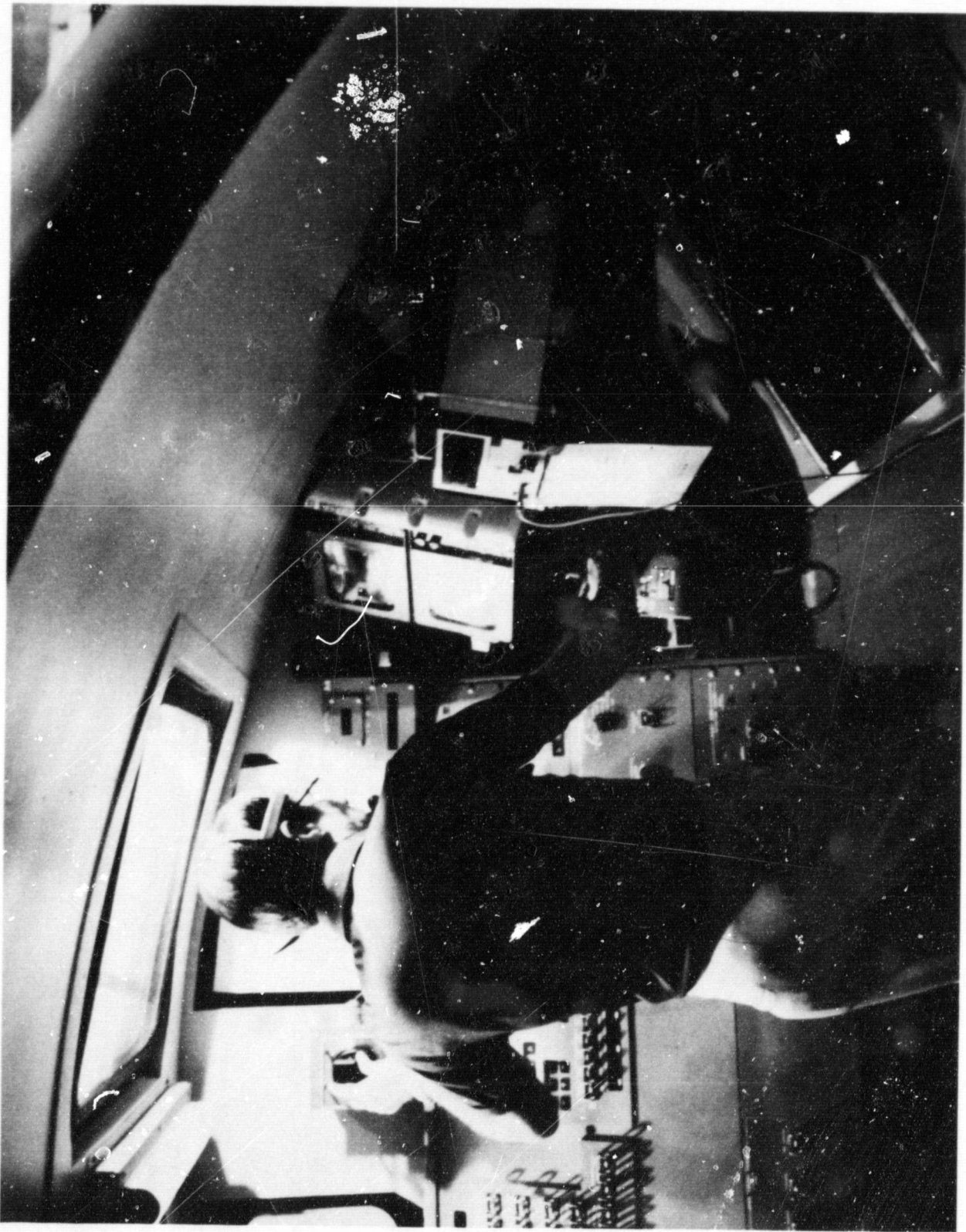
The JPL voice control system allows the operator to "speak" to the camera control panel and control the selection and movement of the TV cameras while simultaneously retaining control of the manipulator arm.



**ORIGINAL PAGE IS
OF POOR QUALITY**

Overall view of the Space Shuttle cargo bay and control cabin simulator at the RMS Manipulator Development Facility of the Johnson Space Center in Houston, Texas. The voice control system and camera control panel are located in the control cabin (aft end of the Space Shuttle cockpit).

ORIGINAL PAGE IS
OF POOR QUALITY



An operator inside the control cabin simultaneously operating the RMS manipulator arm and controlling the cameras and monitors by voice.

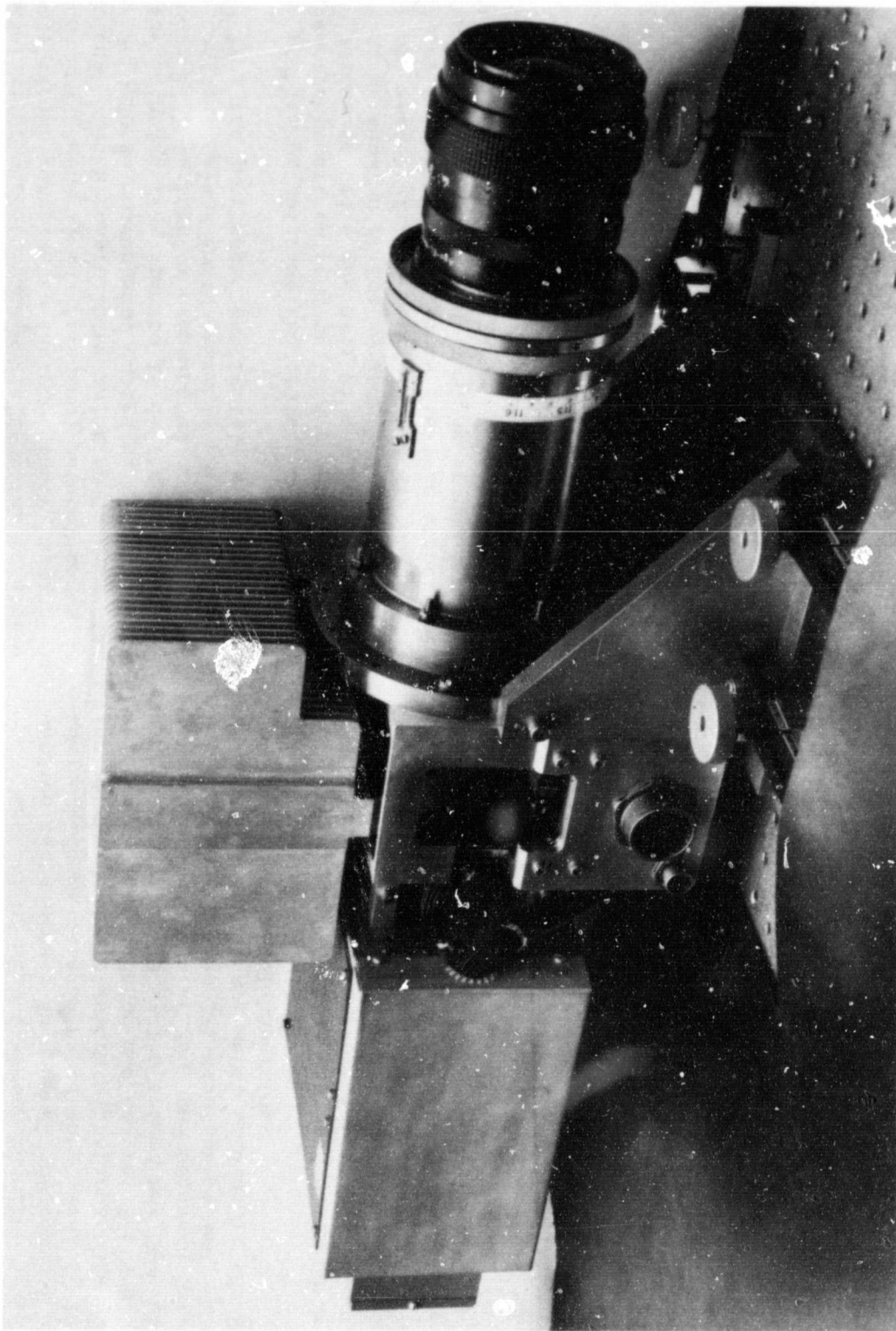
The control of spacecraft attitude and science instrument-pointing has traditionally been an Earth-based function. As spacecraft probe deeper into the cosmos, farther from Earth, the long communication delays adversely affect control precision. Vital communication channels must be diverted from science data acquisition -- a problem common to all missions including Earth orbiters. To alleviate these problems, JPL developed the Target Body Tracker (TBT) for onboard, autonomous image processing. The prototype of this system became operational in 1981.

The Target Body Tracker consists of a solid-state, charge-coupled device (CCD) camera coupled to a microcomputer for large area imaging. Its function is to determine precise position of objects within and relative to its field of view, including acquisition and tracking of stars, planets, satellites, asteroids, comets, and other spacecraft. The

TBT also can aid in imaging science instrument calibration and perform limited target recognition functions. The most vital of these is target acquisition, allowing the science instrument-pointing control system to correct for errors in navigation, predicted target position, and spacecraft attitude.

Laboratory testing of the tracker prototype produced accuracies on the order of 1/18,000 degree for high-rate tracking of extended targets. The current prototype was designed for first flight application on the proposed Halley Intercept Mission; Earth-orbital satellites, terrestrial and outer planet survey craft, interstellar probes, and even robot landers could employ the tracker. On Earth, unmanned probes for deep ocean exploration and data acquisition in hazardous areas such as Mt. St. Helens might be guided by TBT-control systems.

ORIGINAL PAGE IS
OF POOR QUALITY



The Target Body Tracker prototype shown here in breadboard array underwent JPL testing. Results yielded accuracies needed for future spacecraft control.

Mass limitations of space vehicles often require the vehicle's configuration to include highly flexible components having several low-frequency natural modes of vibration. When high-precision pointing instruments are mounted to these components, designing a controller to meet the pointing requirements is difficult. Design of the controller is further complicated when the actuator for controlling the instruments is physically separated from the instrument by flexible structure.

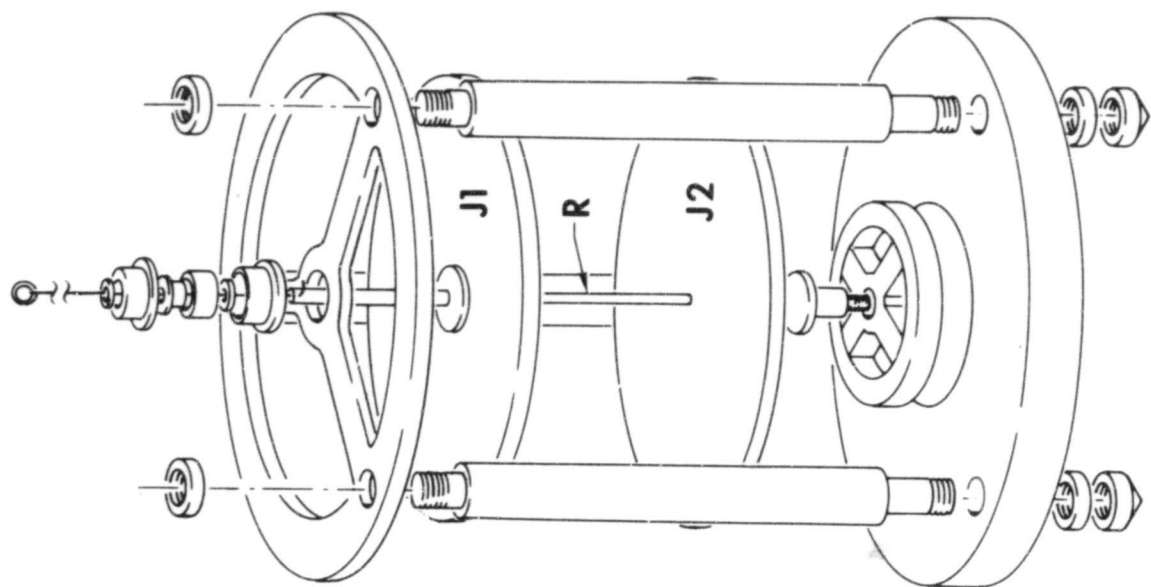
The problem of pointing the television cameras on the Galileo spacecraft epitomizes this severe control problem. Torque to drive one axis of the Galileo cameras must be applied at the de-spin bearing at the center of the spacecraft, but the cameras are mounted at the end of a long series of very flexible structural members through which the torque must be transmitted. The assemblage has five or six modes of vibration, lightly damped, and some at low frequency (1 or 2 hertz). The upper section of the spacecraft, with its long, flexible booms, will be rotating slowly, and will thus invoke vibratory inputs at many low frequencies. The only sensors useful for control will be gyros on the camera package, far removed, structurally, from the applied torque. While high-quality gyros will be used, their signals (and any noise therein) will be magnified many-fold by the sort of predictive compensation that the controller will need to stabilize the system.

Control of such a system requires new and as yet untried techniques. An unusual new control scheme, tuned-feedback damping based on phase-lock-loop tracking of the dominant system vibrations, has been developed by the Guidance and Control Section's controls team at JPL. The scheme has been analyzed by computer simulation at JPL, and Stanford University has complemented the JPL development program with theoretical and experimental studies in the Stanford Guidance and Control Laboratory.

A torsional system has been designed by Stanford and built to study control of flexible structures. A brushless DC motor exerts torque upon the lower disk J2. A position sensor measures the angular position of the upper disk J1. J1 and J2 are connected by a one-eighth-inch diameter steel rod R. The rod is very compliant and acts as a torsion member. The complete laboratory experiment consists of a digital computer, a voltage controlled current amplifier, the above described torsional system, and various computer interfaces. This system serves as a testbed for the development and testing of control laws for flexible systems.

Both experimental testing at Stanford and computer simulation analysis at JPL have demonstrated the effectiveness of the tuned-feedback damping concept for a complex spacecraft.

ORIGINAL PAGE IS
OF POOR QUALITY



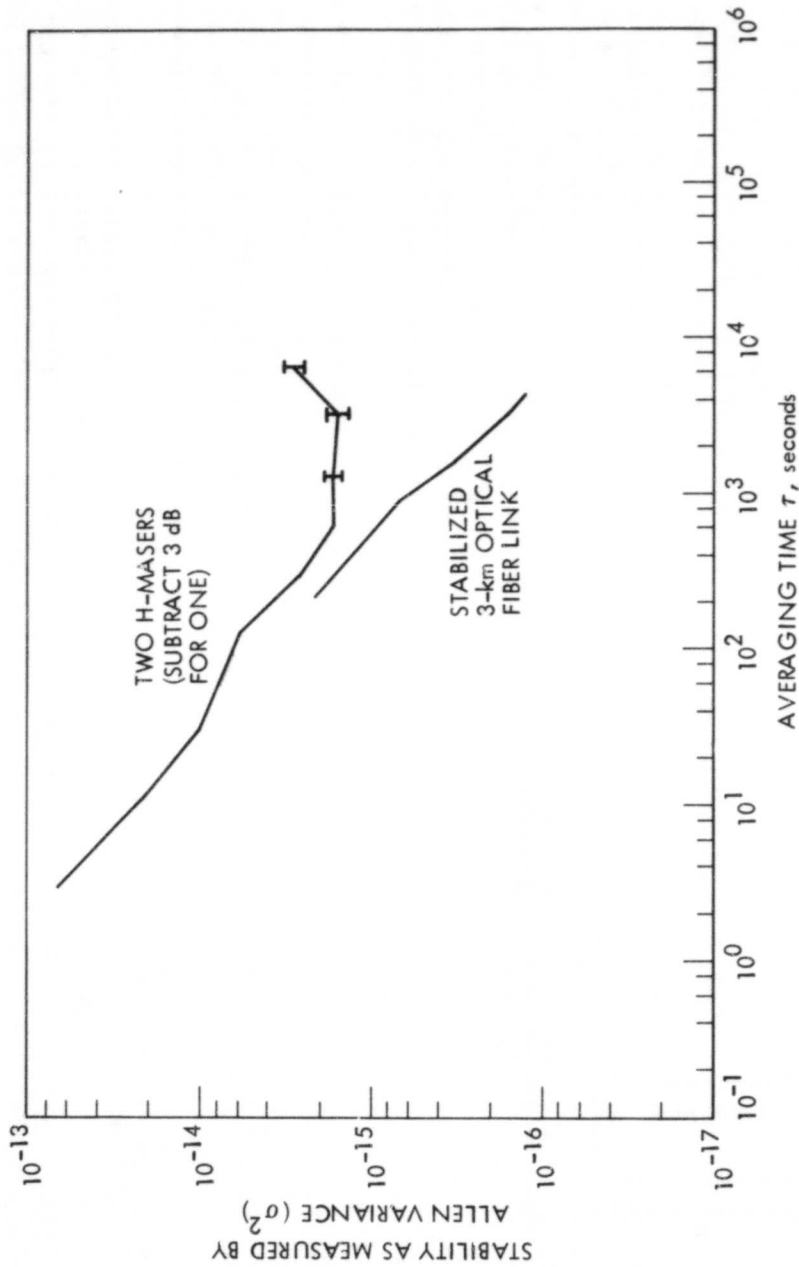
Hardware for non-colocated sensors and actuators experiment.

Optical fiber systems are being developed at JPL to distribute ultra-precise reference frequency signals throughout a Deep Space Communications Complex (DSCC). These ultra-stable signals (10^{-15} stability for averaging times of 100 seconds) are generated by complex and costly frequency standards such as hydrogen masers. The expense of having a frequency standard at each station in a Deep Space Network complex can be alleviated by distributing the reference signal from a centrally located standard to all of the stations in the complex. Optical fibers could be the most suitable medium for distributing these signals, once fully developed for communications. Their stability as a medium for distributing frequency and time had been

unknown until JPL experiments this year.

An experimental optical fiber distribution system 3 kilometers long has been stabilized and achieved a stability of 4×10^{-15} for an averaging time of 100 seconds. It was necessary to develop special test methods and hardware in order to make measurements with the required precision. The stability of this system was found to be limited by the optical transmitter and receiver and not by the optical cable or stabilizing system. A stability of 10^{-17} will be needed to conduct gravity wave experiments, but the demonstrated stability is adequate for all of the current radio science or radio navigation data types.

ORIGINAL PAGE IS
OF POOR QUALITY



The rms fractional frequency deviation (stability) of the 3-km optical fiber link plotted with the relative stability of two hydrogen maser frequency standards for comparison.

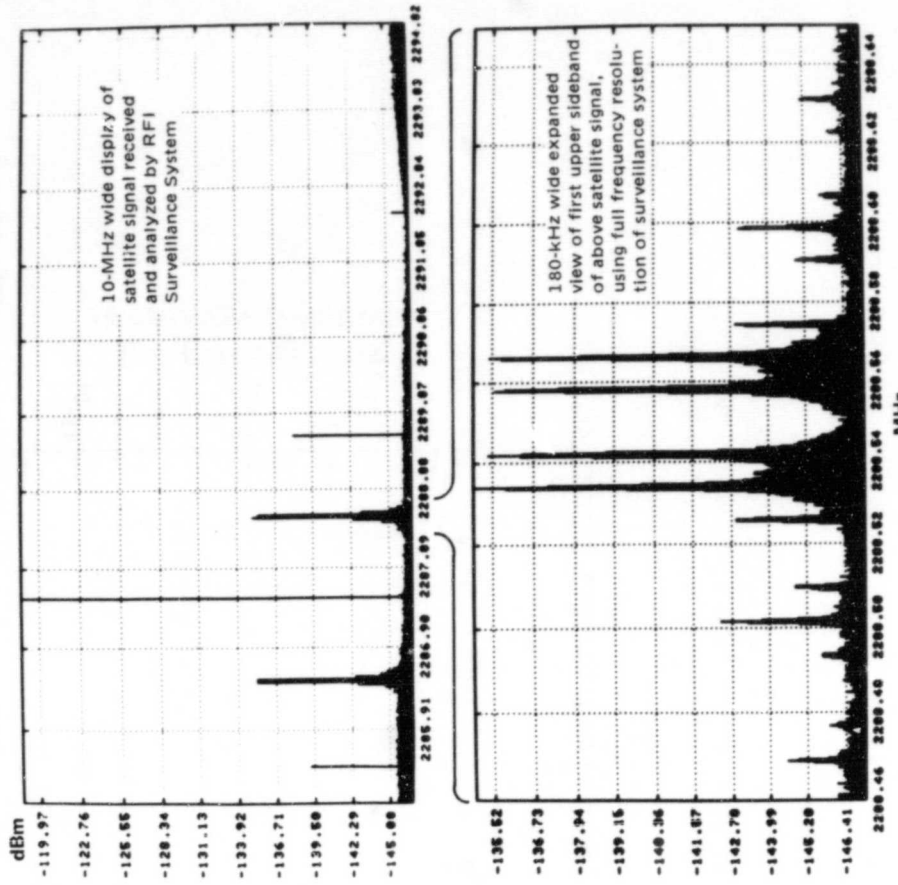
As competition for the available radio spectrum increases, the Deep Space Network (DSN) is becoming ever more concerned about disruptions in station operations caused by radio frequency interference (RFI). Deep space communication links are particularly vulnerable to RFI due to the extraordinary sensitivity of DSN receivers and antennas, which are required to detect extremely weak signals.

Frequency coordination arrangements between the DSN and other radio spectrum users help to reduce the quantity of RFI. These require real-time RFI data, such as the direction, spectra, and time of the interference to identify the source of the RFI, be they civilian satellites, aircraft, or others.

The DSN developed an experimental RFI surveillance system to monitor the S-band environment at the Goldstone DSN complex. A key element of the system is a digital Fast Fourier Transform (FFT) spectrum analyzer, which generates two 32K-line spectra, each covering a 10-megahertz bandwidth. Each 10-MHz bandwidth can be tuned independently in the 300-MHz bandwidth between 2150 to 2450 MHz. The system does 600 million multiplications per second, far beyond the capabilities of commercially available units. A general-purpose digital computer is used to provide flexibility in controlling surveillance operations, reduce the data to a manageable format, and enable real-time source identification capability.

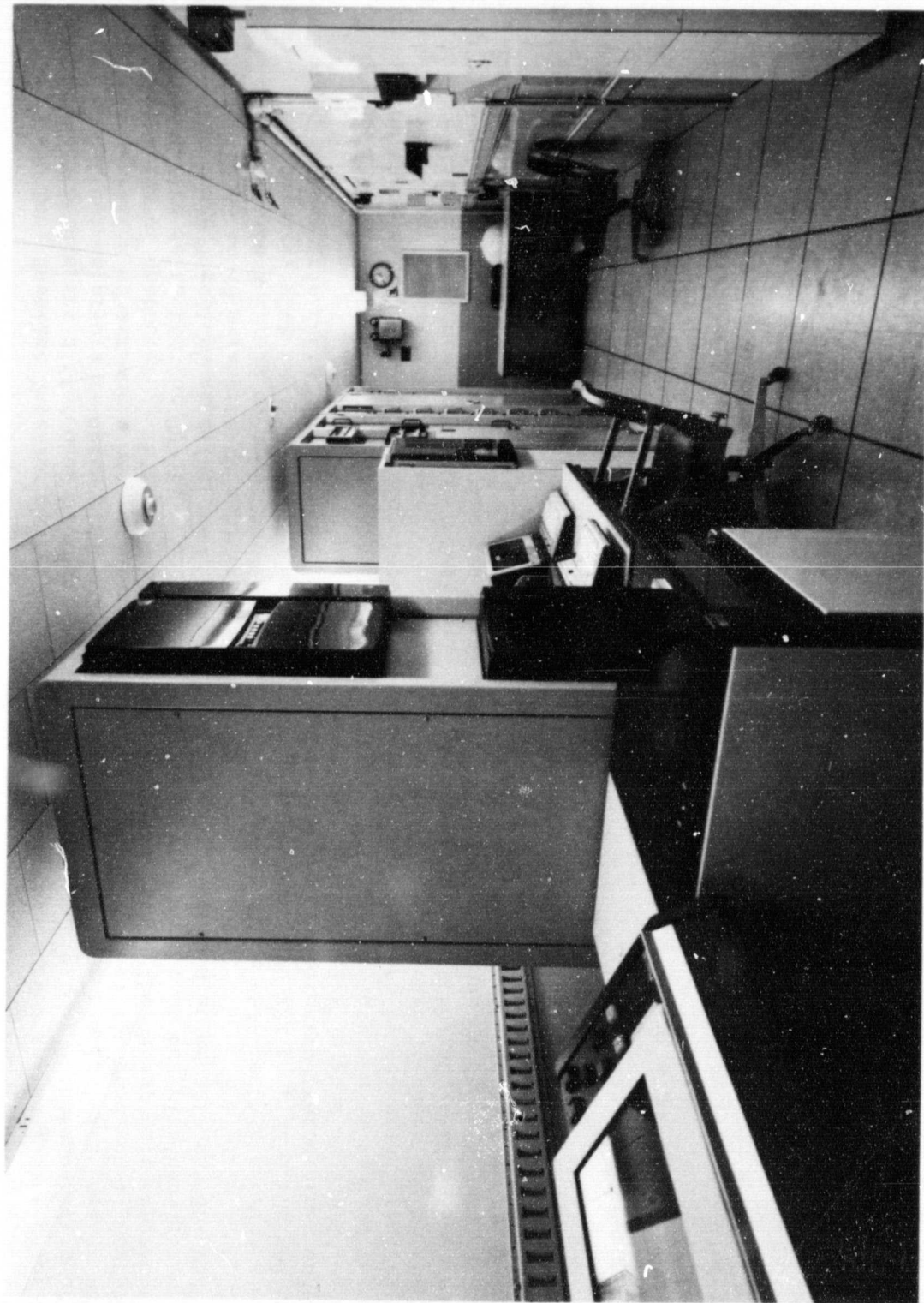
The RF surveillance system is able to detect signals at -170 dBm in a 300-Hz resolution bandwidth, and also detect a 2.4-microwatt isotropically transmitted carrier at a range of 160 kilometers. Two spectra are shown in the first figure, one wideband and one narrower band.

The 20-MHz S-band system was installed in a trailer and deployed on a hilltop at the Goldstone DSN complex near Barstow, California in February 1981, where it has been gathering data. Design for an expansion of this surveillance capability to a bandwidth of 80 MHz and 256K resolution lines at both S- and X-band has been initiated.



Satellite spectrum.

ORIGINAL PAGE IS
OF POOR QUALITY



Interior view of the Radio Frequency Interference Surveillance System trailer.

A method of Very Long Baseline Interferometry (VLBI) in which observations are differenced between two sources to cancel common errors -- delta VLBI -- was used in a demonstration of extremely high-accuracy quasar-based navigation of spacecraft. This technique, frequently called delta DOR for "delta differenced one-way range," employs an effective received bandwidth of up to 40 megahertz to achieve spacecraft angular position accuracy of about 50 nanoradians. (That compares with the 250- to 750-nanorad accuracy of other radio metric techniques.)

Delta DOR has the further advantages of full sensitivity at low spacecraft declinations and shorter tracking requirements than conventional Doppler tracking. It may ultimately reduce antenna use for tracking by 90 percent during spacecraft cruise and 50 percent during planetary encounters.

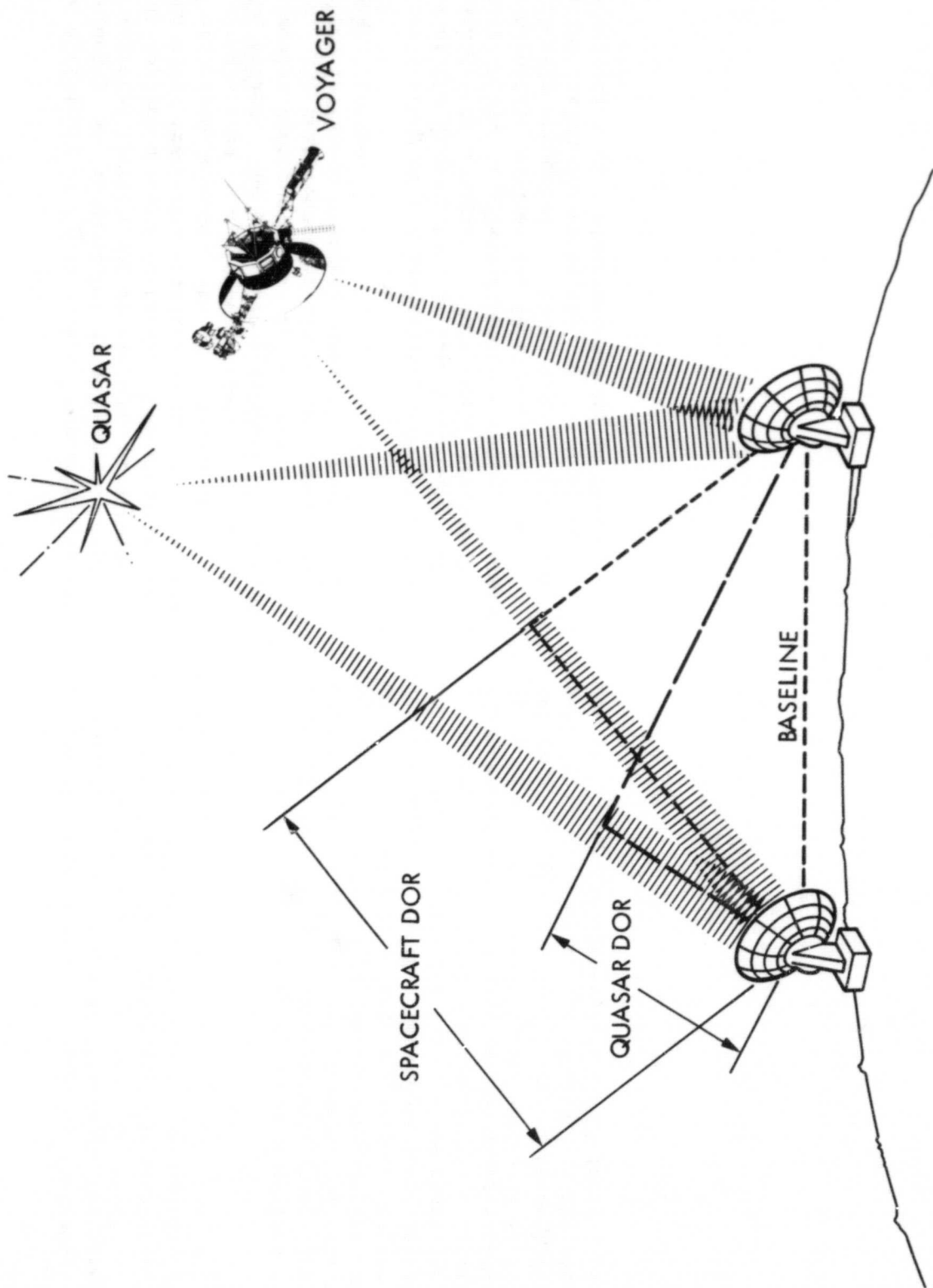
Recent delta DOR demonstrations have been of two types: one using a Voyager spacecraft and an angularly nearby quasar, and one using only quasar pairs. Because the Voyager signal for delta DOR is at S-band and has a relatively limited bandwidth of 3.6 MHz, the goal for that portion of the demonstration is position accuracy (in the quasar frame) of 150 nrad. In the past two years approximately 60 Voyager

delta DOR observations were made, most using 64-meter DSN antenna pairs (either Goldstone-Madrid or Goldstone-Canberra). The results with Voyager have shown a consistency of 70 to 130 nrad, easily surpassing the 150-nrad goal. The quasar pair experiments, also conducted at S-band but with bandwidths up to 36 MHz, produced results at or near the 50-nrad level.

A variant delta VLBI technique using a single narrow bandwidth (250 kHz to 2 MHz) channel measures spacecraft angular velocity (rather than angular position) to accuracies as good as 5 prad/s (5×10^{-12} rad/s). This sensitivity can be applied to navigating low planetary orbiters by measuring precisely the orientation of the orbit in the plane of the sky. To demonstrate the technique, observations will be made of Pioneer 12, now orbiting Venus. If it performs as expected, the narrowband delta VLBI cross-velocity technique will be used for the high-accuracy orbit determination crucial to future radar mapping of Venus.

The delta DOR demonstration is continuing with observations of the Voyagers and quasar pairs. Results will be analyzed to determine the final system configuration and data-taking protocols for the delta DOR navigation of Galileo.

ORIGINAL PAGE IS
OF POOR QUALITY



Δ DOR observing geometry. The interferometer first measures the differential one-way (DOR) to the spacecraft and then to the quasar. The DORs are differenced (Δ DOR) to cancel common errors and give a precise position of the spacecraft with respect to the quasar.

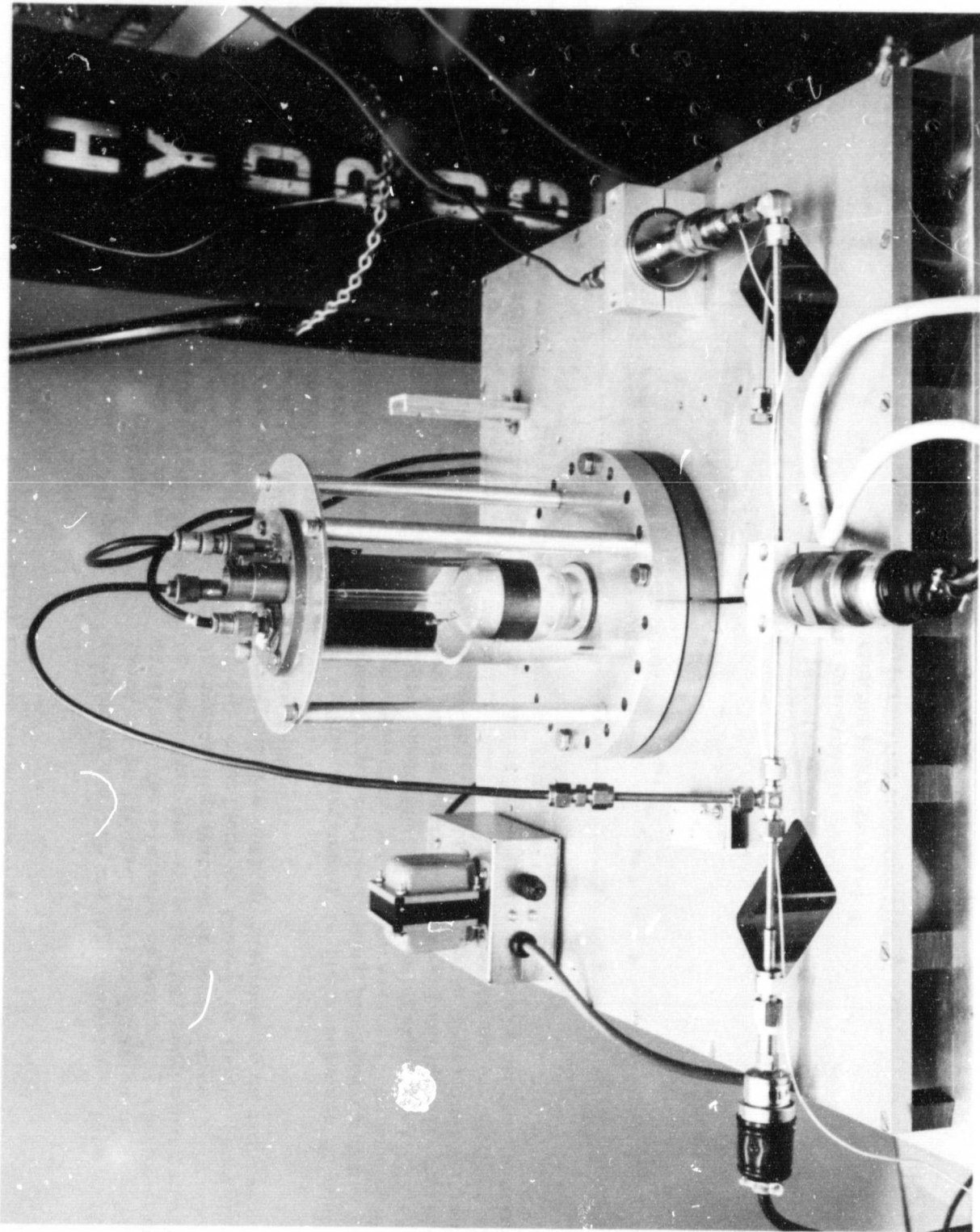
The efficiency of hydrogen atom production in the radio frequency (RF) dissociator of a hydrogen maser has been improved through the development of a technique that applies a magnetic field. The operation of a hydrogen maser frequency standard is based on the excitation of a spin-selected beam of hydrogen atoms that become confined in a microwave cavity to undergo the masing action. The atoms are generated in a source where molecular hydrogen gas is dissociated in an RF discharge. The performance of the RF discharge dissociator can influence hydrogen maser performance and operational lifetime.

After a study of the processes occurring in the RF plasma of the dissociator, it was determined that the application of a magnetic field could enhance the source efficiency. A solenoid was constructed to apply an axial magnetic field on the RF plasma, and the results clearly supported the model study. Since the dissociation action occurs by the collision of the hydrogen molecules with electrons moving in response

to the RF field, the axial magnetic field can enhance the dissociation action by increasing the path length of the electrons in the plasma. By spiraling along the field lines, the electrons have more opportunity to undergo collisions with molecules and cause dissociation.

Tests indicate that an axially applied magnetic field of about 80 gauss increases dissociation efficiency of the RF source by a factor of two, when the RF source operates under power and gas pressure conditions employed in working masers. Furthermore, using a magnetic field allows a decrease in either applied power or gas pressure. A decrease in power increases the life of the dissociator; a decrease in pressure enhances the life of the maser vacuum pumps. It is now possible to apply the magnetic field and arrive at a judicious design choice through proper selection of the operating RF power of the source, gas pressure, and dissociation efficiency.

ORIGINAL PAGE IS
OF POOR QUALITY



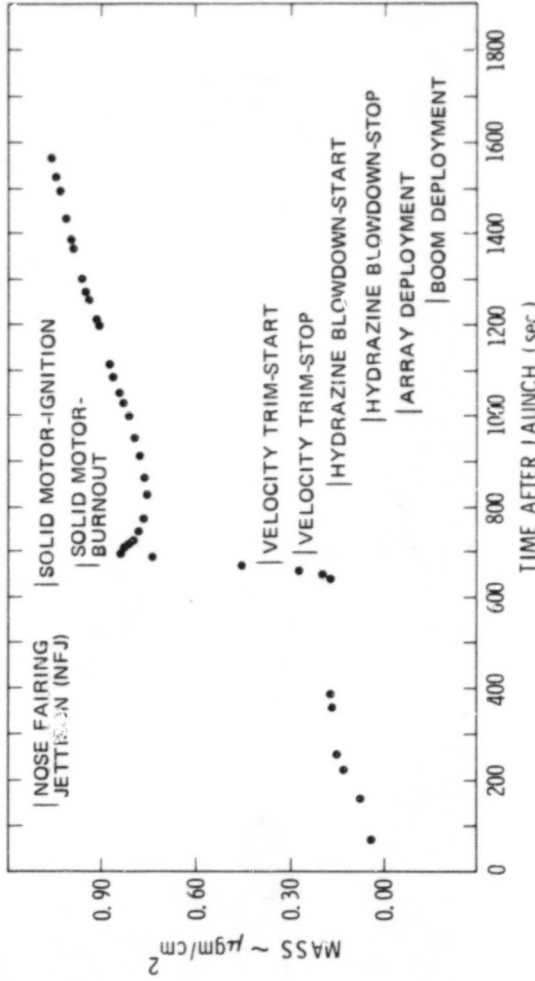
The RF dissociation and solenoid pictured in JPL laboratory.

A spacecraft contamination monitor was developed for flight on the National Oceanic and Atmospheric Administration (NOAA-7) environmental service satellite launched June 23, 1981. The instrument, designed and built by JPL with funding from the Air Force Rocket Propulsion Laboratory, measured contamination induced by the Apogee Kick Motor (AKM) firing. The AKM had been suspected of causing degradation of Tiros-N and NOAA-A hydrazine thermal control systems. The JPL instrumentation includes two thermoelectric quartz crystal microbalances (TQCM), four calorimeters, and a filtered UV detector.

Preliminary data indicate that significant amounts of contamination from the spent AKM, reflected from the back of the solar array after deployment, cause the thermal degradation. Additional data indicate that contamination is deposited in the backflow

region of the AKM during operation. Data will continue to be reduced for the duration of the NOAA-7 mission. The ultimate objective of the experiment is to determine the effects that contamination will have on system degradation or performance. The location of the experiment on NOAA-7 is in the general area of two sensitive optical instruments on follow-on NOAA spacecraft.

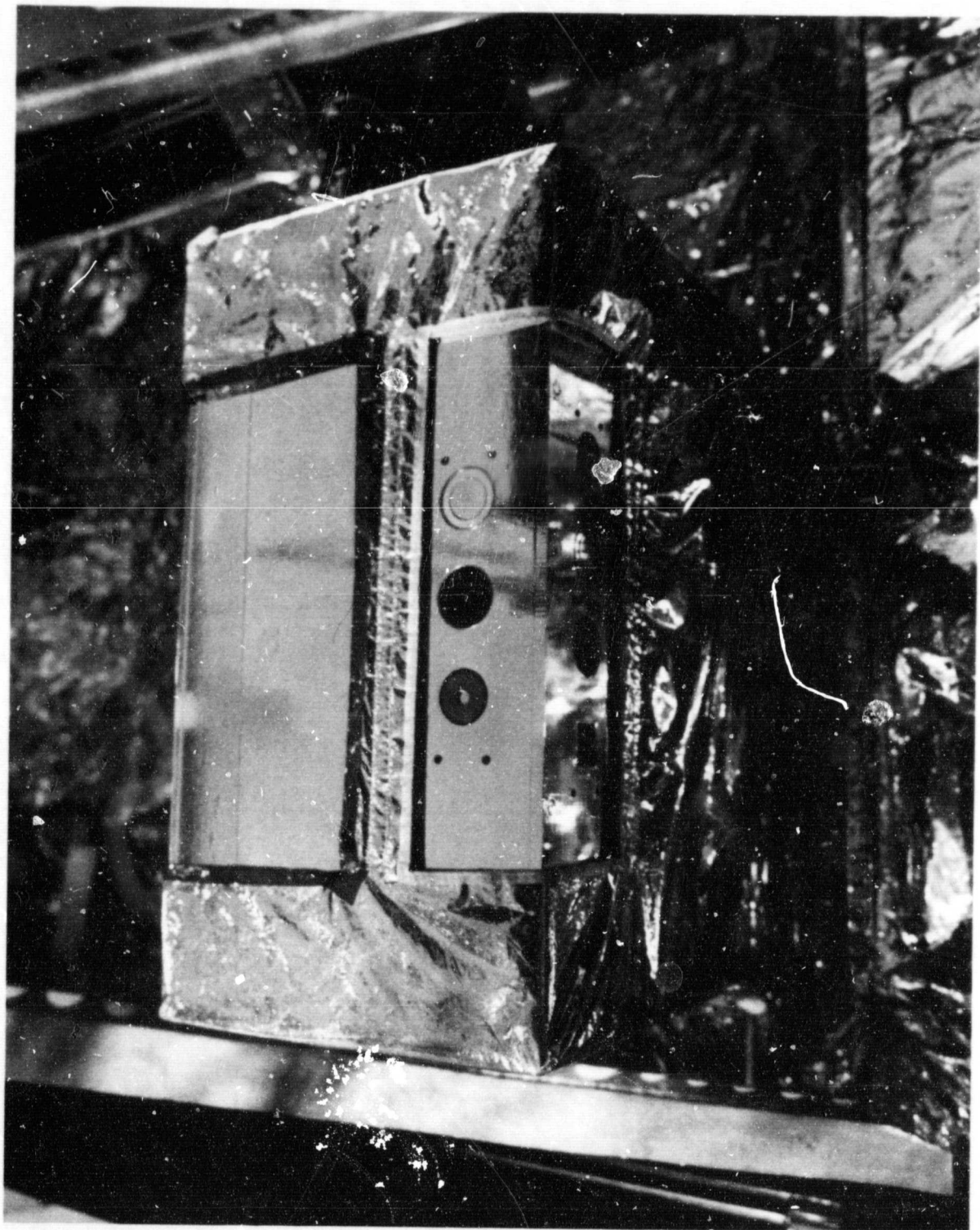
This instrument is the forerunner of additional operational monitors being produced by JPL. The OSS-1 Contamination Monitor Package will be launched on the third Space Shuttle orbital flight test (OFT-3) to monitor contamination levels during all shuttle flight operations. Additionally, a contamination monitor is being developed for a Department of the Navy satellite to measure contamination levels of the onboard attitude control system.



ORIGINAL PAGE IS
OF POOR QUALITY

TQCM sensor 1 mass deposition.

ORIGINAL PAGE IS
OF POOR QUALITY



JPL contamination monitor emplaced on the NOAA-7 environmental service module. On top is a TQCM and two calorimeters. On the side face are a TQCM, two calorimeters and a filtered UV detector. Contamination was detected by the firing of two cable cutters at the base of the instrument.

The testing of solid-propellant burning rates recently was extended at JPL to pressures of 7000 atmospheres, or about 100,000 pounds per square inch. Previous JPL tests had characterized propellant burning surface effects up to pressures of only 500 atmospheres (7000 psi).

Earlier analytical studies had demonstrated that the high-pressure combustion of rocket solid propellants is correlated with the nature of the propellant burning surface.

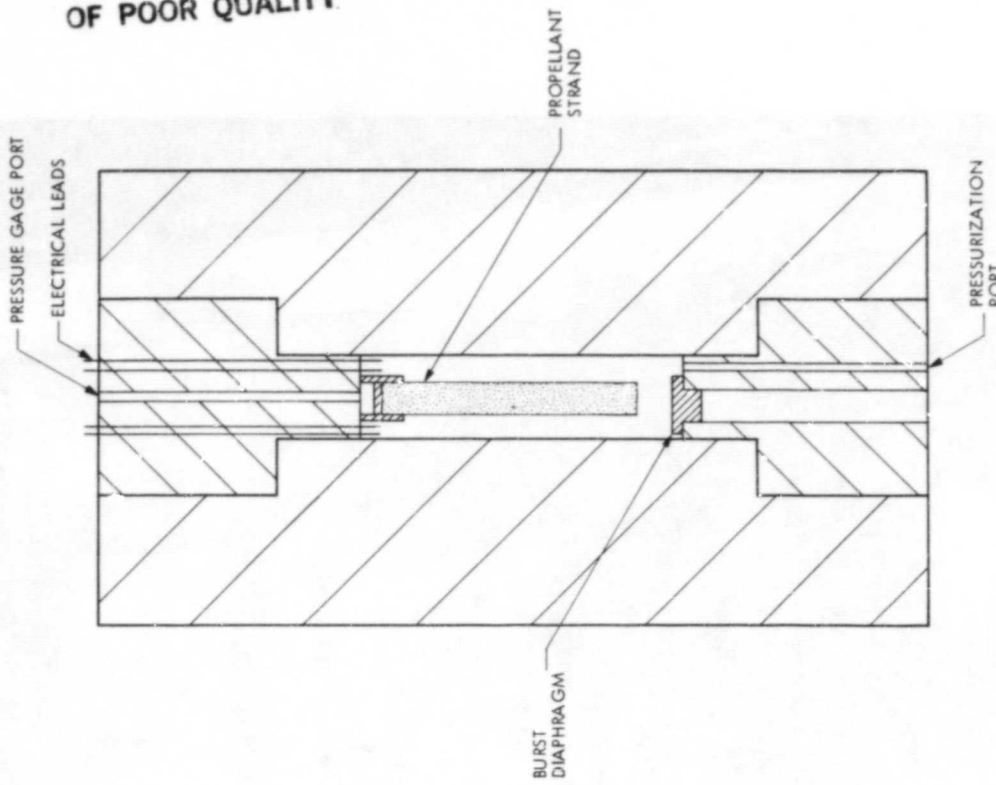
A high-pressure closed vessel was developed to study the combustion of rocket solid propellants over the pressure range of 0.7-7 kbars (10,000-100,000 psi). The vessel's upper closure contains electrical leads, a port for a pressure gage, and a support to keep the propellant sample in an inverted position. The lower closure contains a pressurization port and the burst diaphragm. Diaphragms are designed to rupture at desired pressures. The side surface of the cylindrical propellant strand is coated with a burning inhibitor, so that when the lower end is ignited, the strand burns upward in cigarette fashion.

The test procedure consists of pressurizing the vessel with nitrogen to 320 atmospheres (4700 psi). When the strand is ignited, combustion gases generated in the chamber raise the pressure until the burst diaphragm fails.

The experiment produced two types of data: (1) burning rates were continuously measured by the rate of change in electrical resistance of a circuit formed by electrical leads attached to the sides of the propellant strand and the ionized flame, and (2) the extinguished surface of the propellant was studied under a scanning electron microscope to show the surface

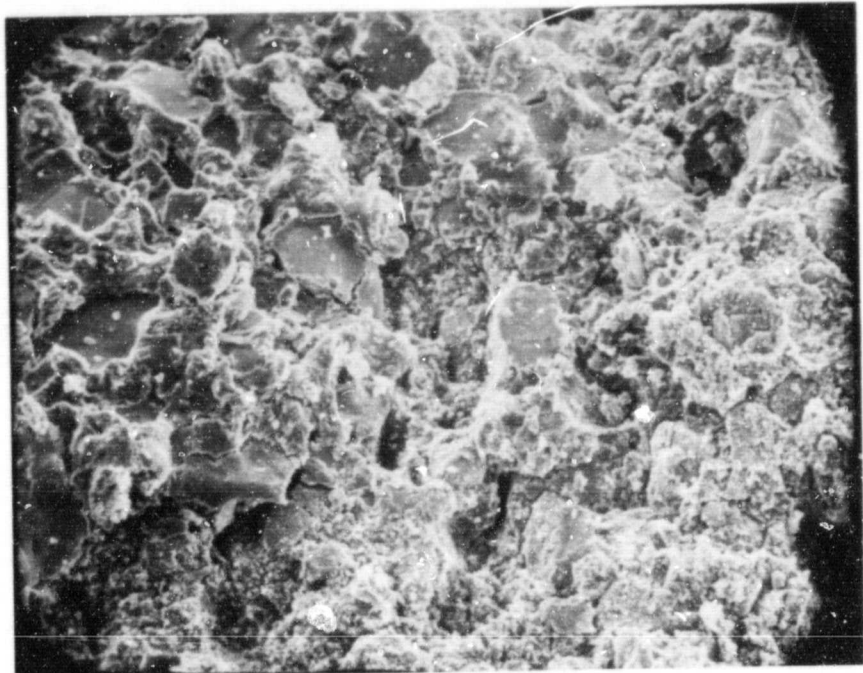
structure that existed at the diaphragm rupture pressure.

ORIGINAL PAGE IS
OF POOR QUALITY

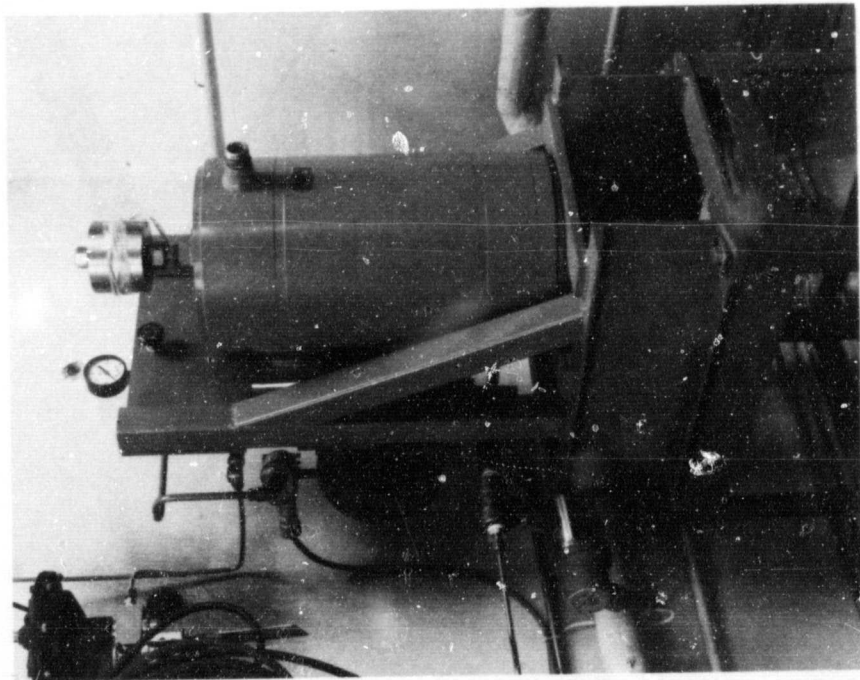


Schematic diagram of a high-pressure closed combustion chamber used for the study of the transition of solid-propellant burning from deflagrative to detonative mode.

ORIGINAL PAGE IS
OF POOR QUALITY



SEM photograph of an extinguished propellant surface, quenched at a pressure of 0.7 kbar (10,000 psi). At this pressure, the burning surface, magnified 100 times, was highly cratered.

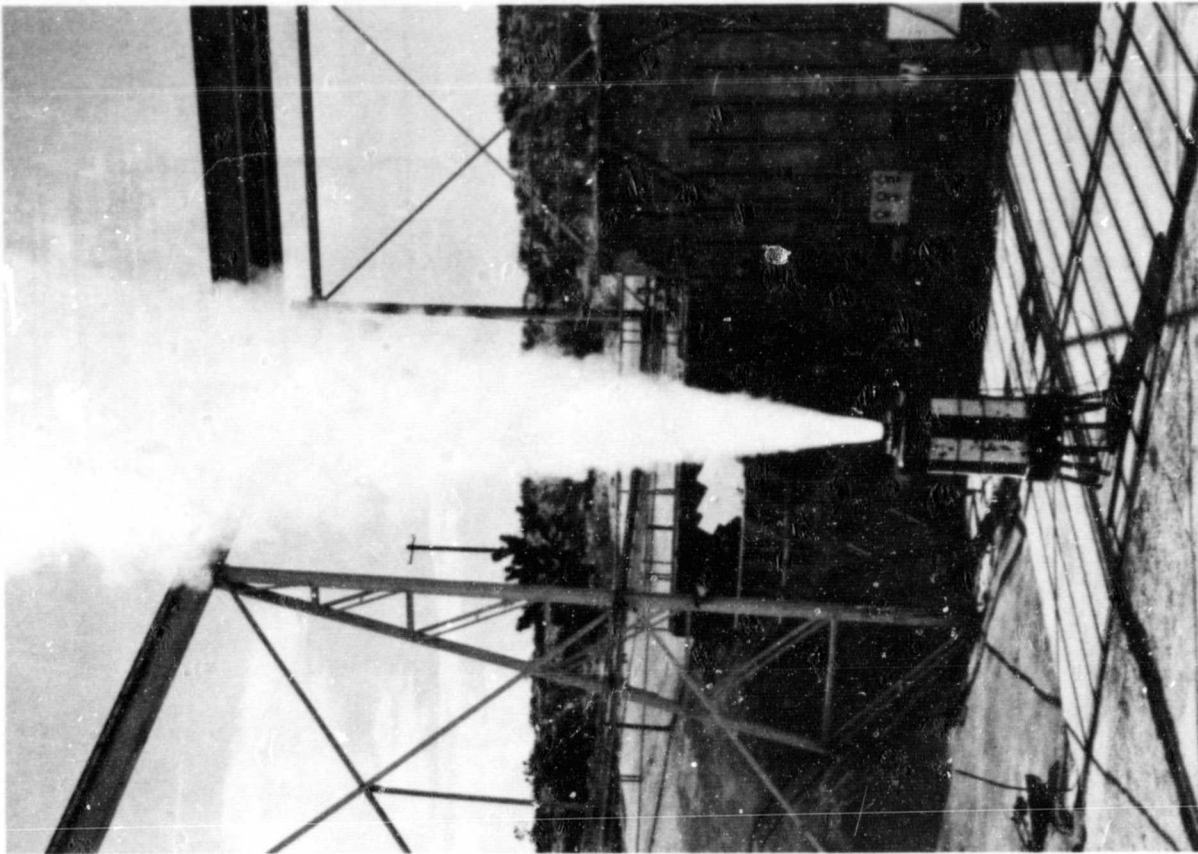


View of completed high-pressure closed combustion chamber that is capable of conducting combustion tests over a range from 700 to 7000 atmospheric pressure.

Development of a solid rocket motor able to withstand the rigors of thermal sterilization has been attained by JPL engineers after several years of effort. This followed the NASA requirement that any future spacecraft designed to land on a planet must be biologically sterile.

The goal, successfully met, was to produce a propellant system that would fire properly after withstanding seven heat cycles of 54 hours each at a temperature of 135°C (275°F). The technology was demonstrated by test firings of two solid rocket motors -- a 32-kilogram (70-pound) motor and a larger one of 272-kg (600-lb) propellant weight.

The larger motor was subjected to seven cycles of 80 hours each at 135°C to allow for heat-up time of the large mass in order to maintain a uniform 135 degrees throughout the 54-hour period. The propellant comprises 84 percent solids and 16 percent aluminum hydroxy terminated polybutene (HTPB).



The 272-kg motor is shown in its successful test firing in February 1981. It ran as predicted for 31 seconds at an average chamber pressure of 345 newtons per square centimeter (500 psia).

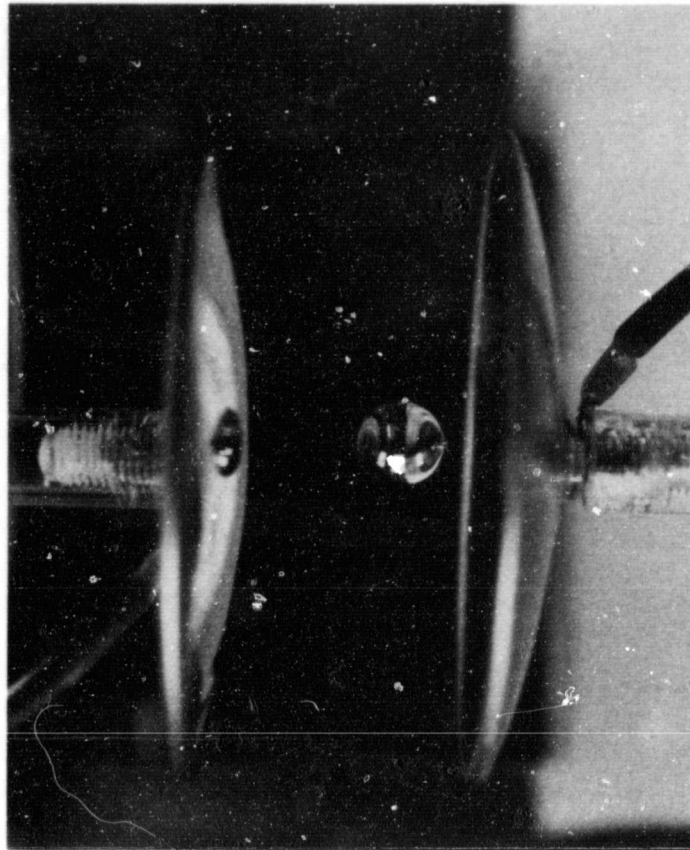
The containerless science group at JPL has developed an electrostatic levitator which levitates and manipulates large objects using a feedback-controlled electrostatic force. This new system can be operated in a very high vacuum chamber, so that one can achieve truly contactless materials processing in Space Shuttle laboratories.

The electrostatic containerless process team succeeded in levitating several large objects with a levitator designed for ground-based operation. The electrodes in this levitator are shaped so that charged objects always experience a centering force toward the vertical symmetry axis when proper voltages are applied.

Levitating and positioning along the vertical axis is achieved by an active feedback control system. A CCD camera monitors the object's position, and a minicomputer processes the information in real time, providing an error signal which takes into account the position error from a set position, as well as the velocity damping of the object. The error signal is fed into a high-voltage unit, which generates the electrostatic force between the electrodes.

The present levitator (the $g = 1$ model) will provide physical parameters of the system crucial to the design of a reduced gravity model.

ORIGINAL PAGE IS
OF POOR QUALITY



The JPL electrostatic levitator (model $g=1$) is shown stably levitating a glass balloon in a laboratory test.

Infrared imaging offers the possibility of detecting and discriminating the constituents of planetary atmospheres and mapping the location of geologic structures. Such imaging is of great interest for both planetary and Earth resource missions.

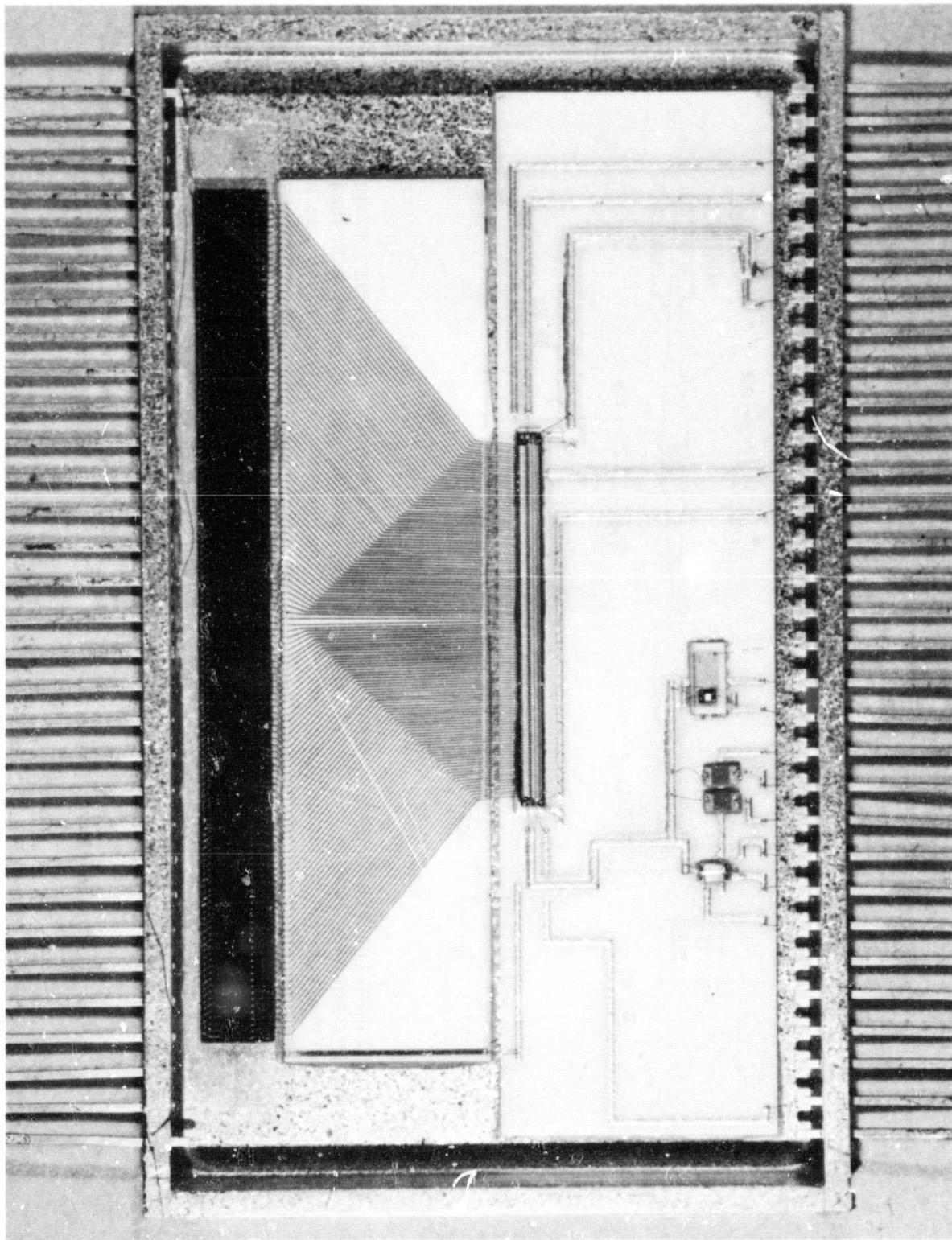
Development of solid-state infrared detector arrays may provide this new capability for future planetary and terrestrial missions. The design and development of the focal plane array for the Galileo Near Infrared Mapping Spectrometer revealed that extremely high performance could be obtained by using indium antimonide photodiodes.

Subsequent development resulted in an integrated 128-element linear imager for the 1- to 5-micrometer

region. An array of 128 indium antimonide photodiodes is coupled to a silicon multiplexer, capitalizing on hybrid fabrication techniques resulting in very low readout noise.

The device shown achieves the inherent, high sensitivity of the diodes in an array format compatible with high-resolution imaging. It operates at temperatures from 55 to 80 kelvins and at readout rates up to one million samples per second. The line array imager has been used in a laboratory demonstration and will be placed in a spectrometer for use at the 200-inch Hale telescope. These tests will confirm its performance capabilities in observing astronomical targets and produce planetary infrared data previously unattainable.

ORIGINAL PAGE IS
OF POOR QUALITY



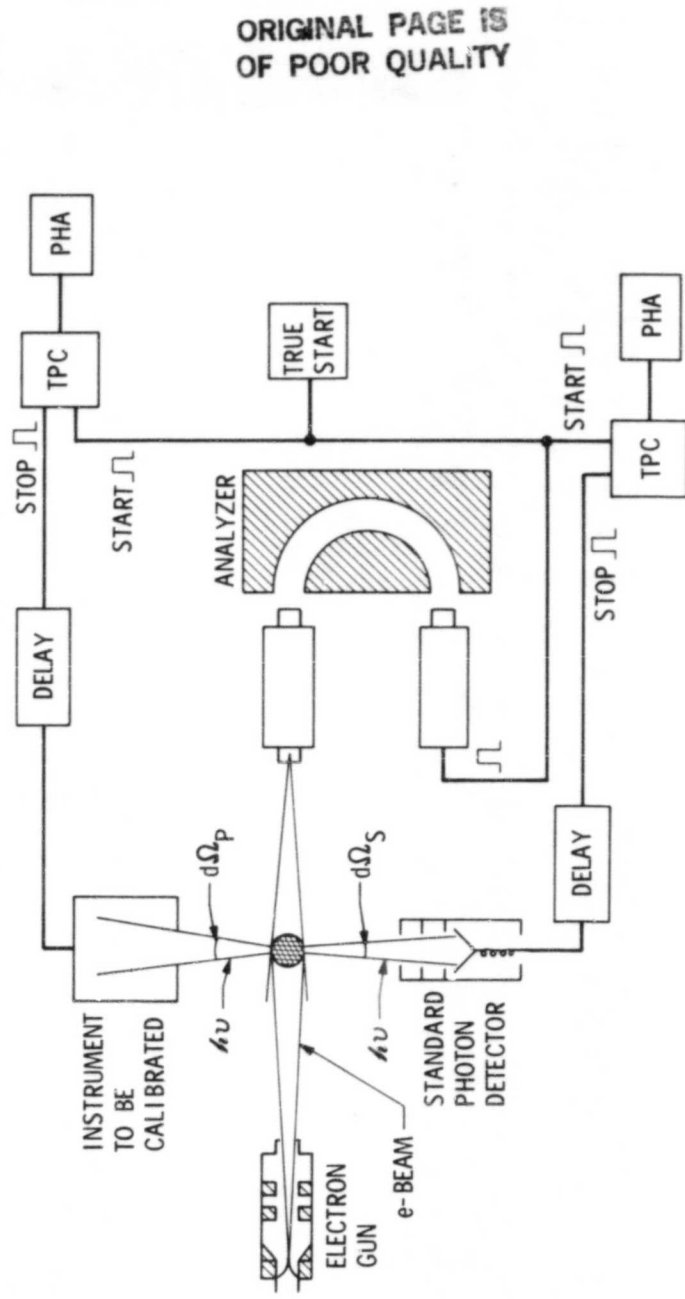
The experimental 128-element infrared linear array of indium antimonide photodiodes shown here uses silicon multiplexer for readout.

AN ELECTRON-PHOTON COINCIDENCE TECHNIQUE AS A RADIOMETRIC CALIBRATION STANDARD IN THE VACUUM ULTRAVIOLET

A new method was developed to calibrate space instruments and detectors which make very low light level measurements in the vacuum ultraviolet region of the spectrum. The experimental technique utilizes a crossed electron beam-atomic beam collision arrangement, where the colliding electron generates a photon emitted by the excited state of the atom. By detecting the emitted photon through the instrument to be calibrated in coincidence with the inelastically scattered electron, one can accurately calculate the absolute number of photons generated by the source for the purpose of calibration. The figure shows the experimental arrangement.

experimental arrangement.

The technique is new and important because the only other standard source commonly used for the calibration in the vacuum UV region, especially below 1000 Å, is a synchrotron. However, at very low light levels, where photon-counting methods are employed, such a high intensity source is not suitable. The proposed technique utilizes the low intensity resonance radiation of the various atoms, such as helium, neon, argon, krypton and xenon, to generate a standard source for calibration.



ORIGINAL PAGE IS
OF POOR QUALITY

A standard source in the vacuum ultraviolet.

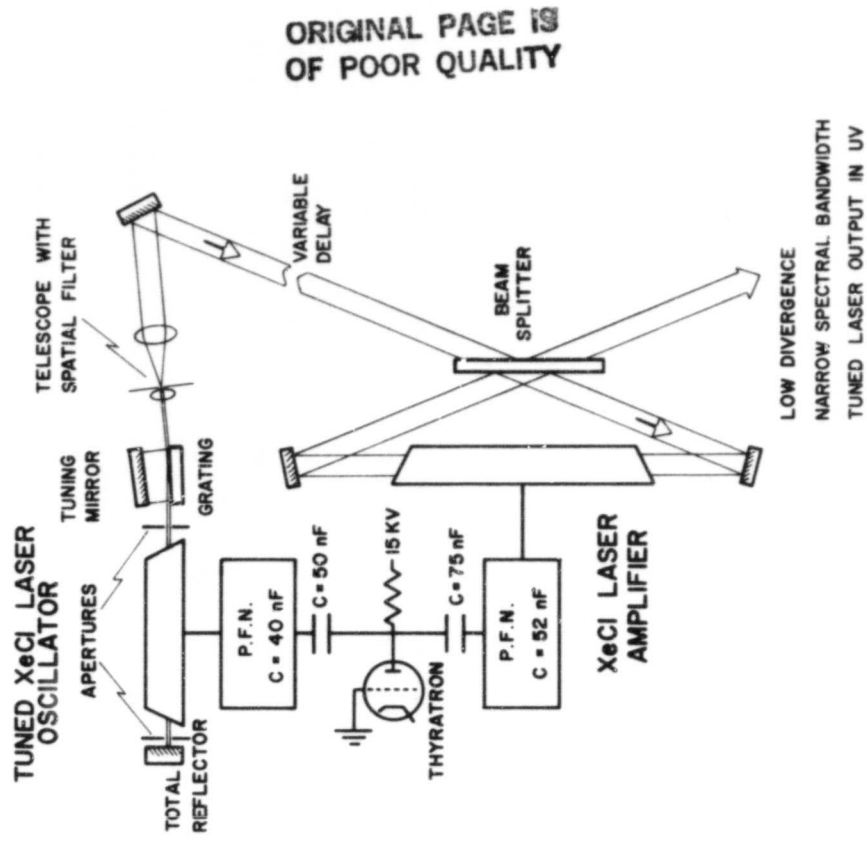
Active laser remote or in situ sensing can complement traditional passive sensing methods and provide local verification for global satellite sensors. Active laser sensing allows high spatial resolution measurements to be made both during the day and night. Ultraviolet lasers are useful for species measurements because they can detect even trace atmospheric constituents by laser-excited fluorescence and in situ resonance ionization spectroscopy.

Laser ability to make measurements of trace atmospheric species until now was limited to the availability of tunable, compact, high-energy ultraviolet laser sources.

Important advances in ultraviolet laser technology have been made at JPL under a NASA-sponsored laser development program for remote sensing. A scanning, narrow-spectral bandwidth, ultraviolet xenon-chloride (XeCl) excimer oscillator-amplifier laser system was produced. This system was used to detect hydroxyl (OH) radicals produced in a combustion source by laser-excited fluorescence. This laser system is one-third the size and much less complex than conventional dye laser sources used by NASA for atmospheric measurements of hydroxyl radicals, ozone, and sulfur dioxide.

The technique is also applicable to other excimer lasers using xenon fluoride, argon fluoride, krypton fluoride, krypton chloride, and xenon bromide. These would provide additional tunable laser sources in spectral regions of the ultraviolet from 193 to 351 nanometers. Additional experiments have also demonstrated the high electrical efficiency, long lifetime for a sealed laser gas filling and scalable laser output energies of over one joule/pulse (33 megawatts) from a XeCl laser.

The XeCl excimer laser is also being proposed for use in oceanographic temperature measurements by Raman scattering of blue-green laser light, and fluorescent measurements of phytoplankton and zooplankton. The XeCl excimer laser can be efficiently shifted to the blue-green region by stimulated resonant Raman shifting in a heated lead (Pb) vapor cell for oceanographic applications.



A scheme by which soil samples from the Martian surface can be returned to Earth in a direct entry/direct return mission envisions the production of the oxidizer between landing on the planet and the least-energy return opportunity. Oxygen can be extracted from the Martian atmosphere, which consists primarily of carbon dioxide containing only small amounts of argon and nitrogen.

The process that employs a solid electrolyte consisting of 8 percent yttria-stabilized zirconia was identified as the most applicable for the in situ propellant production of oxygen.

An electrolytic cell was assembled with a solid electrolyte membrane in the shape of a tube. The inside, as well as the outside, of the tube was covered with porous platinum electrodes which were connected to a DC power source. Surrounding inconel tubing formed the flow passages for the incoming carbon dioxide and the outflowing mixture of carbon dioxide and carbon monoxide.

The cell was installed into a furnace constructed from two clam-shell heaters and insulated for minimal

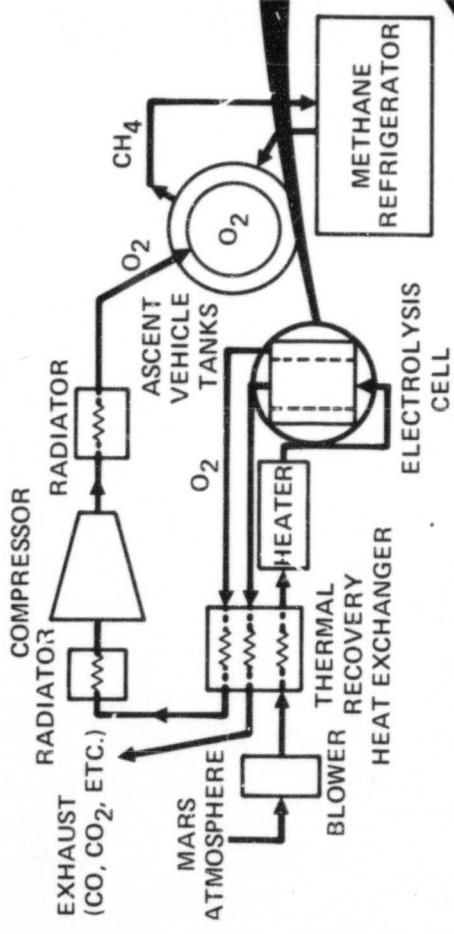
heat losses. A flow panel supplies the cell with pure carbon dioxide or mixtures of gases over a wide range of pressures and flow rates, which are measured or metered by electronic flow controllers and meters. A gas chromatograph confirmed the purity of the produced oxygen.

An upper operating limit with respect to the applied electrical potential was found for the 8 percent yttria-stabilized zirconia, explaining an observed failure mode.

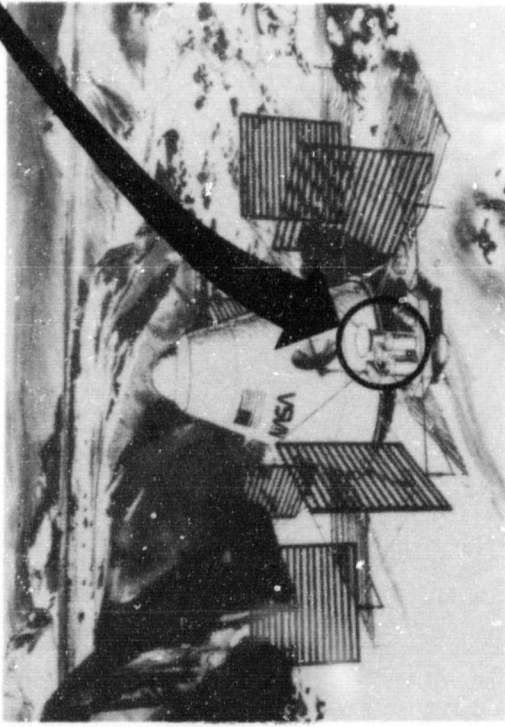
Test data confirmed that the dissociation energy can be supplied entirely thermally and that the electrical potential for extracting oxygen from carbon dioxide is not at all determined by the free energy difference between carbon dioxide and carbon monoxide and oxygen.

The construction of the porous electrodes was identified as a major parameter in the operation of the cell. Integrated solid electrolyte membranes were conceived that promise low resistance to the gas flow while still providing a high electrical conductivity.

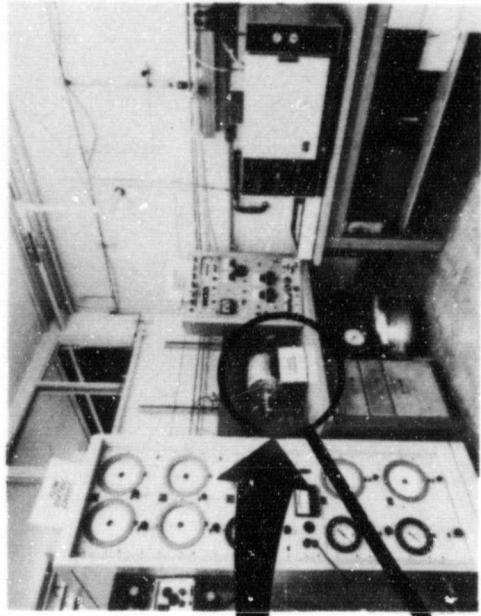
OXYGEN PRODUCTION PROCESS



PROCESSOR AND RETURN VEHICLE ON MARS



EXPERIMENTAL SET-UP AT JPL



ORIGINAL PAGE IS
OF POOR QUALITY

HIGHLIGHTS

- PROPELLANT PRODUCTION FROM INDIGENOUS PLANETARY MATERIALS ENABLES SAMPLE RETURN MISSIONS
- NASA/JPL HAS DEVELOPED A UNIQUE CAPABILITY FOR EXTRACTION OF OXYGEN FROM GASES SUCH AS FOUND IN MARTIAN ATMOSPHERE

In situ propellant processing.

V. Technology Applications

PRECEDING PAGE BLANK NOT FILMED

Through the imaginative mathematical skill of JPL computer animators, millions of television viewers have been brought into the orbit of the United States' space exploration program. The most recent examples of the art were the simulations of the Voyager 2 Saturn encounter on all major U.S. and international TV networks and the animations for the *Cosmos* series on public television.

The Computer Graphics Laboratory began its animated movie production with the Voyager 1 encounter of Jupiter in January 1979. These movies are used for mission design and planning activities and educational services, as well as public information.

The movies are scientifically accurate to the current state of knowledge of each planet or moon being explored. In the case of a first-ever encounter, astronomical photographs and artist renderings are used; but if a previous encounter has returned imagery, these up-to-date results are used. In the forthcoming production of a Galileo movie (on the mid-1980s Jupiter mission), imaging results from both Voyager and Viking missions will be used to make full-color digital maps of Jupiter and its moons.

The location of celestial bodies is precise. Background stars down to the sixth magnitude are taken

from astronomical star maps; the position of each planet is taken from a planetary ephemeris.

The spacecraft itself is depicted from blueprints which are placed on a digitizing tablet and the various spacecraft components reduced to a series of polygons which are stored in digital form in the computer.

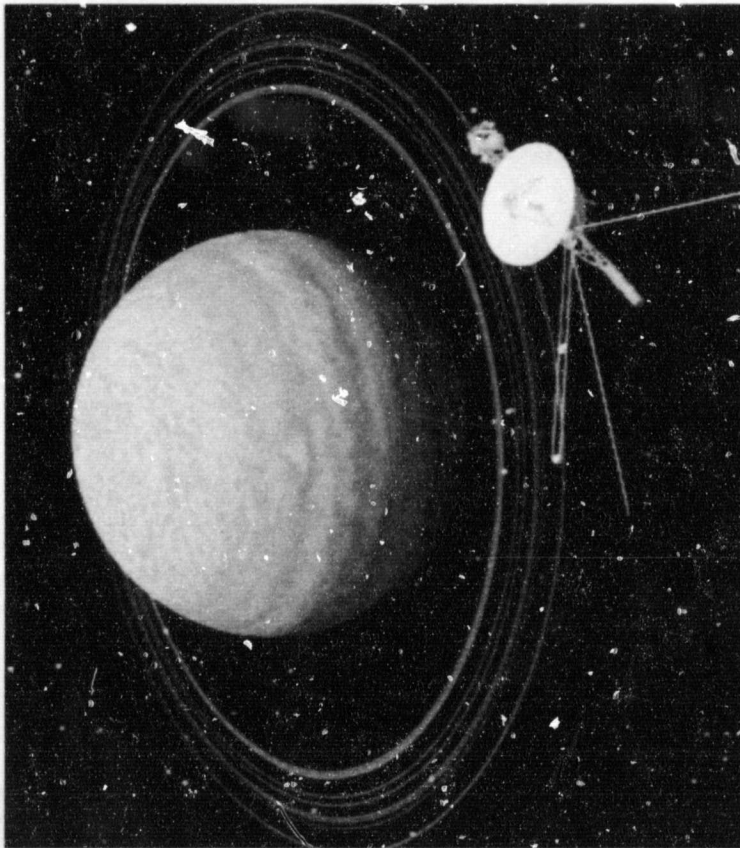
To produce a movie, the mission sequence and trajectory information are used to determine speed, relative approach, and viewing angle for each scene. The scene is then viewed at movie speed in a vector drawing system which produces a line drawing representation of the movie, without color or shading. Once the scene has been edited, the "script" is saved in digital form. The computer then automatically computes each frame in color showing surface features, rings, stars, and spacecraft, all with accurate shading based upon the true position of the sun.

Each frame requires from 30 seconds to ten minutes to compute; a one-minute movie takes one week of 24-hours-per-day computing. The digital data is saved on magnetic tape. Filming is done by reading the tape into a frame buffer to produce a color raster image. By the time composite video and three-color processing is completed, the one-minute movie has taken four more hours to film.

ORIGINAL PAGE IS
OF POOR QUALITY



Saturn as seen from one Dione radius above that moon, 16 hours before Voyager's Saturn encounter. The field of view is 30 deg in this computer animation. The small moon barely visible in the center of the ring plane is Enceladus.



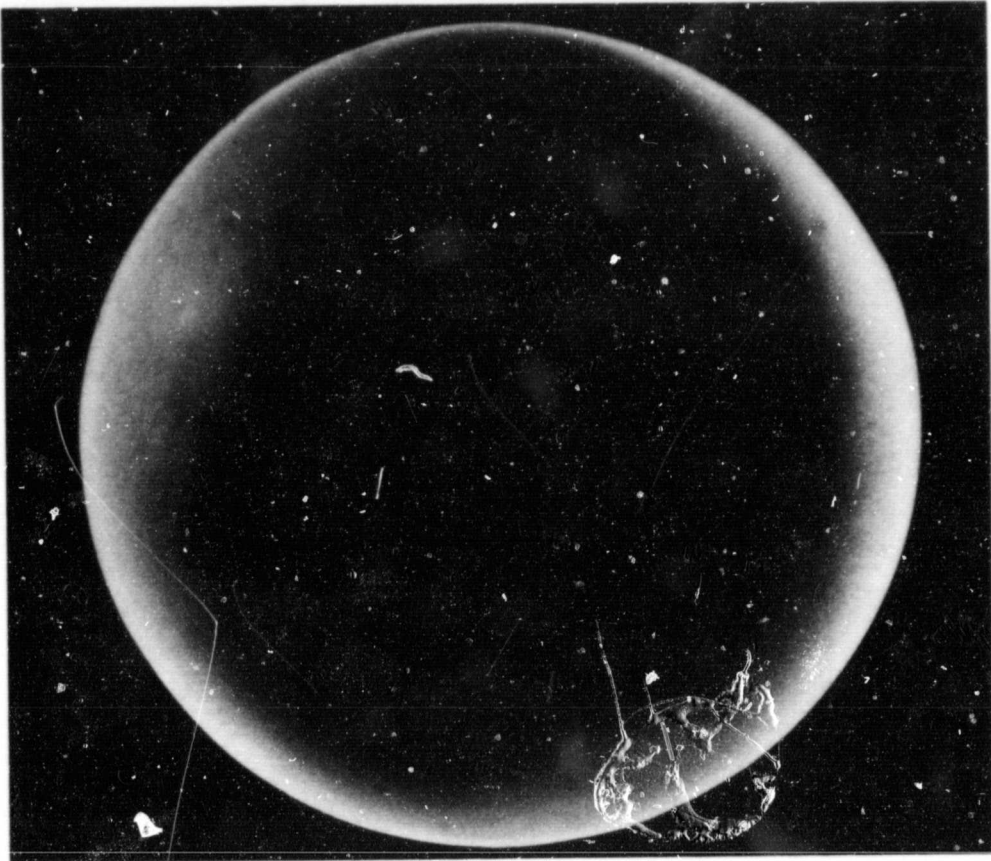
Voyager 2 encounters Uranus in 1986, as depicted by the JPL Computer Graphics animators in their film for the Voyager Project.

Inertial confinement fusion (ICF) is one of the promising techniques for future power generation. In this, a spherical capsule containing thermonuclear fuel is caused to implode by focusing an intense burst of beam energy upon the external surface.

One challenging aspect of this program concerns the development of suitable fuel containers, called fusion targets or pellets. These are hollow spheres comprising concentric layers of various materials. The outer diameter is about 0.25 millimeter in present designs, but may be increased to 5.0 mm in later versions. Pellets must possess high sphericity, concentricity, and smoothness, and be able to contain internal pressures up to 750 atmospheres. Moreover, they must be inexpensive to produce.

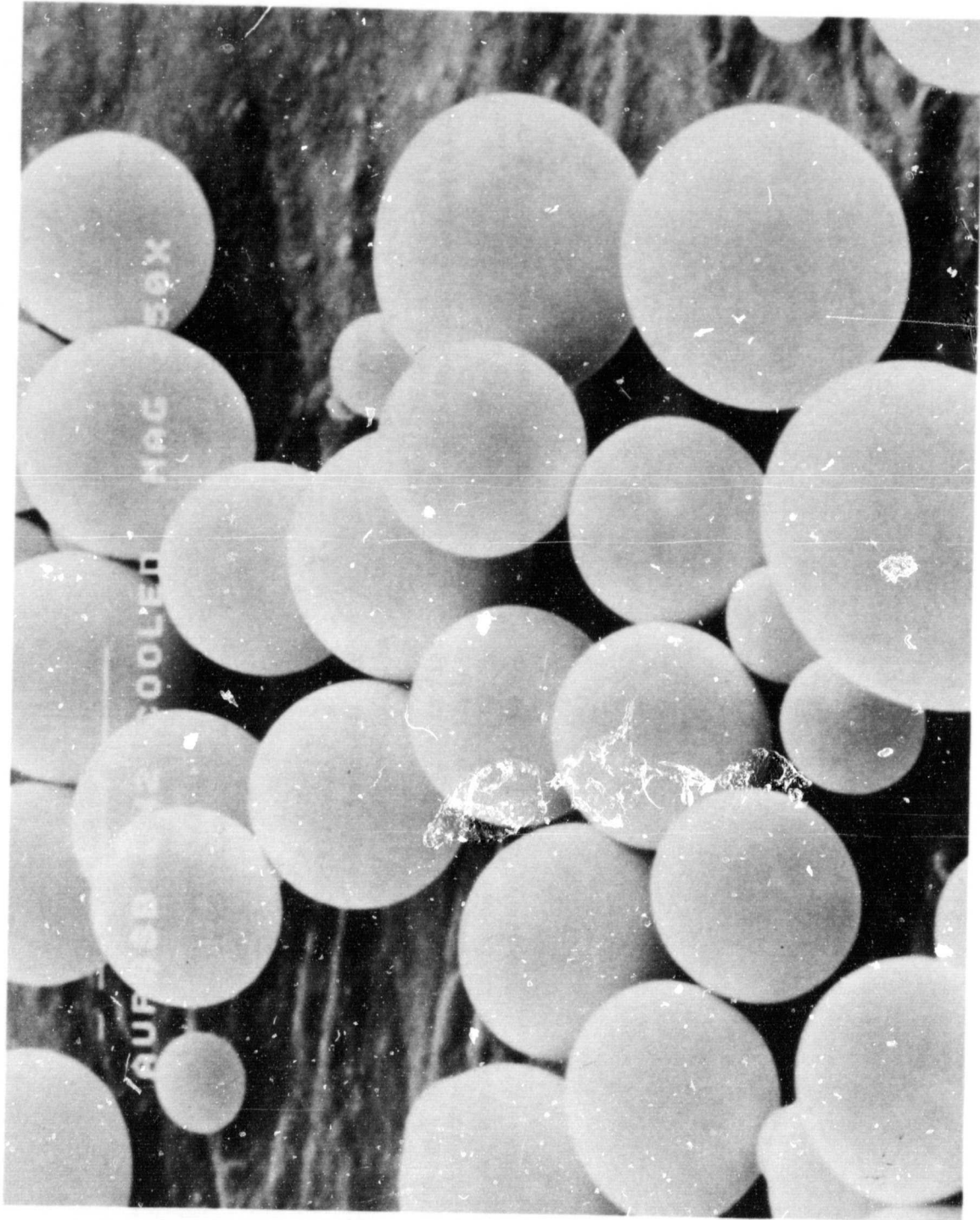
A technique for producing precision metal shells was developed by JPL research engineers. Liquid metal is forced through an axisymmetric nozzle which contains a center tube providing a flow of fill gas. The resultant hollow jet flow of liquid possesses an inherent instability that causes it to pinch-off spontaneously, thereby capturing the fill gas and forming shells. When freezing of the metal is delayed sufficiently, surface tension forces cause the shells to assume a spherical form.

Additionally, a metal which may be particularly well-suited to ICF designs has been employed with some success. An alloy composed of gold, lead, and antimony -- developed at Caltech and studied because it can be frozen in amorphous form -- offers several advantages over other candidate metals. The amorphous form ensures that the surface finish will not be degraded by crystalline structure, and that the material will exhibit excellent strength. The high atomic number of the composition is favored in current target designs.



Radiograph of a shell formed of tin, which serves as a test metal. The sphericity of typical 2.0-mm diameter specimens is excellent, and the surface finish and wall uniformity are good.

ORIGINAL PAGE IS
OF POOR QUALITY



Assemblage of solid spherules of amorphous *allo*- γ with diameters ranging between 40 and 120 μm . Spherules exceeding 1.0 mm in diameter and shown by x-ray analysis to be devoid of crystallization have been produced. This size had previously been unattainable.

AUTOMATED CERVICAL CANCER SCREENING

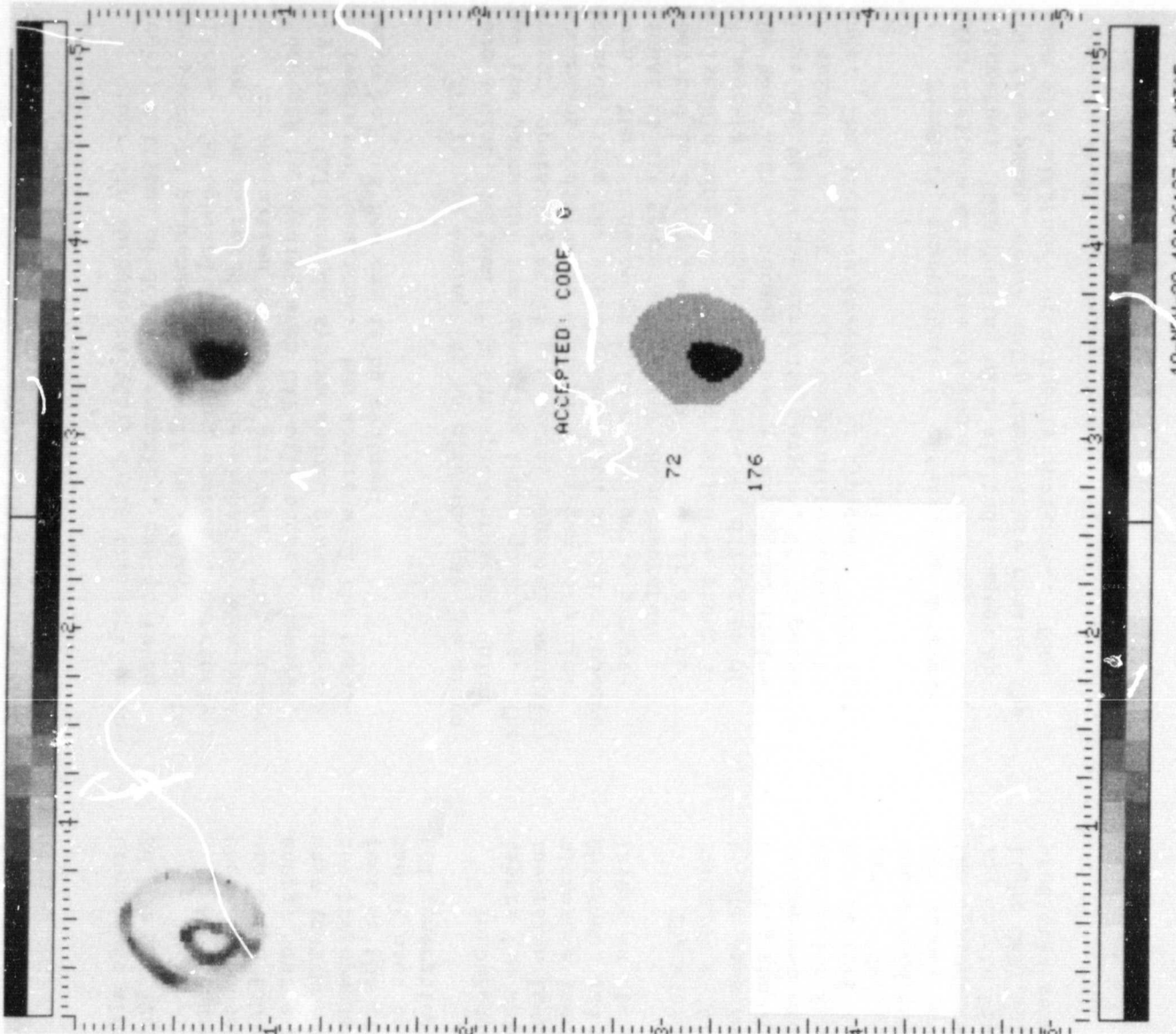
Fifty million women in the United States are at risk for cancer of the uterine cervix, a disease that can be treated successfully if detected in the early stages by the well-known Pap smear. One of the factors that limit the use of the Pap test on a wide scale is the amount of labor required to prepare and analyze the specimen.

Working in collaboration with pathologists at UCLA, JPL completed a four-year study aimed at designing an automated system to prepare the specimen on microscope slides. These slides were searched for abnormal cells, and predictions made as to how well such a system would perform in clinical use.

The study involved the computer analysis of 10,000 cell images. The machine outlined the nucleus

and cytoplasm of each cell and measured the size, shape and texture of each. The cells were classified as normal or abnormal, and this was compared to the true class as determined by a pathologist. A cost-benefit analysis indicated that an automated system could make a significant contribution in the clinical laboratory if the processing can be stepped up 1000 times faster.

A clinical prototype, scheduled to be built this December, will use a special JPL-designed multiple-microprocessor computer to achieve the desired speeds. After one year of testing, the system will be put into use at UCLA for further evaluation. The Pap smear-replacement prototype is believed to be the first developed for clinical use in the United States.



**ORIGINAL PAGE IS
OF POOR QUALITY**

The microscopic image of a cell from the uterine cervix (upper right) is subjected to computer processing for edge enhancement (upper left). The computer then outlines the cell and its nucleus (lower right) and measures the size, shape and texture of each. Based on these measurements, the machine decides if the cell is normal or abnormal. Abnormal cells are called to the attention of the medical technician.

CLEAR AIR TURBULENCE AVOIDANCE USING MICROWAVE RADIOMETRY

Clear Air Turbulence (CAT) costs the airline industry millions of dollars annually, and it is an annoyance to passengers, as well as a distraction to pilots. No onboard CAT warning system is currently in use. An infrared sensor, developed by NOAA/NASA, is under evaluation by United Airlines. This sensor endeavors to predict when CAT will occur. However, any final CAT warning system should provide answers to two other questions: how severe will the turbulence be, and how can it be avoided?

JPL is now evaluating an airborne passive microwave sensor, derived from the space program, which has the potential for answering these questions. The sensor, operating at 56 gigahertz, measures naturally occurring radio waves emitted by oxygen molecules located along the viewing direction of the microwave horn. The intensity of this radiation is proportional to air temperature, and the temperature measured is approximately that of the air at the applicable range of the sensor, which is about 3 kilometers. By scanning the viewing direction of the horn antenna through several elevation angles above and below the aircraft horizon, it is possible to build up a plot of air temperature versus altitude. The altitude coverage is typically 7000 feet.

tropopause altitude generally varies between 30,000 and 50,000 feet.

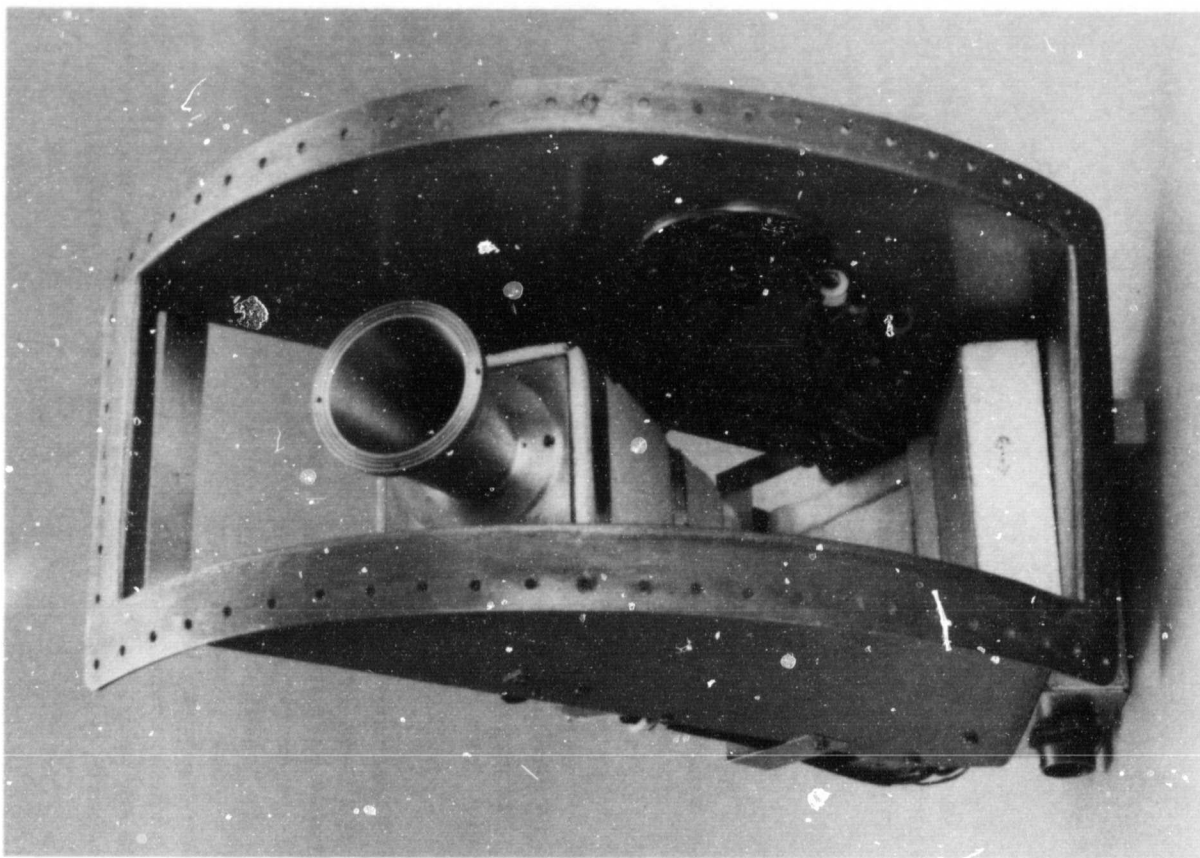
About half of severe CAT encounters occur at the tropopause. The high levels of wind shear that are often found near the tropopause may provide the energy source for turbulence production. The microwave instrument under evaluation is able to locate the tropopause when it is within a few thousand feet of the aircraft flight level. This capability can be used to guide the pilot away from areas where CAT generation is most likely.

Turbulence is also generated within inversion layers (in which temperature increases with altitude). Inversion layers can be found at any altitude. The microwave instrument is also capable of measuring the thickness and temperature contrast across inversion layers in the aircraft's vicinity.

The microwave sensor was installed this year in the NASA C-141 Kuiper Airborne Observatory, operated by the Ames Research Center. Preliminary results confirm the instrument's ability to locate the tropopause and inversion layer features. Encounter statistics support the hypothesis that the more severe turbulence is encountered close to the tropopause. The tests over the western United States could lead to an improved sensor, making it possible for pilots soon to make an appropriate choice between the options of: (1) remaining at altitude, but turning on the "fasten seatbelt" sign (for predicted light CAT), or (2) changing flight level (in case of predicted severe CAT).

Normally, temperature is observed to decrease with altitude at a rate of about 7 kelvins/kilometer. This cooling with altitude ceases at the tropopause, above which temperature remains the same with altitude, or actually increases. The

ORIGINAL PAGE IS
OF POOR QUALITY



This passive microwave radiometer (weight 17 pounds) is installed in the NASA C-141 Kuiper Airborne Observatory aircraft, in the leading edge of a wheel well. The microwave horn, with a 3-inch diameter aperture, is mounted to a box containing the 56-GHz radiometer. A stepper motor and belt-drive system rotate the horn/radiometer assembly through a selection of elevation angles for the necessary temperature measurements.

Air pollution is recognized as a major environmental problem in the United States. Over three decades of legislative control efforts have been unsuccessful in reducing the air pollution in southern California to acceptable levels. The U.S. Environmental Protection Agency has expressed a need for accurate, timely, and easily understandable information about daily levels of air pollution. This information would allow individuals to modify their activities when air pollution levels are high or to take other temporary measures to protect themselves.

The Earth Resources Applications Group used JPL Image Processing Laboratory techniques in conjunction with station-measured air quality data and population statistics to assess population exposure to air pollution. An automated procedure was devised to calculate hourly population exposure to ozone at specific locations in the South Coast Air Basin of southern California. This utilized several techniques to combine and superimpose data of differing types and scales onto a common map base.

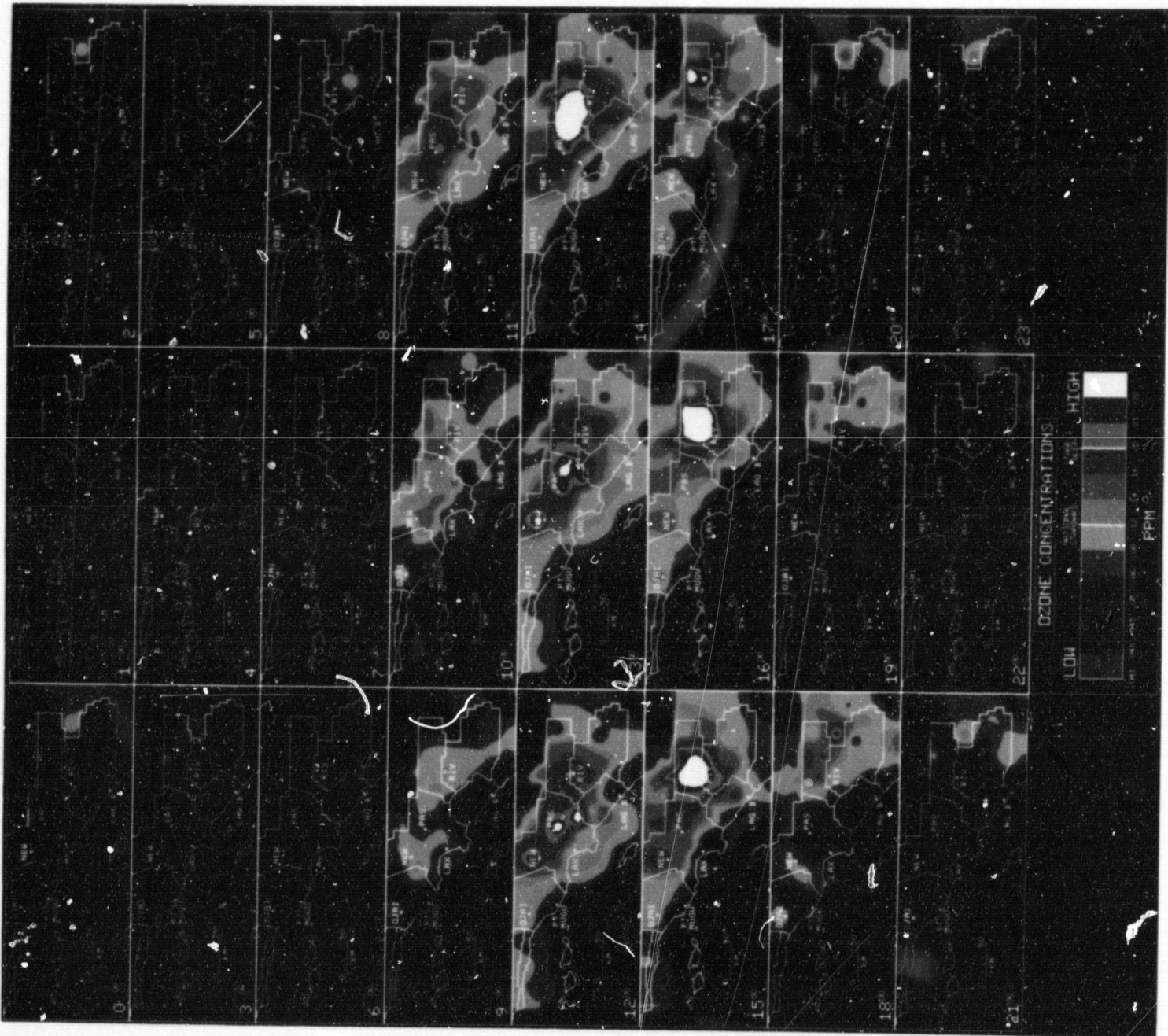
The time-lapse imagery (opposite) shows the diurnal variation of ozone concentrations in the South Coast Air Basin in southern California on June 26, 1974. This imagery demonstrates how large volumes of complex environmental data can be presented in a

format which greatly eases its interpretation. It displays the 24 hourly average ozone concentration data with a key to the colors used. The numeral in the lower left corner of each sub-image indicates the starting hour of the average for that image.

The photochemical nature of ozone production can be witnessed. Note the rapid build up of ozone during daylight hours and its dissipation as the sun sets. The eastward migration and enlargement of the highest ozone concentrations is also shown, illustrating how the predominant westerly wind carries pollutants, originating in Los Angeles, up against the San Gabriel and San Bernardino mountains where they photochemically react to produce smog.

Further application of image processing technology to air quality problem assessment is being pursued by the Earth Resources Applications Group. If data from past years are examined, a historic record of exposure to pollutants may be compiled. Current concentration levels could be measured and added on a daily or hourly basis to identify major problem areas. The output of air quality models, which predict future pollutant concentrations over urban airsheds, could also be incorporated to provide accurate pollution forecast maps for increased public awareness.

~~SECRET~~
ORIGINAL PAGE
COLOR PHOTOGRAPH



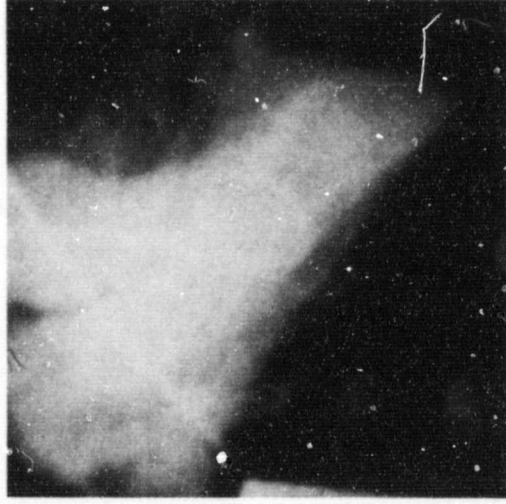
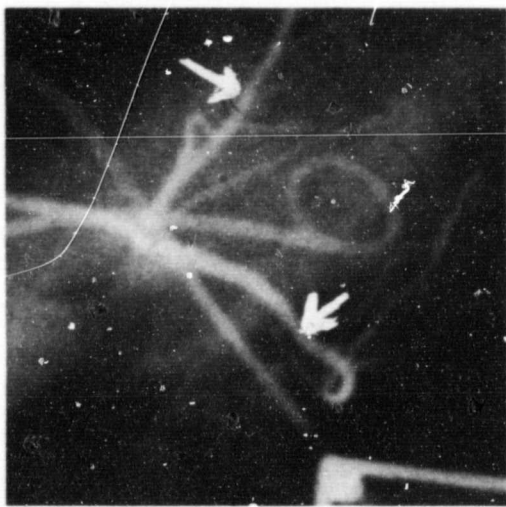
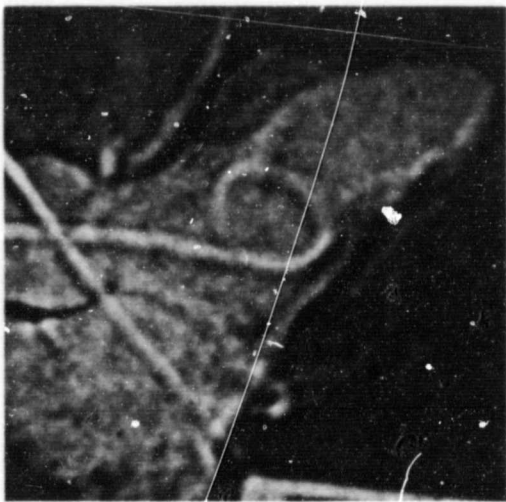
COMPUTER ENHANCEMENT OF CORONARY ARTERIES FROM INTRAVENOUS ANGIOGRAMS

A computer technique for x-ray film enhancement devised at JPL has permitted the clear visualization of the coronary arteries of a dog from an intravenous angiogram. The work, sponsored by the NASA Office of Life Sciences, gives promise of being applicable to intravenous human angiograms.

The result was the first clear picture of coronary arteries from venous dye injection x-ray films yet made, according to the medical researchers. In the usual angiogram employing a radio-opaque dye injection, the dye fills the ventricles of the heart as well as the arteries. This in turn reduces the relative contrast in the film so that the arteries are indistinct, hence the necessity of computer enhancement of the film.

In collaboration with University of Southern California medical researchers, the JPL imaging team applied a computerized three-dimensional filtering to 36 frames of film recorded at 1/60-second intervals. Filtering was used in both the spatial and time domain and a sequence of 30 enhanced images was re-recorded on film for viewing in motion.

Efforts are continuing to develop improved filtering techniques that will decrease the computer noise levels in the enhanced images. After the enhancement methods are developed, the technique will be further tested in animal models and eventually applied to human angiograms.



Example of intravenous angiogram of dog's heart.

Location of arteries from conventional arterial-injection angiogram.

Enhanced intravenous angiogram.

ANTICANCER DRUG MICROSPHERES FOR LEUKEMIA TREATMENT

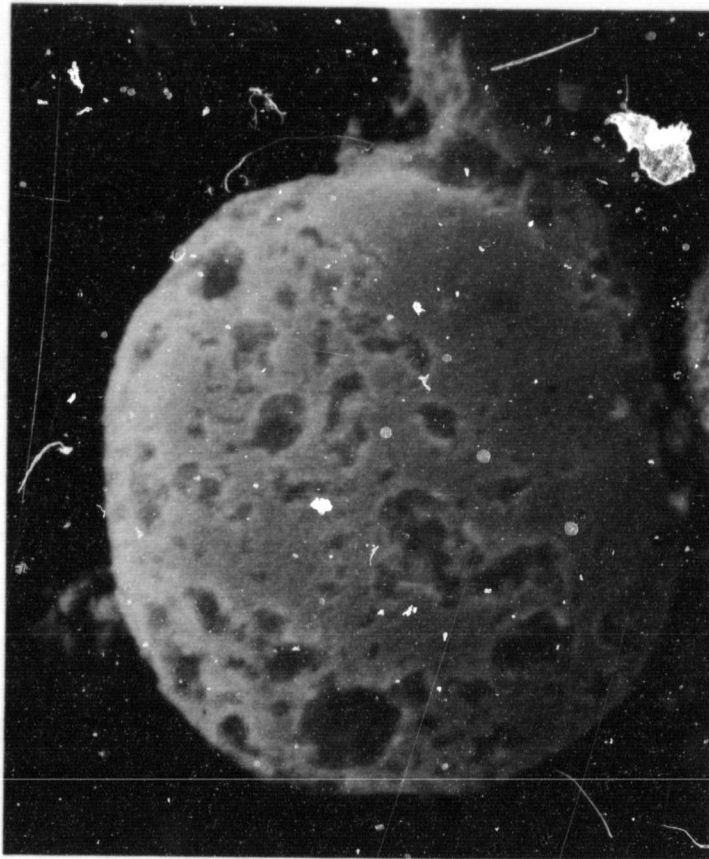
Polymeric microspheres developed by JPL chemists have proven in tests this year to be a helpful agent to the drug adriamycin in curbing the growth of leukemia cancer cells.

Adriamycin is a universally used anticancer drug, yet its mechanism of action is at present not well understood. It is not known whether the drug needs to diffuse into the nucleus of the cell and interact with DNA in order to exercise its toxic action or whether its action is due to the perturbation of cell surface membranes. Investigations conducted in collaboration with the University of Southern California Comprehensive Cancer Center revealed that adriamycin covalently bound to polyglutaraldehyde microspheres sufficiently perturbs the plasma membrane of malignant cell lines to lead to

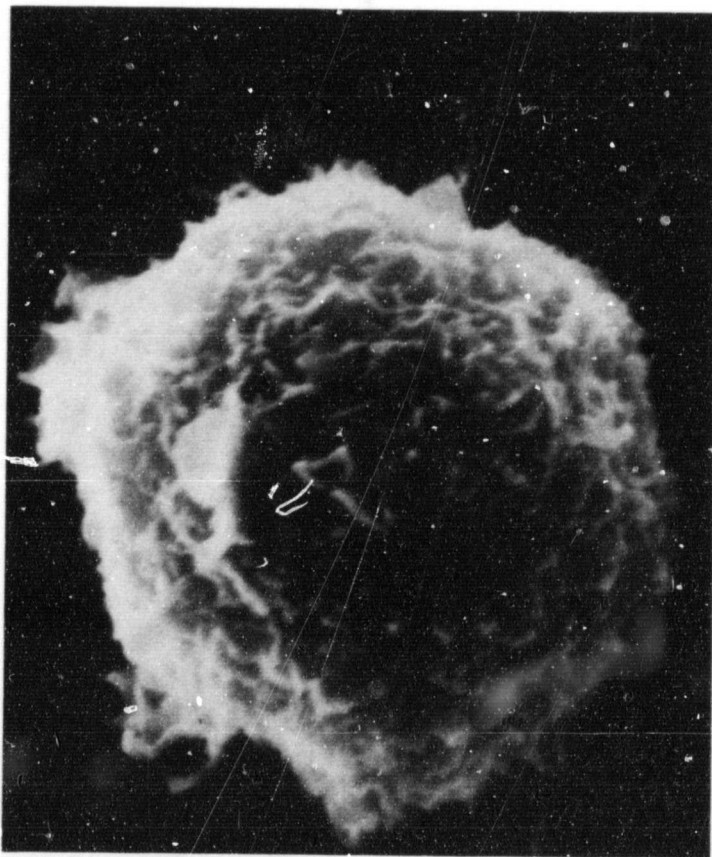
cytostatic activity -- the slowing down of cancer cell growth. The obtained evidence is based on the study of cytostatic activity of a number of malignant cell lines (including human lymphocytic leukemia cells) interacting with polyglutaraldehyde-adriamycin conjugates and is supported by the altered cell surface topography.

In addition to the results obtained on adriamycin action, further investigation at JPL of antibody bodies bound to microspheres led to new clinical assays of antigens present in blood and urine based on light-scattering techniques. These new nephelometric assays are likely to replace the now widely used radioimmuno assays which present a problem of radioactive waste disposal.

ORIGINAL PAGE IS
OF POOR QUALITY



Scanning electron photomicrograph of a leukemic cell treated with polymeric microspheres adriamycin conjugates for 24 hours. The extensive damage to the cell membrane causes growth inhibition.



Scanning electron photomicrograph of a leukemic cell treated with polymeric microspheres for 24 hours (control). The appearance of the cell is identical to that of an untreated cell.



ORIGINAL PAGE IS
OF POOR QUALITY

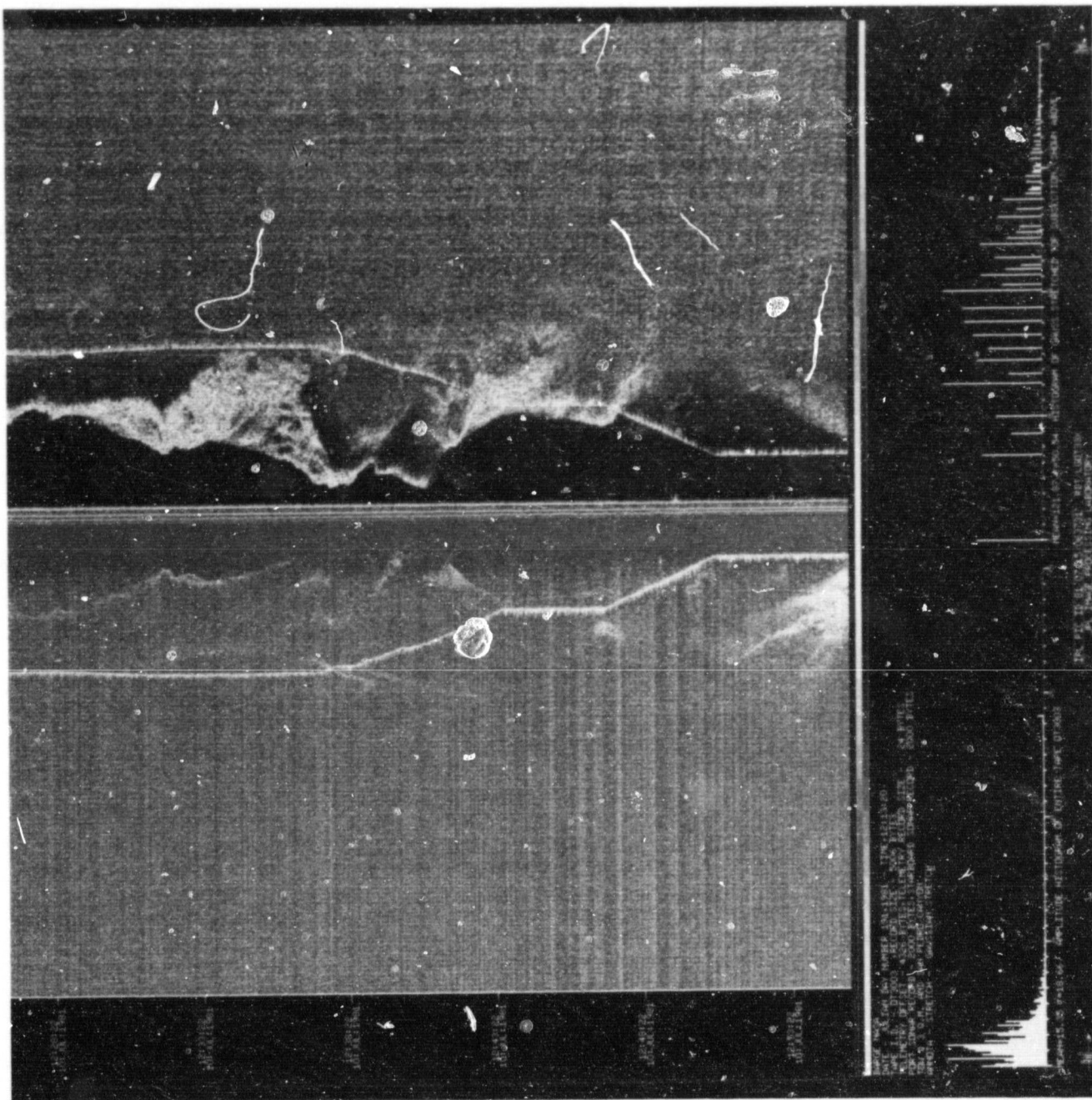
An unmanned underwater vehicle for deploying and testing oceanographic instruments and sonars has been built and successfully demonstrated by JPL engineers in the Advanced Ocean Technology Development Platform (AOTDP) project.

The AOTDP system consists of three elements: the fully instrumented submersible housing (FISH), which serves as a platform for data collection electronics and instruments; the shipboard control, data processing and display equipment housed in a seagoing van; and an armored coaxial tow and communications power (60 hertz) cable linking the FISH and control center.

The computer systems, unique in the oceanographic field, have been adapted from space technology. They enable scientific and operational data to be processed in real time or to be stored on magnetic tape for later investigation. The tape format is compatible with the JPL Image Processing Laboratory (IPL) format. Several AOTDP ocean test tapes have been processed by the IPL, whose special techniques were used to improve sonar images.

The National Oceanic and Atmospheric Administration (NOAA) supplied partial funds for the sonar development. From the FISH, the side-looking sonars have imaged underwater objects 450 meters away at depths up to 260 m. The FISH can work down to 6000 m with a tow cable about 10,000 m long.

The AOTDP Project's FISH is shown being readied for deployment into the water at dockside prior to checkout of the system. The port side-looking sonar transducer is visible on the centerline of the cylindrical pressure hull.



Side-looking sonar image of the steep wall of the undersea San Pedro Valley, south of Palos Verdes Peninsula. Side-looking sonar portrays the seafloor in a plan-view much like an aerial photograph. However, the side-looking process also includes a vertical profile of the bottom causing a slight distortion removable by IPL processing.

VI. Basic Research

PRECEDING PAGE BLANK NOT FILMED

CLOSED ECOSYSTEMS RESEARCH

A JPL scientist has established the first totally self-sufficient communities of shrimp, algae, and microorganisms capable of generating their own food, oxygen, and water within the confines of a sealed glass flask in a laboratory.

These closed aquatic communities, called materially closed ecosystems, were one year old last June. Such a long-lived microecosystem is of major significance to the science of ecology.

The animals and plant life in these ecosystems are believed to be the largest to have lived for a year in a closed environment. The development of techniques to measure the chemical and biological recycling processes that allow these closed microecosystems to survive could lead to the first chance for ecologists to perform rigorously controlled repeatable experiments on whole ecosystems.

might be applied to developing larger, more complex ecosystems to support human colonies in space.

The materially closed ecosystems live in one-liter glass flasks, hermetically sealed by melting the necks of the flasks closed. Only radiant energy and heat may enter or leave through the glass walls.

Living in synthetic sea water inside each flask are up to 16 small red tropical shrimp less than an inch long, assorted algae and many varieties of bacteria, viruses and microscopic animals. Inside the flasks, plants (algae) produce the oxygen and foods that feed the shrimp and other animal life, and the animals' wastes provide carbon dioxide and fertilizer consumed by the algae. This cycle is driven by artificial sunlight provided 12 hours a day by fluorescent lamps.

NASA has become interested in this work to the extent of sponsoring a workshop next year specifically concerned with materially closed ecosystem research and its potential for contributing to NASA's Controlled Ecology Life Support System (CELSS) Program. JPL will organize and chair the workshop.

In addition, the closed ecosystems experiment may help scientists in understanding what is needed to produce regenerative life support systems for humans. Information on how the materially closed ecosystems work

ORIGINAL PAGE IS
OF POOR QUALITY



ON BOOK SHELF
DUSTY AND DIRT

The JPL closed ecosystem colonies of shrimp, algae, and marine microorganisms are shown thriving in synthetic sea water after one year in hermetically sealed laboratory flasks.

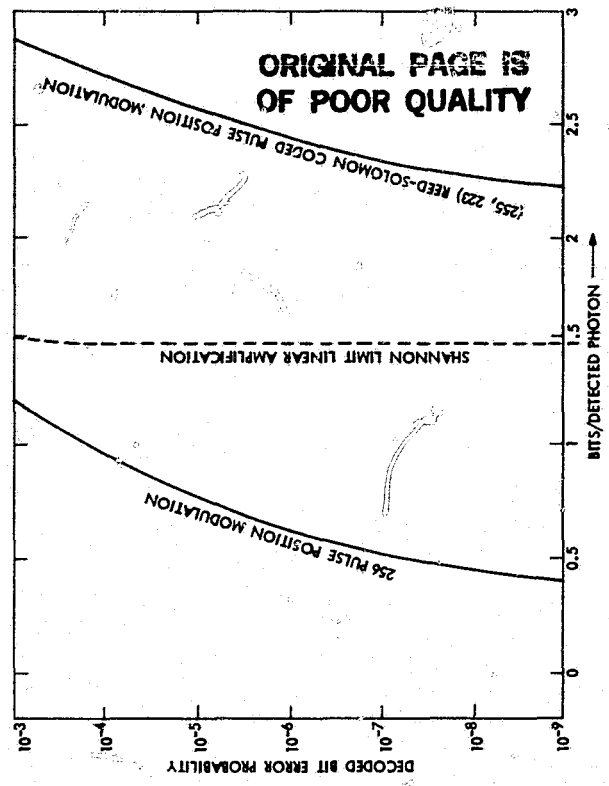
Compared to conventional microwave links, optical channels offer advantages due to much shorter wavelengths and the resulting higher antenna gains and components of smaller size and weight, and also in some applications due to extremely large information bandwidths. Joint JPL and Caltech research has shown that the direct detection of photons at optical frequencies offers a considerable information-theoretic advantage over the conventional methods of linear signal amplification.

The information-theoretic advantage results because the capacity of the optical channel using photon-counting techniques is not limited by the quantum ($h\nu$) noise of linear amplification, but only by thermal noise, with the same capacity formula holding at optical frequencies and microwave frequencies. The previous limit was $1.44 (\ln 2)$ bits per detected photon. With the new capacity formula, an optical system operating in the blue-green region can conceptually achieve a capacity of about 100 bits per detected photon with expected noise temperatures.

A key ingredient for deep space optical communication systems using the new coding schemes is a high-brightness single spatial mode pulsed laser emitter. Gallium arsenide semiconductor injection lasers were selected for this application because of their high reliability and efficiency. Their major disadvantage is a low level of emitted power. Work done in collaboration with Caltech demonstrated the feasibility of a method for achieving higher power levels by coherently combining a monolithic stack of four lasers in a phased array. The peak powers of about 1/4 watt produce a single 1-watt pulse. As a result of the 1980 work, optical communication looks ever more attractive for deep space communication and for intersatellite relay for near-Earth communication.

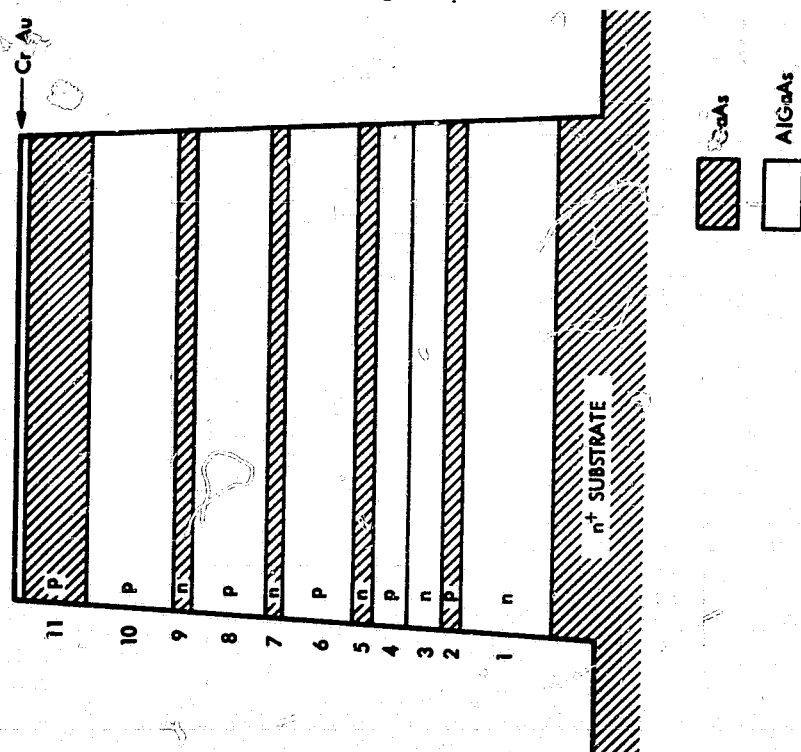
However, studies indicated that, due to complexity and bandwidth constraints, an information efficiency of about 10 bits per detected photon represents an upper limit on the performance of any practical system. (The 1.44 bits/photon for linear amplification is a theoretical, not practical, limit.)

The ability to achieve the goal of 2.5 bits or higher per detected photon depends on the validity of the mathematical models used in the performance analysis. For this reason, the verification of the channel noise models is a crucial first step. These models were checked experimentally in the deep space optical communication laboratory, and the results show excellent agreement between theory and experiments.

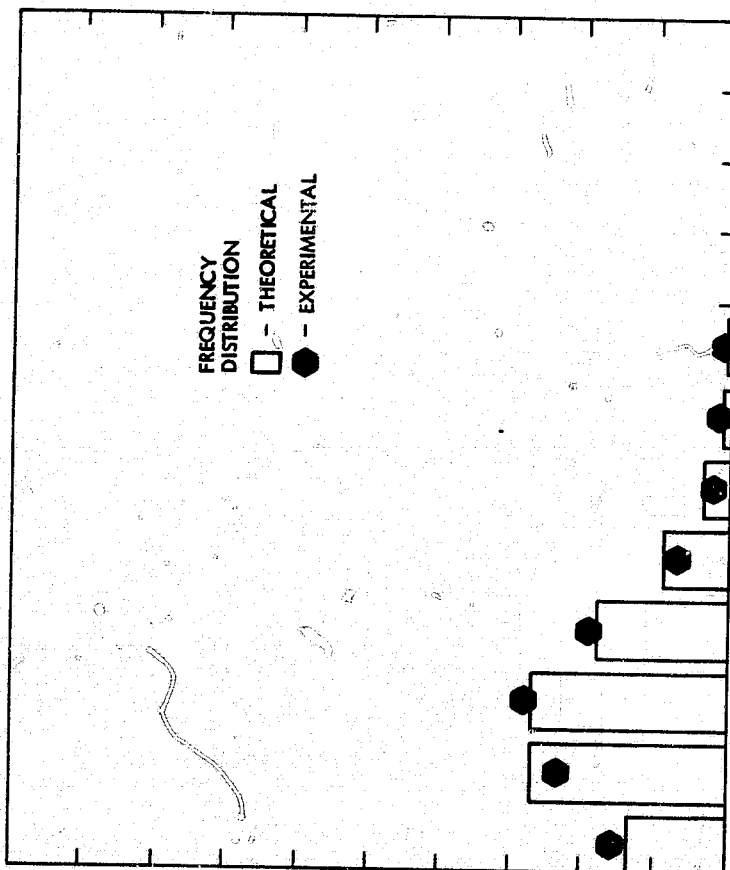


Performance curve of optical link.

ORIGINAL PAGE IS
OF POOR QUALITY



Cross-section of the combined device.



Experimental results on the intrinsic noise characteristics of the free-space optical channel.

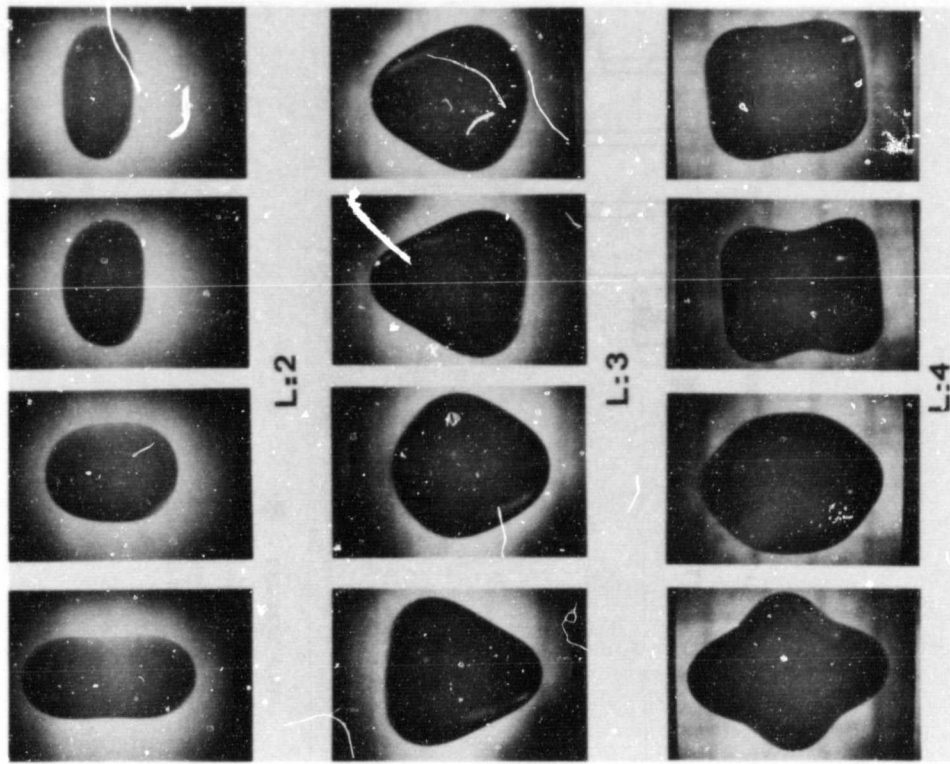
Basic research is just one of the motivating forces behind the JPL study of the phenomena related to the dynamic behavior of free liquid drops. The prospects of space materials processing and terrestrial applications in the fields of chemical engineering, energy production, and meteorology are affected by the acquisition of new information concerning the vibrational, rotational, and internal flow motions of such unconfined drops. Experiments have been carried out using immiscible liquids and 1 g acoustic levitation systems. The dynamics of free drop shape oscillations were investigated through a non-invasive technique (i.e., without physical contact).

For small amplitude oscillations, a drop suspended in a host liquid behaves in a way similar to the usual damped harmonic linear oscillator. The response to a sinusoidal excitation is almost purely sinusoidal; the frequency of maximum response is characterized by an approximately 90-degree phase shift between the drive and the response; the decay rate is roughly linear with the drop viscosity; and the resonance curve for the displacement has the familiar shape.

However, when the amplitude of the oscillation can no longer be considered small, characteristic nonlinear effects were discovered. For example, the qualitative study of the internal flow field of steady-state oscillating drops revealed fields which are more complicated than suggested by the simple linear theory. Circulation was found to be present even for relative oscillation amplitude as low as 8 percent, and appears to originate first at the drop boundary and to spread subsequently toward the drop interior.

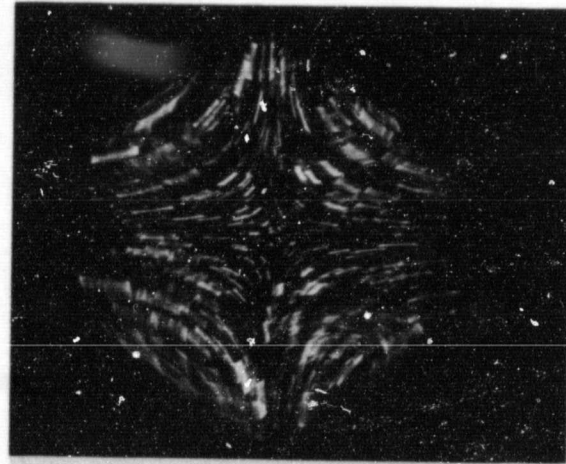
Immediate applications of the techniques developed here can be found in terms of chemical reaction monitoring involving liquids and gases, of

light scattering measurements used in the remote sensing of aerosols, and of the thermodynamic and nucleating properties of liquids deep in the metastable ranges.

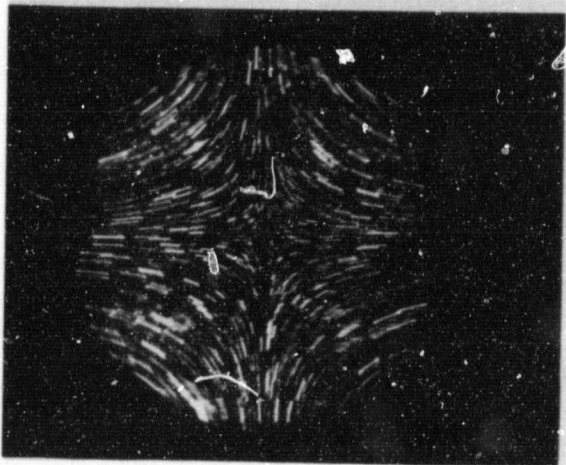


Silicon oil drops oscillating in a succession of axisymmetric modes. L=2, L=3, L=4 are measurements of increasing vibrational frequency intensity.

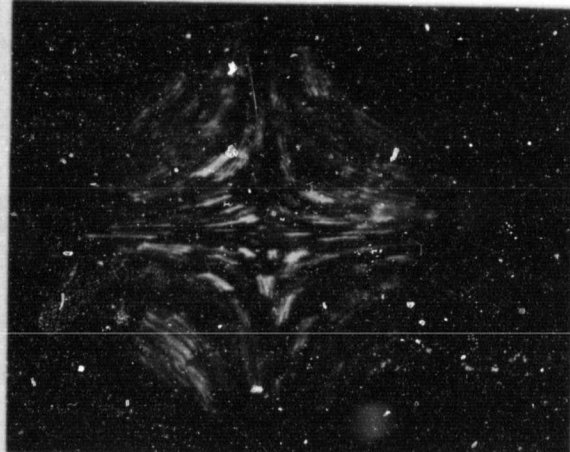
ORIGINAL PAGE IS
OF POOR QUALITY



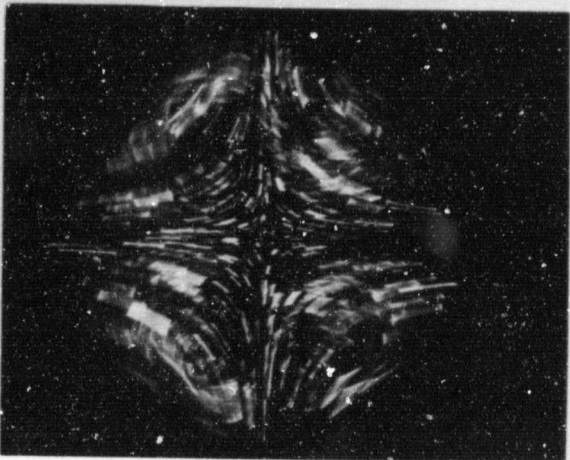
B



A



C



D

Internal flow patterns of a free-floating silicon oil drop oscillating in the $L=2$ mode. The streak patterns are formed by suspended dye particles in the drop.

Free volume in a glassy plastic material was measured for the first time using Electron Spin Resonance (ESR) techniques with spin probes. It is a major step forward in developing experimental techniques to verify liquid state theories.

Comparison of Calculated and ESR Measured Free Volume Fraction in PMMA at 296 K

Aging Time (days)	ESR Measured* Free Volume Fraction	Calculated** Free Volume Fraction	
		Calculated** Free Volume Fraction	ESR Measured* Free Volume Fraction
0.014 (20 min)	0.089	0.07151	
0.03		0.085	
0.063 (90 min)		0.069	
0.875 (21.5 h)		0.06986	
1.00			0.06931
1.792 (43 h)	0.064		0.0468
3.00			0.0436
∞			

The spin-trapping technique, a modified spin-label method, utilizes diamagnetic molecules, such as nitrones and nitroso compounds, as spin traps to react with short-lived free radicals (and/or unstable ionic species) to form stable free radicals (spin adducts) for characterization. The technique has recently been applied to the studies of molecular motions and mechanical relaxation mechanism in polymethyl methacrylate (PMMA), and the curing kinetic mechanism of composite materials. This technique can also be used to study rate of diffusion in polymers.

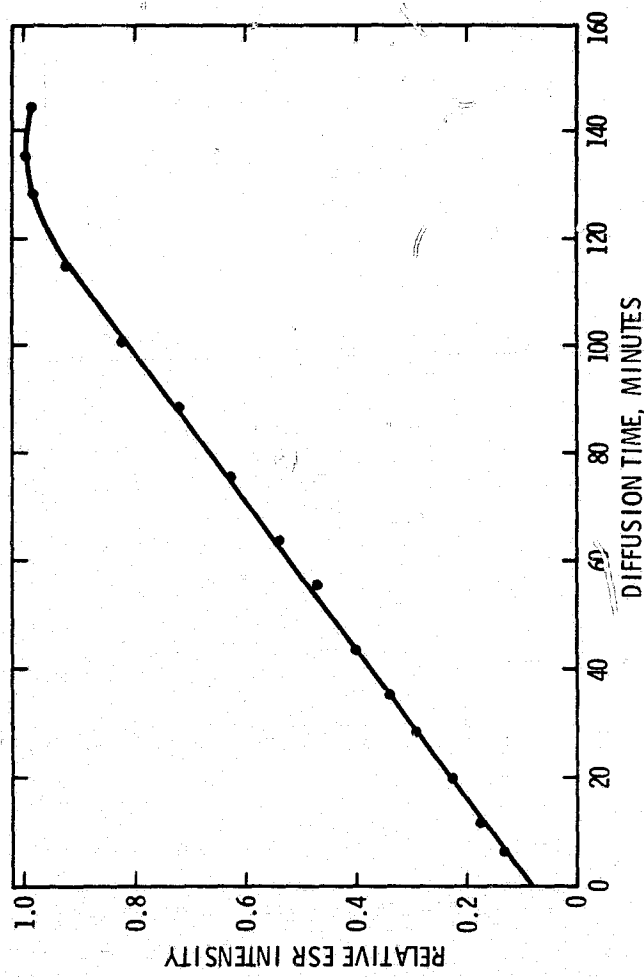
The ESR technique also enables the development of a predictive model describing long-term mechanical property changes affected by physical aging. It provides a potential solution to a long-standing engineering design concern of the long-term aging effects on materials.

*From
$$\left(\frac{\text{Narrow Components}}{\text{Narrow and Broad Components}} \right)$$
 Intensity Ratio

**By Curro, LaGasse and Simha

ORIGINAL PAGE IS
OF POOR QUALITY

ORIGINAL PAGE IS
OF POOR QUALITY



Diffusion of benzene vapor in PMMA containing spin probe.

AUTHORS, ADDRESSES, PHONE NUMBERS

Authors may be contacted by mail at JPL, 4800 Oak Grove Drive, Pasadena, California 91109, or by calling them at the following phone numbers (area code 213). FTS prefix for Lab phones is 792-.

I. DEEP SPACE EXPLORATION

<u>Author(s)</u>	<u>Phone Number</u>
Voyager Saturn Encounter and Uranus Mission	
Saturn After Voyager 2	
The Rings of Saturn	
Titan	
Other Saturnian Satellites	
Magnetospheres of Jupiter and Saturn	
Temperature and Cloud Structure of Venus' North Pole	
Io Heat Flow	
Studies in High-Energy Astrophysics via HEAO-3	
Shuttle Infrared Telescope Facility Fine Guidance Sensor	
Radio Interferometer Observations of Astronomical Object SS433	
JPL Radar Astronomy: Asteroid Apollo and Saturn	
Voyager-Saturn Data Rate Enhancement	
II. ENERGY AND ENERGY CONVERSION TECHNOLOGY	
Large Area Silicon Development	
High-Performance Thermal Storage Materials Testing	
Sunfuels: Integrated Fuels Production and Use	

R. Trieser
354-4729
E. Miner
354-4450

D. Diner
354-4235
D. Matson
354-2984

R. Riegler
354-6259
P. Salomon
354-6214

A. Niell
354-4633
R. Goldstein
354-6999

J. Hall
354-6016

K. Koliwad
354-5197
W. Phillips
354-4051
K. Ekman
577-9020

<u>Author(s)</u>	<u>Phone Number</u>
Acoustic Diagnostics of Turbulent Combustion	P. Seshan 354-7215
Quasi-Bipolar Lead-Acid Battery	W. Rippel 577-9121
Automotive Diesel Engine Particulates Destruction by Electrical Discharge	W. Dovier 354-3169
III. EARTH ORBITAL APPLICATIONS	
Global Maps of Water Vapor, Wind Speed and Wave Height	D. Chelton 354-7151
Advances in Digital SAR Processing Techniques	D. Held 354-7763
Tectonic Studies in the Caribbean With Seasat Radar Imagery	T. Dixon 354-4977
Seasat Altimeter Studies in the Gulf of Mexico	G. Born 354-4644
Seasat Scatterrometer Detection of a Tropical Depression in the Gulf of Mexico	P. Woiceshyn 354-5416
Joint JPL/Caltech/People's Republic of China Earthquake Fault Study	A. Gillespie 354-6927
Portable Radio Geodesy for Geodynamics Measurement	P. MacDoran 354-7118
Balloon-Borne Microwave Limb Sounder	J. Waters 354-3025
Maritime Remote Sensing (MAREN) Experiment in the North Sea	O. Shemdin 354-2447
Regular Solar Irradiance Variations Related to Solar Active Regions	R. Willson 354-3529
Zero Gravity Fluid Dynamics	T. Wang, D. Elleman 354-5182
IV. INFORMATION SYSTEMS AND SPACE TECHNOLOGY DEVELOPMENT	
Image Processing Using Very Large Scale Integrated Systems	R. Nathan 354-2073

<u>Author(s)</u>	<u>Phone Number</u>
Automated Spacecraft Power Systems Management	A. Bridgeforth 354-5626
Remote Manipulator System	R. Dotson 354-7267
Target Body Tracker	R. Armstrong 354-2681
Model Insensitive Control for Elastic Spacecraft Study and Experiment	E. Marsh 354-3599
Optical Fibers for Frequency Distribution	G. Lutes 354-6210
Radio Frequency Interference Surveillance	H. Wilck 354-4298
Delta Differenced One-Way Range for Navigation	T. Yunck 354-3369
An Efficient Atom Source for Hydrogen Maser Frequency Standard	R. Sydnor 354-2763
Spacecraft Contamination Flight Data (NOAA-7)	C. Maag 354-6453
Rocket Propellant High-Pressure Combustion Study	L. Strand 354-3108
Heat Sterilizable Solid Rocket Motor	F. Anderson 354-3167
Electrostatic Levitator for Containerless Science in Space	W. Rhim, D. Elleman 354-5182
Detector Arrays for Infrared Imaging	J. Wellman 354-6638
An Electron-Photon Coincidence Technique as a Radiometric Calibration Standard in the Vacuum Ultraviolet	S. Srivastava 354-3246
Tunable Lasers for Remote Sensing Applications	J. Laudenslager 354-2259
Extraction of Oxygen From Carbon Dioxide	R. Richter 354-3253

V. TECHNOLOGY APPLICATIONS

<u>Author(s)</u>	<u>Phone Number</u>
Computer Animation of Space Mission Planetary Encounters	R. Holzman 354-2544
A Technology for the Production of Fusion Targets	J. Kendall, M. Lee 354-4795
Automated Cervical Cancer Screening	K. Castleman 354-5660
Clear-Air Turbulence Avoidance Using Microwave Radiometry	B. Gary 354-3198
Population Exposure to Air Pollution Study	K. Hussey 354-4016
Computer Enhancement of Coronary Arteries From Intravenous Angiograms	R. Selzer 354-5754
Anticancer Drug Microspheres for Leukemia Treatment	A. Rembaum 354-3189
Advanced Ocean Technology Development Platform System	R. Gulizia 577-9049
<hr/>	
VI. BASIC RESEARCH	
Closed Ecosystems Research	J. Hanson 577-9282
Deep Space Optical Communication	E. Posner 354-6224
The Dynamics of Free Liquid Drops	T. Wang 354-6331
Electron Spin Resonance	A. Gupta 354-5783